ELECTRONIC PROPERTIES OF THE LINEAR CHAIN MERCURY COMPOUNDS

By

© ERWIN BATALLA, M.Sc.

A Thesis

Submitted to the Faculty of Graduate Studies

in Partial Fulfilment of the Requirements

for the Degree

Doctor of Philosophy

McMaster University

March 1981

DOCTOR OF PHILOSOPHY (1981) (PHYSICS)

McMASTER UNIVERSITY Hamilton, Ontario

TITLE: Electronic properties of the linear chain mercury compounds

AUTHOR: Erwin Batalla, B.Sc. (Université de Montréal), M.Sc. (McMaster University)

SUPERVISOR: Professor W. R. Datars

NUMBER OF PAGES: xvi, 123

ABSTRACT

The Fermi surface, resistivity and superconducting properties of the mercury linear chain compounds were studied.

A detailed model of the Fermi surface of the mercury linear chain compounds has been constructed. Measurements of the dHvA frequencies in $Hg_{3-\delta}SbF_6$ are presented and show that the Fermi surface of this compound consists of cylinders. The cross-sectional areas of these cylinders are accounted for by the Fermi surface model. Measurements of the dHvA frequencies in $Hg_{3-\delta}AsF_6$ under pressures between 0 and 4 kbar are also presented. The changes in frequencies with pressure imply that the anions' lattice contracts while the mercury-mercury distance remains unchanged when the pressure is applied.

A model of the lattice resistivity in these compounds is introduced and compared to our measurements of the resistivity between 4.2 and 90 K, and to measurements of the resistivity anisotropy between 4.2 and 250 K. A sudden resistance increase at 217 K, when the samples are cooled, is reported and is associated with mercury extrusion at the same temperature.

Measurements of the ac susceptibility in $Hg_{3-\delta}AsF_6$ for fields between 0 and 400 Gauss at temperatures of 4.2 to 1.2 K are reported. Transitions associated with elemental mercury and with the linear chain mercury compound are observed. The

presence of elemental mercury with the compound is discussed. Measured values for the critical field, the critical temperature and the zero-field susceptibility of the mercury compound are presented and two explanations for these and previous results are suggested.

ACKNOWLEDGEMENTS

I wish to express my gratitude to my supervisor, Dr. W.R. Datars, for his keen interest throughout my research and in the revisions and corrections to this thesis. I also wish to thank Mr. C.A. Verge for his assistance with many technical problems and all the other members of the Fermi surface group for many stimulating and fruitful discussions.

This research was supported by a research grant from the Natural Sciences and Engineering Research Council of Canada.

TABLE OF CONTENTS

PAGE

LIST OF TABLES

LIST OF TABLES

LIST OF FIGURES

FIGURE PAGE

CHAPTER I

INTRODUCTION

$Hg_{3-\delta}AsF_6$ and $Hg_{3-\delta}SbF_6$ are compounds that contain one-dimensional chains of mercury atoms running in two mutually perpendicular directions. Over the past ten years, there has been considerable interest in one-dimensional conductors. These compounds have been shown to exhibit many unusual properties: large anisotropy, metal-insulator transition, commensurate and incommensurate charge-density waves, nonstoichiometry.

As member of this vast family of coupounds, the mercury linear chain compounds also display some of these properties.

These compounds were discovered in the Chemistry Department of McMaster University by Gillespie and Ummat (1971) and the first single crystals were grown in the same laboratory (Cutforth, 1975). X-ray measurements by Brown et al (1974) showed that, at room-temperature, the mercury chains form a disordered system incommensurate with the tetragonal host lattice. At room-temperature, the chains, as a whole, are able to slide along their length with respect to one another and with respect to the hexafluoride anion lattice. Later neutron diffraction measurements (Pouget et al, 1978) confirmed these results and showed that as the temperature is lowered from room-temperature, parallel chains start to exhibit short-range order at 180 K and eventually, interaction between perpendicular chains produces long-range order at 120 K with no further crystallographic changes down to 10 K. Because, at low temperatures, there are three interpenetrating lattices with no common unit cell in the mercury linear chain compounds, they constitute a stepping stone between the ideal monoatomic crystal with infinite translational symmetry and the amorphous materials such as metallic glasses with no translational symmetry.

$Hg_{3-\delta}AsF_6$ and $Hg_{3-\delta}SbF_6$ are metallic down to 4.2 K. At room-temperature, the resistivity, in the plane containing chains, is of the order of 10^{-4} Ω-cm (Cutforth et al, 1977) placing these compounds among the best one-dimensional conductors. The resistivity along the c axis is one hundred times larger than in the plane of the chains for $Hg_{3-\delta}AsF_6$ and twenty times for $Hg_{3-\delta}SbF_6$.

The optical reflectivity (Koteles et al, 1976; Peebles et al, 1977) and the thermopower (Scholz et al, 1977) have also shown anisotropy in both compounds.

From differential thermal analysis, Datars et al (1978) have concluded that, upon cooling, mercury is extruded from these compounds between 195 and 215 K. This mercury returns to the chains when the sample is warmed back to 235 K. This phenomenon is a direct consequence of the incommensurability of the chains and is unique to these compounds.

Razavi _et al_ (1979) have measured the de Haas-van Alphen effect in $Hg_{3-\delta}AsF_6$ and determined from it that the Fermi surface of this compound consists of a group of cylinders aligned along the c axis. This was confirmed by the observation of an open orbit along the c direction using an induced torque method (Dinser _et al_, 1979). This constituted the first time that the Fermi surface of a one-dimensional conductor had been completely determined experimentally.

Chiang _et al_ (1977) have suggested that $Hg_{3-\delta}AsF_6$ becomes an anisotropic superconductor at 4.1 K. This anisotropy vanishes at 0.43 K and the compound becomes an ordinary superconductor according to magnetization measurements by Spal _et al_ (1979). This is of particular interest in view of a proposal by Little (1964) that one-dimensional conductors could become superconducting at temperatures higher than the highest T_c for three-dimensional superconductors.

Other properties have also been measured in $Hg_{3-\delta}AsF_6$: nuclear magnetic resonance (Ehrenfreund _et al_, 1977), specific heat (Wei _et al_, 1977), X-ray fluorescence (Spal _et al_, 1979).

In this work, a detailed model of the Fermi surface is investigated and expressions for the dHvA frequencies and cyclotron masses are derived. These are used to analyze our measurements of the de Haas-van Alphen effect in $Hg_{3-\delta}SbF_6$ at room-pressure and in $Hg_{3-\delta}AsF_6$ under hydrostatic pressures of up to 5 kbar.

Also, we have measured the resistivity of $Hg_{3-\delta}AsF_6$ from 4.2 to 300 K. A model of the lattice resistivity is constructed with the cylindrical Fermi surface and scattering by one-dimensional and three-dimensional phonons and is compared to the experimental results.

Finally, results of differential susceptibility measurements in $Hg_{3-\delta}AsF_6$ between 4.2 and 1.2 K are presented and hypotheses explaining the superconducting properties of this compound are discussed.

CHAPTER II

CRYSTAL STRUCTURE

The crystal structure of the mercury linear chain compounds, $Hg_{3-\delta}AsF_6$ and $Hg_{3-\delta}SbF_6$ was determined at room temperature by Brown et al (1974) using X-ray diffraction. They found that both compounds contain chains of mercury atoms in channels of a tetragonal lattice of octahedral anions. For $Hg_{3-\delta}AsF_6$, Pouget et al (1978) confirmed these results at room-temperature and extended these measurements down to 10 K using neutron scattering. They found that the two mutually perpendicular sets of mercury chains order below 120 K.

At room temperature, the hexafluoride anions in $Hg_{3-\delta}AsF_6$ and $Hg_{3-\delta}SbF_6$ form a body-centered tetragonal lattice with a basis of two anions. One possible set of primitive translation vectors for this lattice is given by

$$\vec{a}_1 = (a,0,0)$$

$$\vec{a}_2 = (0,a,0)$$

$$\vec{a}_3 = (\tfrac{a}{2},\tfrac{a}{2},\tfrac{c}{2})$$

relative to a set of cartesian coordinates with the z axis along the four-fold symmetry axis of the tetragonal lattice (Fig. II.1). An anion at the origin of the axes together with one at $(0,\frac{a}{2},\frac{c}{4})$ form the basis of the structure.

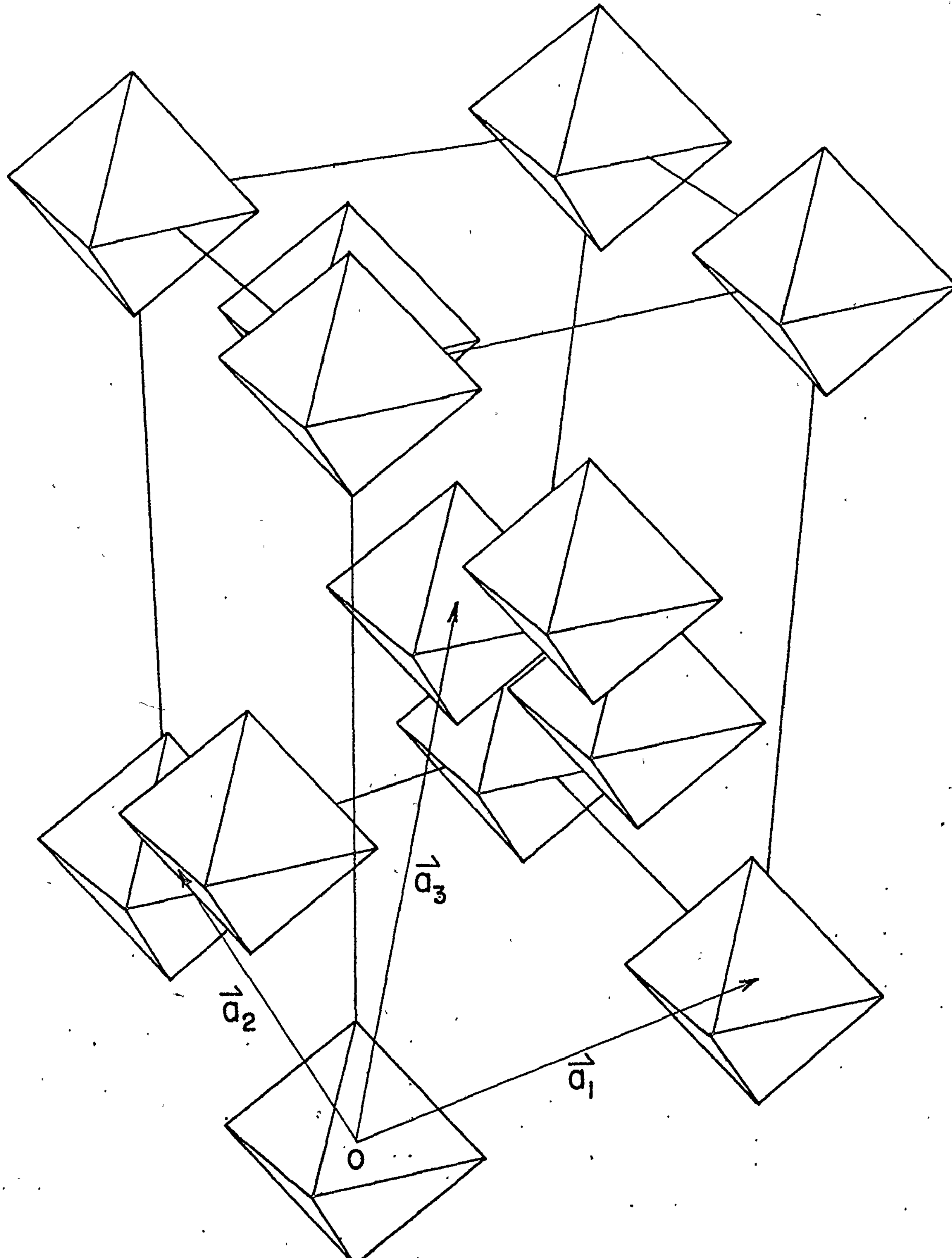

Figure II:1
Perspective view of the hexafluoride anions' lattice with unit cell represented by solid lines and primitive vectors $\vec{a}_1$, $\vec{a}_2$ and $\vec{a}_3$.

There are channels along the x and y axis of this anion structure intersecting the boundaries of the tetragonal unit cell at $(0,0,\frac{3}{8})$, $(0,\frac{1}{2},\frac{7}{8})$ and at $(\frac{1}{2},0,\frac{1}{8})$, $(0,0,\frac{5}{8})$ respectively. These channels do not intersect because the channels along the x and y directions are a distance $\frac{c}{4}$ apart along the z-direction. The mercury atoms are located in these channels. Table II.1 contains crystal structure parameters for $Hg_{3-\delta}AsF_6$ and $Hg_{3-\delta}SbF_6$.

The mercury-mercury distance along a channel direction, d, is not commensurate with the tetragonal lattice parameter, a. This means that we cannot find two small integer numbers, m and n, such that

$$md = na \ .$$

We then define δ, the ratio of the difference between three mercury-mercury separations and the lattice parameter of the tetragonal lattice, to d, the mercury-mercury distance

$$\frac{a}{d} = 3 - \delta \ .$$

The formula for these compounds is then given by $Hg_{3-\delta}AsF_6$ and $Hg_{3-\delta}SbF_6$.

Also, because they observed sheets of diffuse scattering in X-ray photographs of these compounds with a precession camera, Brown <u>et al</u> (1974) concluded that there is no ordering of the position of Hg atoms in adjacent parallel chains. However, along one chain, it was shown later (Pouget <u>et al</u>, 1978) that the mercury atoms exhibit long range order of their positions over more than 150 Hg-Hg spacings.

Table II.1 Crystal structure parameters for $Hg_{3-\delta}AsF_6$ and $Hg_{3-\delta}SbF_6$

	$Hg_{3-\delta}AsF_6$			$Hg_{3-\delta}SbF_6$
Space group	$I4_1/amd$ (no 141, D_{4h}^{19})			$I4_1/amd$ (no 141, D_{4h}^{19})
Bravais lattice	Body-centered tetragonal			Body-centered tetragonal
Number of formula units/primitive cell	2			2
Temperature	295 K [a]	295 K [b]	10 K [b]	295 K [c]
Cell constants				
a	7.538(4) Å	7.531 Å	7.443 Å	7.699(3) Å
c	12.339(5) Å	12.395 Å	12.248 Å	12.610(4) Å
Mercury-mercury distance along channels				
d	2.64(1) Å	2.670(5) Å	2.670(5) Å	2.64 (1) Å
Smallest distance between perpendicular chains				
c/4	3.085(1) Å	3.099 Å	3.062 Å	3.153(1) Å

a Brown et al (1974)

b Pouget et al (1978)

c Cutforth (1975)

In $Hg_{3-\delta}AsF_6$, when the temperature is lowered from room-temperature to 10 K, the tetragonal crystal lattice parameters decrease by 1% while the Hg-Hg distance remains the same. Therefore, δ goes from 0.18 at room-temperature to 0.21 at 10 K. If we could write

$$md = na$$

using large integers m and n assuming that the compound is commensurate with a large unit cell, then a and d would change by the same relative amount when the temperature is lowered. This does not occur and the invariance of the mercury-mercury distance with temperature is further evidence of the incommensurability of the Hg chains.

At 120 K, the mercury atoms in parallel chains are observed to order in $Hg_{3-\delta}AsF_6$. If a mercury atom is at the origin of the x axis for a chain going in the x direction, then, on the parallel chain a distance a along the y axis, there is a mercury atom with a coordinate along the x-axis of $\pm\ \delta d$. In the chains that are one lattice parameter c from the two above, mercury atoms are at the same positions along the x axis while the atoms in the chains at $\frac{c}{2}$ are in body-center positions (Fig. II.2). If the sign of the displacement of the mercury atoms in going from a chain to the next parallel one is the same for both the chains along the x and y axes, the two structures have common reciprocal points of the form

Figure II.2

Arrangement of mercury atoms for one set of chains below 120 K. Circles represent mercury atoms in the ab plane and concentric circles represent mercury atoms c/2 above that plane.

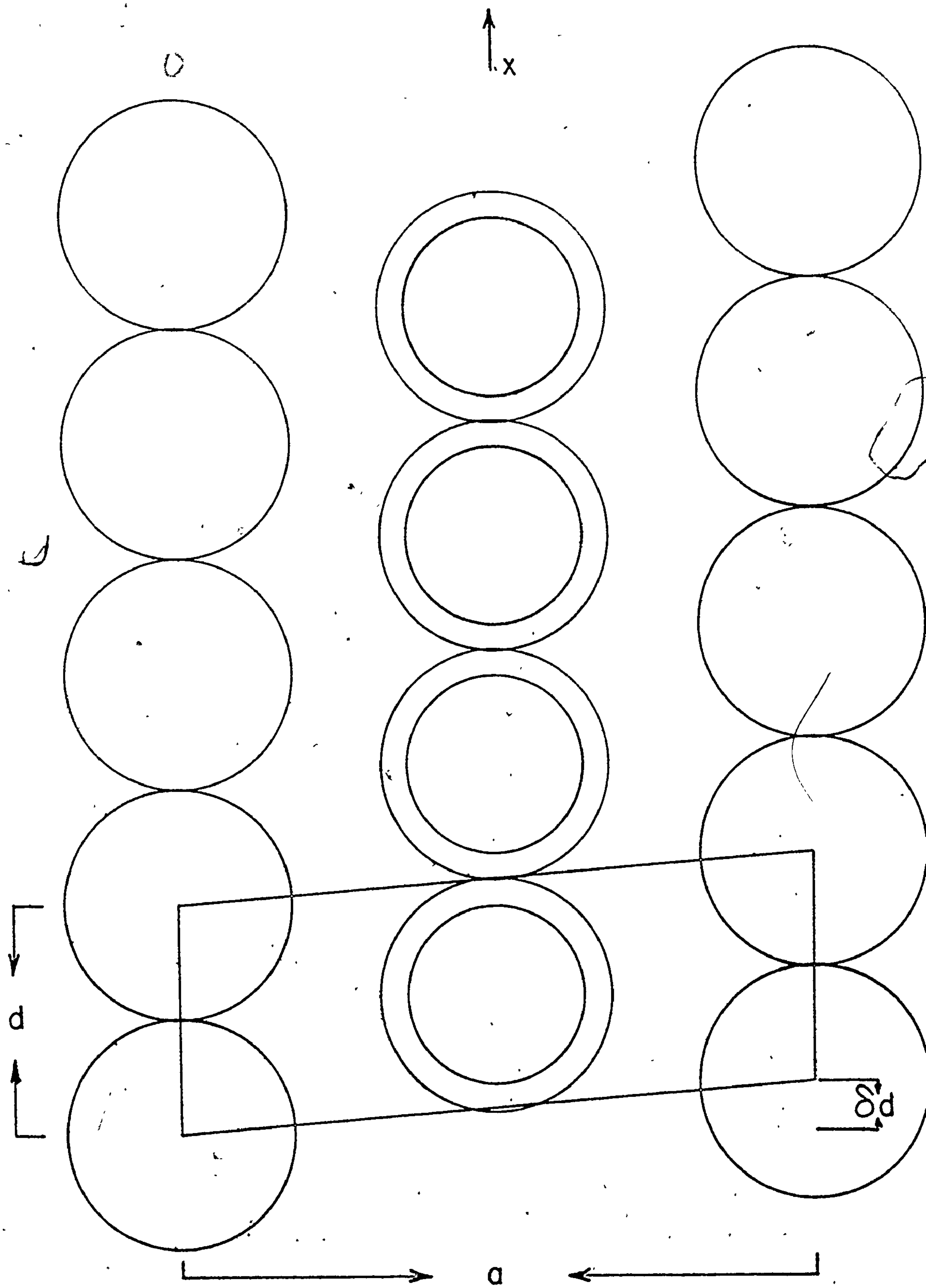
x
d
δd
a

$$(h,k,\ell) = n(3-\delta,3-\delta,0) \ .$$

This means that there is some interaction between perpendicular chains. This is not unexpected since the distance of closest approach between perpendicular chains (3.085 Å at room temperature) is not very different from the mercury-mercury distance in metallic mercury (3.005 Å). Also, Pouget et al (1978) report that the $(6-2\delta,6-2\delta,0)$ peak is detected while the $(3-\delta,3-\delta,0)$ is not. They conclude from this that the two sets of chains have arranged their phase in the manner shown in Fig. II.3. The [110] planes containing the mercury atoms on the chains going in the x direction are exactly halfway between the planes containing the mercury atoms from the chains along the y axis. This insures that mercury atoms on perpendicular chains never get closer than $\sqrt{\frac{c^2}{16} + \frac{d^2}{8}}$. By keeping the positive ions apart, the electrostatic energy is minimized.

Finally, because there is a choice of sign in the relative displacement of the parallel chains, there will be domains of both types in a crystal. Also, Pouget et al (1978) noted that rapid cooling through the transition at 120 K down to 10 K could prevent the ordering of the parallel mercury chains. Both of these effects could cause crystals to have non-uniform structure at low temperatures.

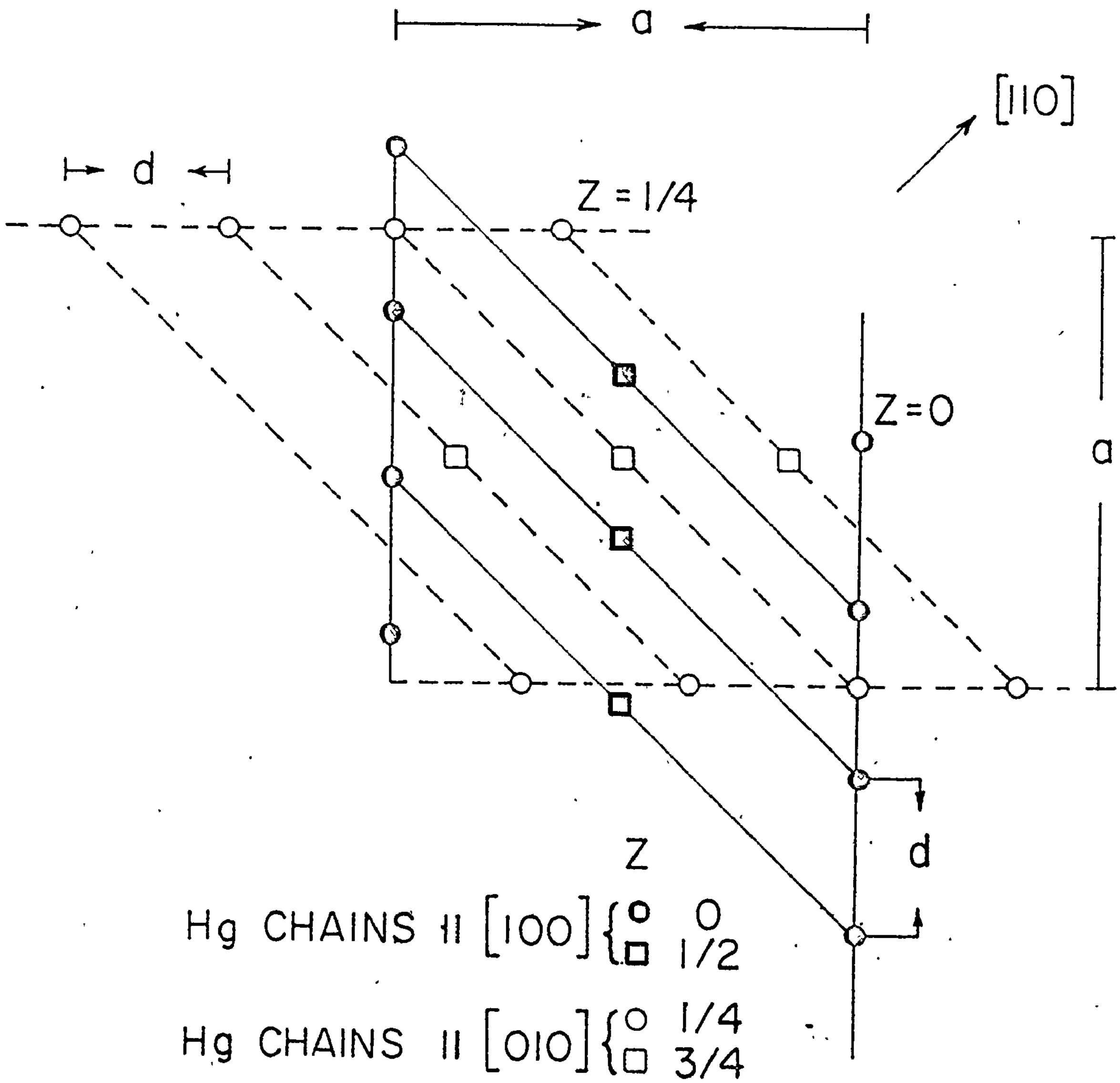

Figure II.3

Mercury chains below 120 K. Dashed and solid lines represent alternating (110) planes of mercury atoms belonging to the two sets of chains.

CHAPTER III

FERMI SURFACE

a. Introduction

Razavi et al (1979) suggested a model of the Fermi surface of $Hg_{3-\delta}AsF_6$. This model is analyzed and used to fit our measurements of the Fermi surface of the other mercury linear chain compound, $Hg_{3-\delta}SbF_6$, the cyclotron masses for both compounds and the Fermi surface of $Hg_{3-\delta}AsF_6$ under hydrostatic pressure.

b. Fermi surface model

The electrical and optical properties of $Hg_{3-\delta}AsF_6$ and $Hg_{3-\delta}SbF_6$ are anisotropic and metallic which suggests that the conduction electrons are localized in the channels containing the mercury chains. In this model, there is ionic bonding between the positively charged mercury chains and the hexafluoride anions, and metallic bonding between mercury atoms along a chain. The 6s valence electrons of the Hg atoms not required for the ionic bond participate in the metallic bond.

Since the Hg-Hg distance is incommensurate with the tetragonal lattice parameter of the hexafluoride anions, the whole crystal is the smallest unit cell that can be constructed. Tnis makes it impossible to use any of the techniques used to calculate the energy band structure of the electrons in other metals. This problem is eliminated in a suggestion by A.J. Berlinsky (1978) that the Hg ions can be ignored along the chains so that the electrons move in a cylindrically symmetric uniform potential along the direction of the chains. Then this potential obeys the same symmetry operations as the lattice of hexafluoride anions.

Considering one set of chains along one direction and ignoring the position of the Hg atoms in them, these chains can be regarded as forming a two-dimensional structure. The unit cell and the reciprocal lattice of this structure are shown in Fig. III.1.

It is assumed that these chains do not interact. This implies that, in the dispersion relation

$$\varepsilon = \varepsilon(\vec{k})$$

the energy depends only on the component of $\vec{k}$ along the chain.

The Fermi wavevector along the chain, k_F, is determined by filling the lower energy states with all the available valence electrons. Each mercury atom contributes two valence electrons but one electron for every $(3-\delta)$ mercury atoms is used in bonding the mercury chain to the hexafluoride anions. If the chain's length is L, then the number of mercury atoms along a chain is L/d where d is the mercury-mercury distance. The total number of electrons is

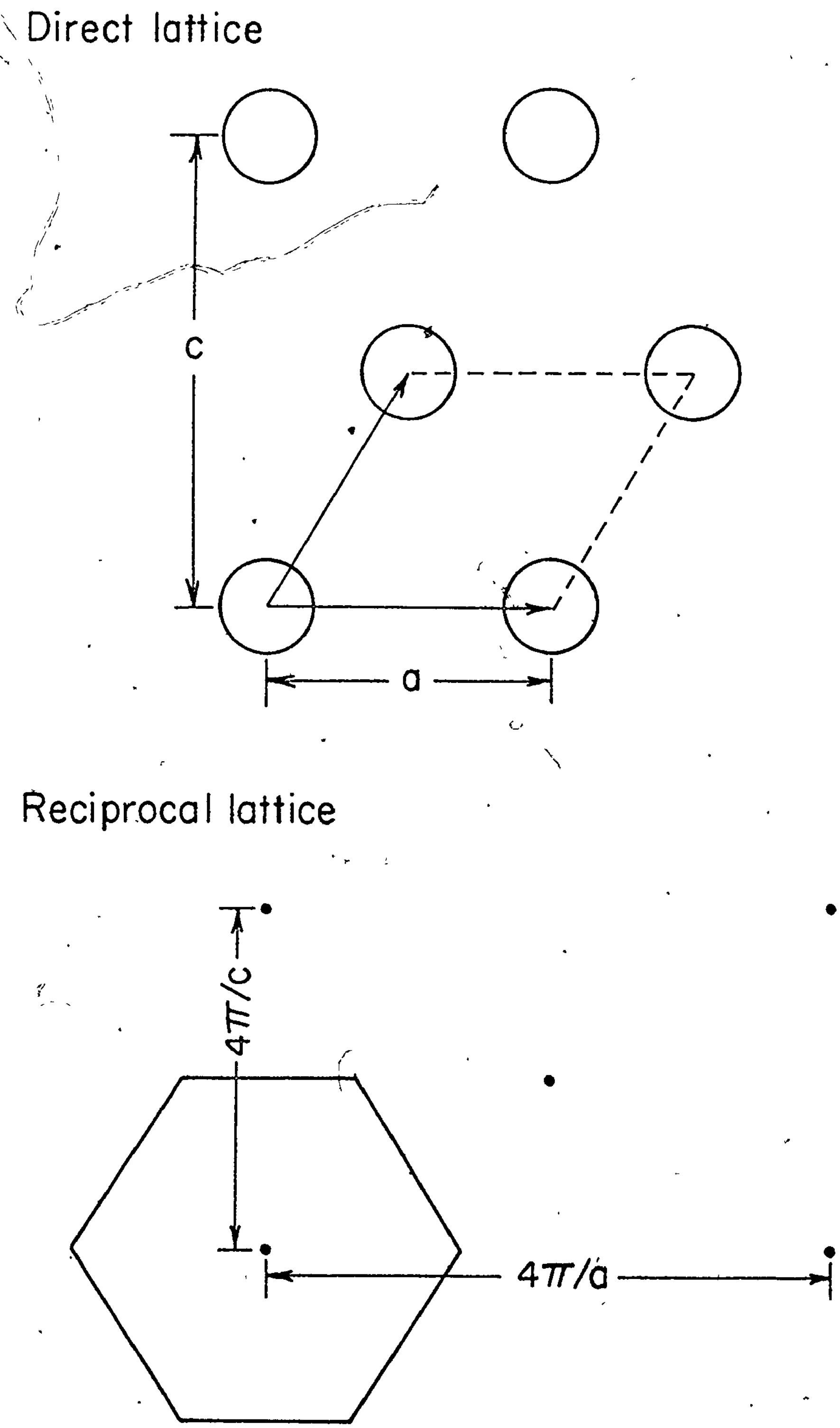

Figure III.1

Direct and reciprocal lattice for one set of chains. Dashed and solid lines represent unit cell and Brillouin zone.

$$N_e = \frac{L}{d}\left(2 - \frac{1}{3-\delta}\right)N_c \qquad \text{(III.1)}$$

where N_c is the number of chains. The Brillouin zone (BZ) will be full in the plane perpendicular to the chain because in that plane, the energy is independent of $\vec{k}$. There will not be any occupied states outside this Brillouin zone because our model consists of a tight binding band in the interchain directions limited to one orbital on each chain with negligible overlap. This will account for 2 N_c filled states for each value of the wavevector along the chain. Equating the number of states occupied to the total number of electrons available, we get

$$\left(2k_F * \frac{L}{2\pi}\right) * 2N_c = \frac{L}{d}\left(2 - \frac{1}{3-\delta}\right)N_c \qquad \text{(III.2)}$$

where $\frac{L}{2\pi}$ is the density of states for wavevectors along the chain. Therefore,

$$k_F = \frac{\pi(2.5-\delta)}{a} . \qquad \text{(III.3)}$$

The Fermi surface for one set of chains consists of two planes perpendicular to the direction of the chains at $+k_F$ and $-k_F$.

There are two sets of mutually perpendicular chains inserted in the lattice of the hexafluoride anions. If the chains are considered to be structureless, then they belong to the same crystal group as the anions, $I^{4_1}_{amd}$. The corresponding Bravais lattice is body-centered tetragonal and the Brillouin zone and a few planes of the reciprocal lattice for this structure are shown in Fig. III.2

The Fermi surface for the two perpendicular sets of chains is then drawn at every reciprocal lattice point. The resulting Fermi surface consists of four planes parallel to k_z at $\pm \frac{\pi}{a}(0.5-\delta)$ along k_x and k_y in the third BZ (Fig. III.3). Since there is no variation of the Fermi surface along k_z in our model, it is sufficient to look at the $k_z = 0$ cross-section.

In that plane, there are four crossings of the Fermi surfaces of the two sets of chains at $(\pm \frac{\pi}{a}(0.5-\delta), \pm \frac{\pi}{a}(0.5-\delta))$. The minimum separation of mercury atoms on perpendicular chains is comparable to the Hg-Hg distance in metallic mercury and the interaction between these chains will remove the degeneracies at the crossings of the Fermi surfaces of the two sets of chains to produce the cross-section shown in Fig. III.3.

This Fermi surface consists of two square cylinders: one electron cylinder centered at Γ and a hole cylinder centered at X. Written in terms of 'a' and δ, their cross-sectional areas are given by

$$\text{Area(electron)} = [\frac{\pi}{a}(1-2\delta)]^2 \qquad \text{(III.4)}$$

$$\text{Area(hole)} = [\frac{\pi}{a}(1+2\delta)]^2 \qquad \text{(III.5)}$$

For $Hg_{3-\delta}AsF_6$, Pouget et al (1978) obtained

$$\delta = 0.21$$
$$a = 7.443 \text{ Å}$$

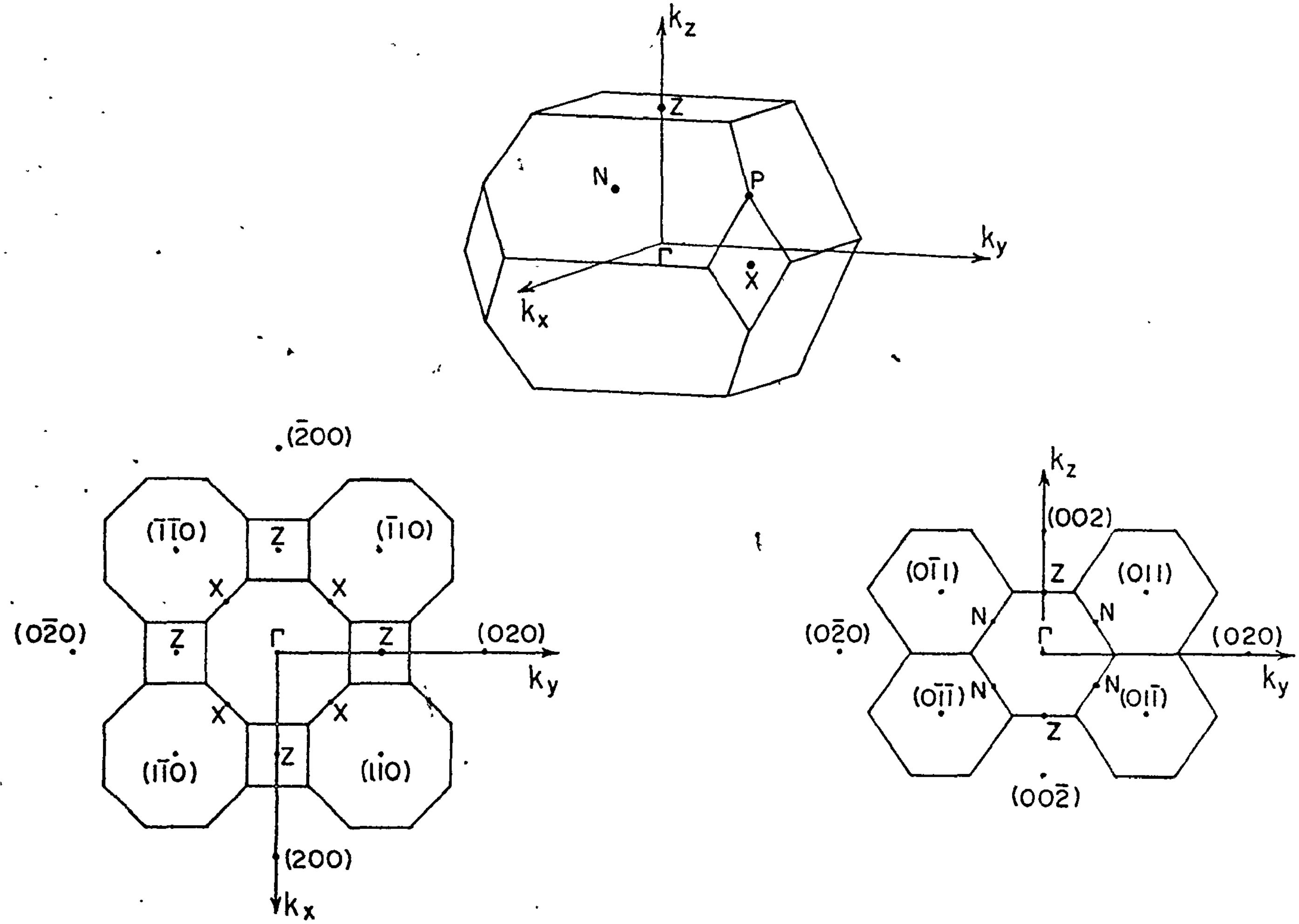

Figure III.2

Three-dimensional view of the Brillouin zone of the body-centred tetragonal lattice together with (001) and (100) planes of the reciprocal lattice.

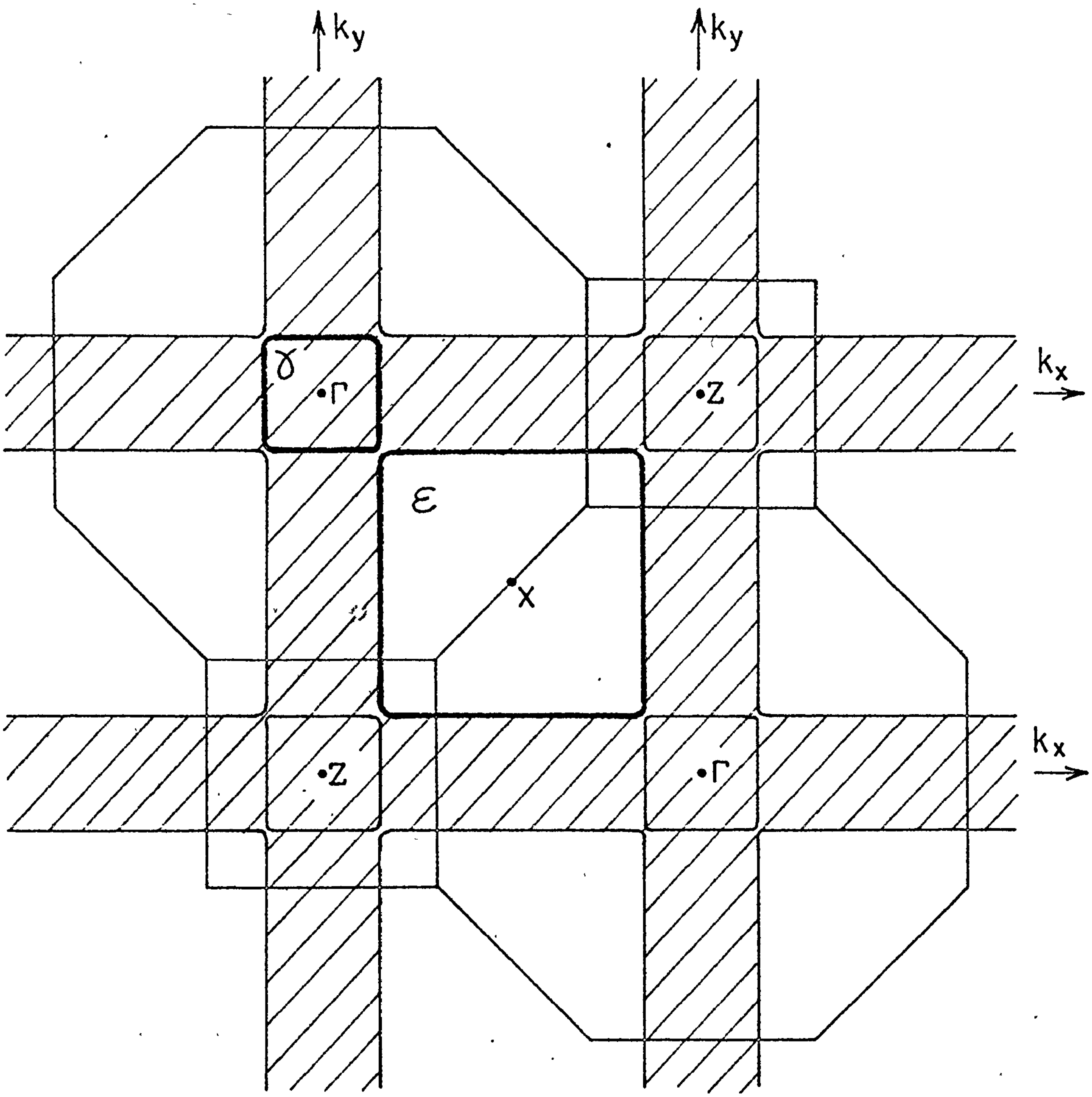

Figure III.3

Cross-section of the Fermi surface in the (001) plane. Hashed regions contain occupied states. The electron orbit, γ, and the hole orbit, ε, are outlined.

from neutron diffraction experiments at 10 K. With these values, Razavi et al (1979) obtained a good agreement between eqs. III.4 and III.5, and the cross-sectional areas corresponding to the γ and ε branches of their de Haas-van Alphen (dHvA) frequencies measurements (Table III.1).

Therefore, it is reasonable to consider the mercury chains as structureless in a first approximation. This is physically sound at room-temperature where there is no ordering between chains. However, below 120 K, the two sets of chains order and form two reciprocal lattices with common reciprocal points at

$$\vec{G} = n(3-\delta, 3-\delta, 0)$$

As in the case of spin density waves in chromium (Lomer, 1965), the crystal potential of the mercury chains opens energy gaps in the vicinity of any pair of states on the Fermi surface which are separated by $\vec{q}$

$$\vec{q} = \vec{G}(XF_6 \text{ lattice}) - \vec{G}(\text{chains}) \qquad \text{(III.6)}$$

The smallest non zero $\vec{q}$ is given by

$$\vec{q} = \frac{2\pi}{a}(\delta, \pm\delta, 0)$$

where the choice of signs corresponds to two possible domains in the crystal. The location of the energy gaps is found by displacing the Fermi surface by $\vec{q}$ and superposing this trans-

Table III.1 Experimental and theoretical dHvA frequencies and corresponding Fermi surface cross-sectional areas for $Hg_{3-\delta}AsF_6$

Orbit	Experiment		Theory	
	Freq. (T)	Area ($Å^{-2}$)	Freq. (T)	Area ($Å^{-2}$)
α^*	48	0.0046	48	0.0046
α	340	0.0325	298	0.0285
γ	626	0.0598	627	0.0599
δ	1860	0.1777	1865	0.1781
μ	3413	0.3260	3432	0.3278
ε	3680	0.3515	3761	0.3592

lated surface on the original, as shown in Fig. III.4. If the energy gap at all the crossing points is very large, the set of orbits shown in Fig. III.5 is obtained.

The orbits γ and ε have been destroyed by the extra gaps and there are four new orbits: two electron orbits, α^* and $\maltese$, one hole orbit δ, and one open orbit. In $Hg_{3-\delta}AsF_6$ orbits δ and α^* have been observed but the orbits γ and ε have also been observed in dHvA experiments (Razavi et al, 1979) while no open orbits in the ab plane were detected using an induced torque magnetometer (Dinser et al, 1979). From this, it is inferred that the energy gaps caused by the extra periodicity associated with the mercury chains are small enough to permit magnetic breakdown across them. Assuming that all first order gaps are the same, we call the corresponding breakdown probability, q, and determine all the possible orbits if this probability is of the order of 0.5.

Figures III.3 to III.5 have been obtained with a δ of 0.21, the value for $Hg_{3-\delta}AsF_6$ at 10 K. There is no low temperature crystallographic measurement of the incommensurability parameter, δ, for $Hg_{3-\delta}SbF_6$. However, knowing that δ has a value of 0.09 at room-temperature and assuming that the SbF_6 lattice contracts by 1% when the crystal is cooled to 1.25 K, we estimate

$$\delta(1.25\ \mathrm{K}) \doteq 0.09+0.01*3 = 0.12\ .$$

The difference in δ for the arsenic ~~and antimony~~ com-

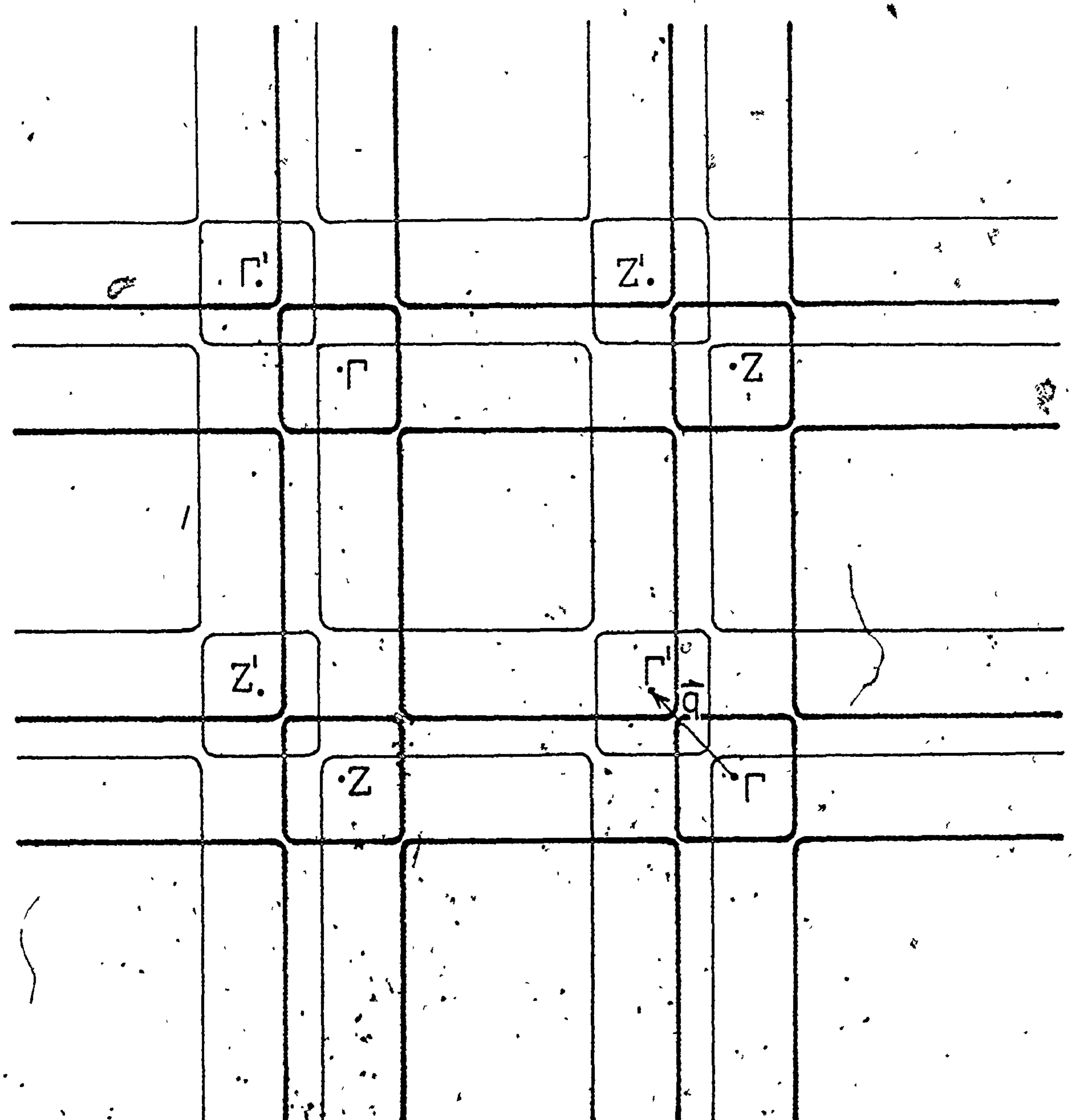

Figure III.4

Fermi surface translated by $\vec{q}$ (light) on to the original Fermi surface (dark).

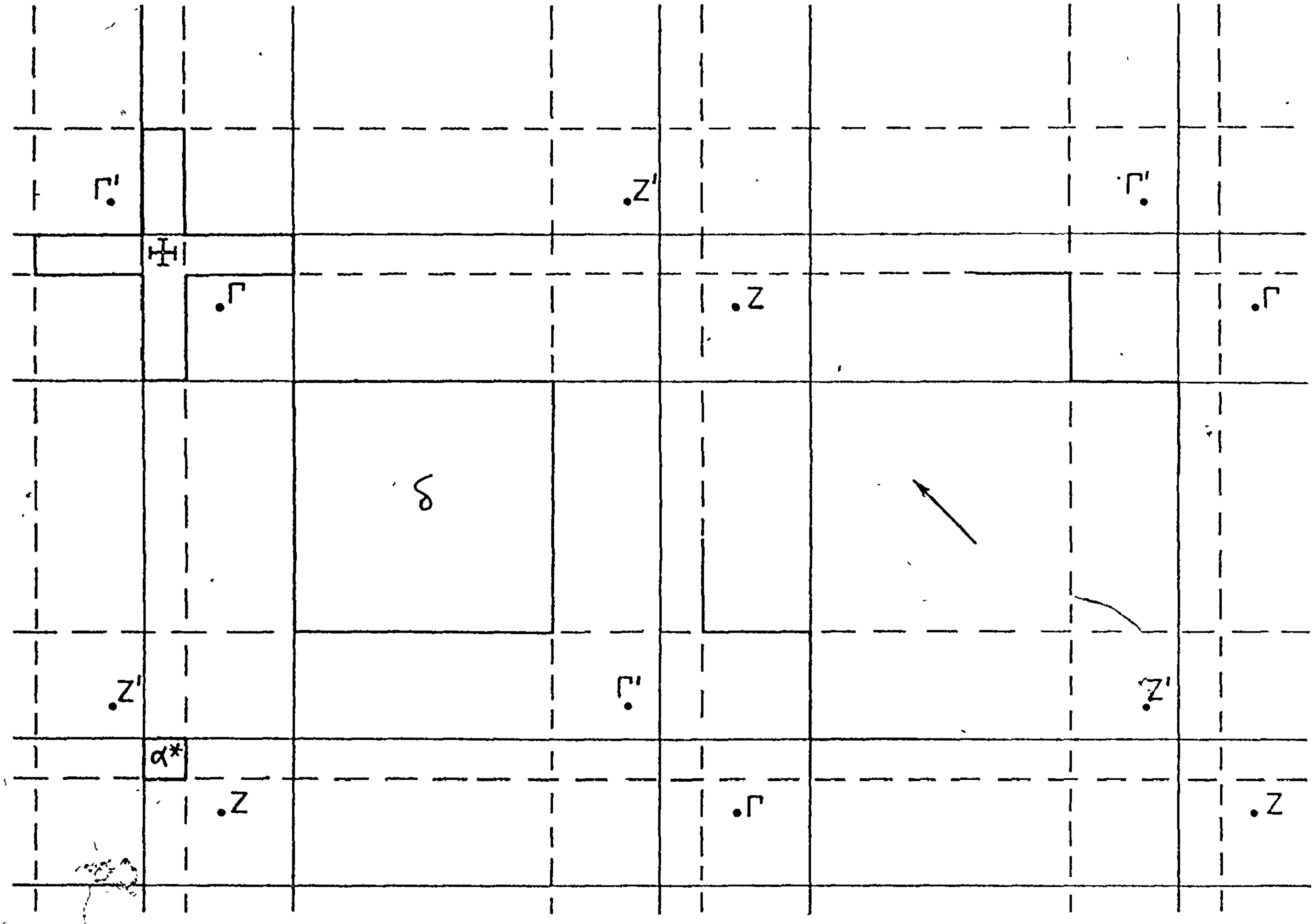

Figure III.5

Closed orbits α^*, δ and $+$ and an open orbit along the direction of the arrow (dark outlines) which are obtained when the gaps at the intersections of the original Fermi surface (solid lines) and the translated Fermi surface (dashed lines) are large.

pounds produces large differences in the areas of the possible orbits but it does not change the geometry of the Fermi surface except for some of the more complicated orbits. Common orbits are shown in Fig. III.6 and III.7 for $Hg_{3-\delta}AsF_6$ and $Hg_{3-\delta}SbF_6$, respectively. The cross-sectional areas corresponding to these orbits and some others are listed in Table III.2 together with their probabilities of occurrence in both compounds.

In $Hg_{3-\delta}AsF_6$, the electron orbits α, α^* and γ and the hole orbits δ, ε and μ are observed in the dHvA data of Razavi et al (1979) (Table III.1). Our assignment of the orbit corresponding to frequency α is different from the assignment of Razavi et al. The orbit they had chosen (Fig. III.6) is an interferometric orbit (Stark and Friedberg, 1971) which can not be observed directly in dHvA experiments. The probabilities associated with the orbits that are observed are of low order in (1-q) confirming our earlier suggestion that q is large. Also, the probability of orbit μ, which was shown to disappear below 4.6 Teslas in $Hg_{3-\delta}AsF_6$, contains the largest power of q.

The area of the δ orbit depends only on the lattice parameter a; the ratios of the area of the other orbits to the area of the δ orbit are then simple functions of δ, the incommensurability parameter. These are listed in Table III.2 and are plotted against δ in Fig. III.8 for values of δ between 0.10 and 0.22.

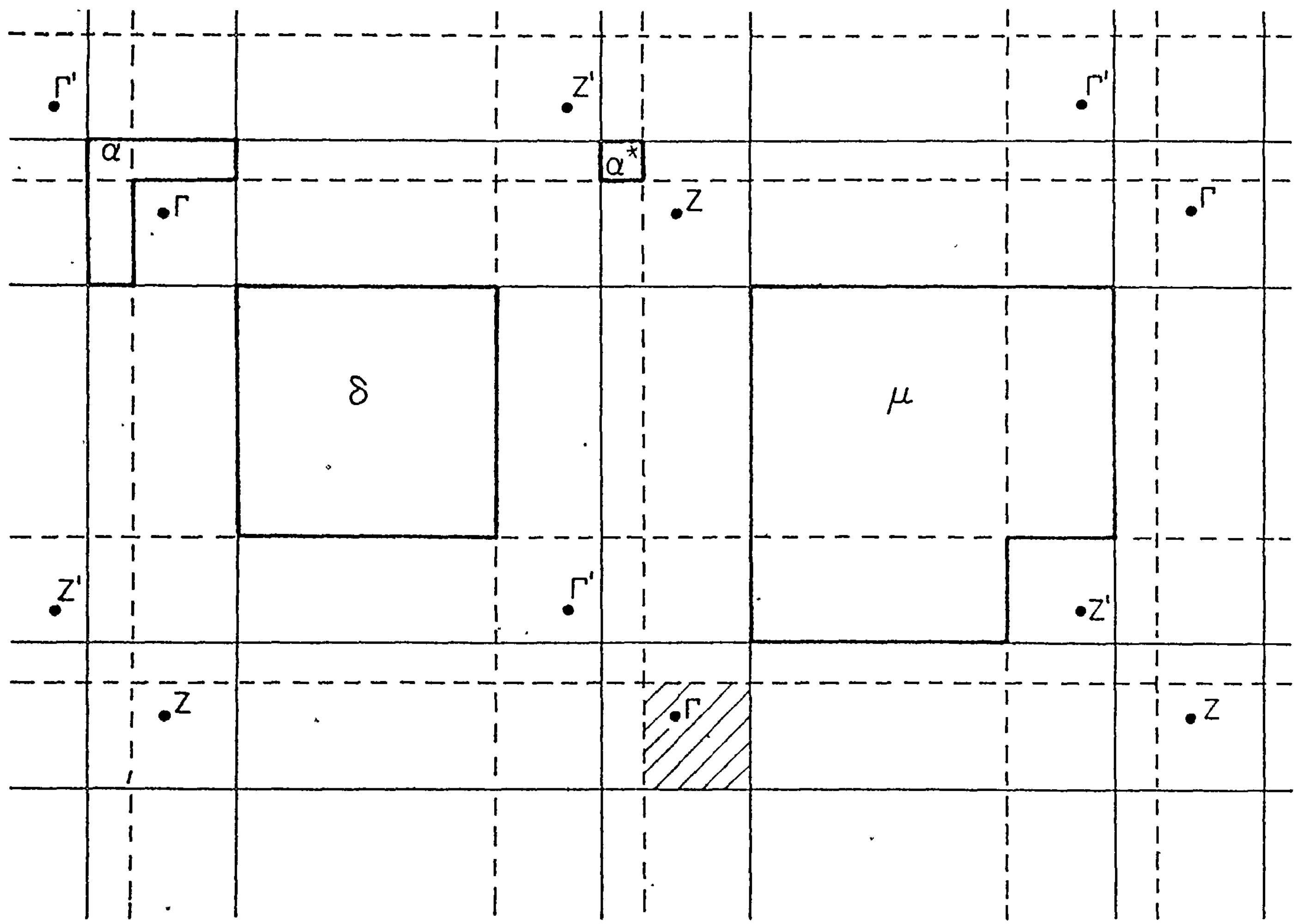

Figure III.6

Orbits α*, α, δ, μ for $Hg_{3-\delta}AsF_6$ (dark outlines). The contour of the hashed area represents the interferometric orbit previously used to fit frequency α.

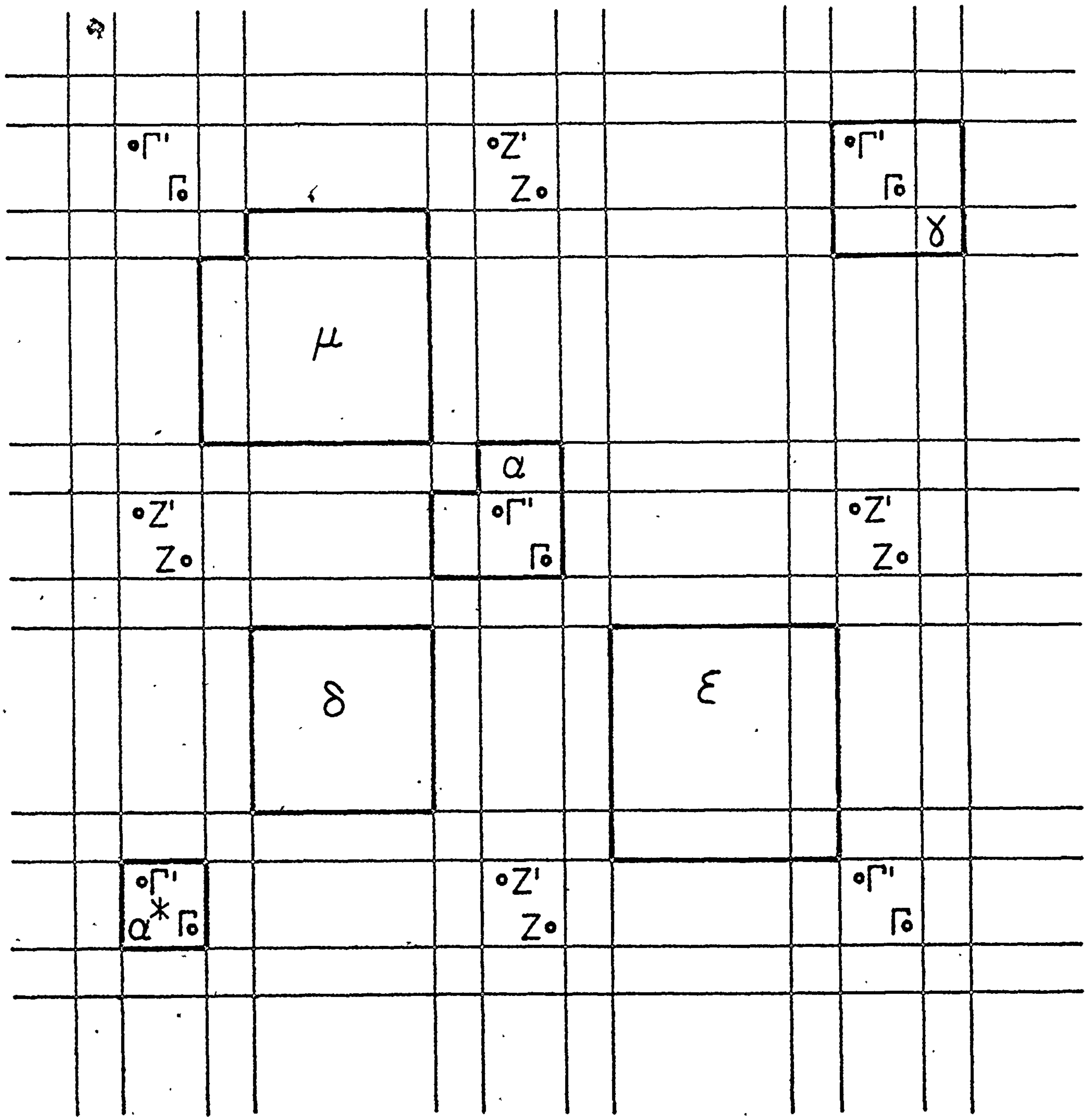

Figure III.7

Orbits α*, α, γ, δ, μ and ε for $Hg_{3-\delta}SbF_6$.

Table III.2 Areas and probabilities of occurrence of possible orbits associated with our Fermi surface model of the mercury chain compounds. Ratios of the cross-sectional areas to the area corresponding to the δ orbit are also shown.

Orbit	Area	Probability $Hg_{3-\delta}AsF_6$	Probability $Hg_{3-\delta}SbF_6$	$\frac{\text{Area}}{\text{Area }(\delta)}$
γ	$\frac{\pi^2}{a^2}(1-2\delta)^2$	q^8	q^8	$(1-2\delta)^2$
ε	$\frac{\pi^2}{a^2}(1+2\delta)^2$	q^8	q^8	$(1+2\delta)^2$
μ	$\frac{\pi^2}{a^2}(1+4\delta)$	$(1-q)^2q^8$	$(1-q)^2q^6$	$(1+4\delta)$
α	$\frac{\pi^2}{a^2}(1-4\delta)$	$(1-q)^2q^4$	$(1-q)^2q^6$	$(1-4\delta)$
δ	$\frac{\pi^2}{a^2}$	$(1-q)^2q^4$	$(1-q)^2q^4$	1
α^*	$\frac{\pi^2}{a^2}(1-4\delta)^2$	$(1-q)^2$	$(1-q)^2q^4$	$(1-4\delta)^2$
$2\gamma-\alpha^*$	$\frac{\pi^2}{a^2}(1-8\delta^2)$	$(1-q)^2q^{12}$	$(1-q)^2q^8$	$(1-8\delta^2)$
$2\varepsilon-\delta$	$\frac{\pi^2}{a^2}(1+8\delta+8\delta^2)$	$(1-q)^2q^{10}$	$(1-q)^2q^8$	$(1+8\delta+8\delta^2)$
$\gamma+\alpha-\alpha^*$	$\frac{\pi^2}{a^2}(1-12\delta^2)$	$(1-q)^4q^8$	$(1-q)^4q^6$	$(1-12\delta^2)$
$2\varepsilon-\delta-\alpha'$	$\frac{\pi^2}{a^2}(1+8\delta+4\delta^2)$	$(1-q)^4q^{10}$	$(1-q)^4q^6$	$(1+8\delta+4\delta^2)$
$\delta-\alpha'$	$\frac{\pi^2}{a^2}(1-4\delta^2)$	$(1-q)^4q^4$	$(1-q)^4q^2$	$(1-4\delta^2)$

Figure III.8

Theoretical ratios of the α^*, α, γ, μ and ε frequencies to the δ frequency as a function of the incommensurability parameter, δ (solid lines). Dots and squares are placed on these lines at the experimental values of these ratios for $Hg_{3-\delta}SbF_6$ and $Hg_{3-\delta}AsF_6$ respectively.

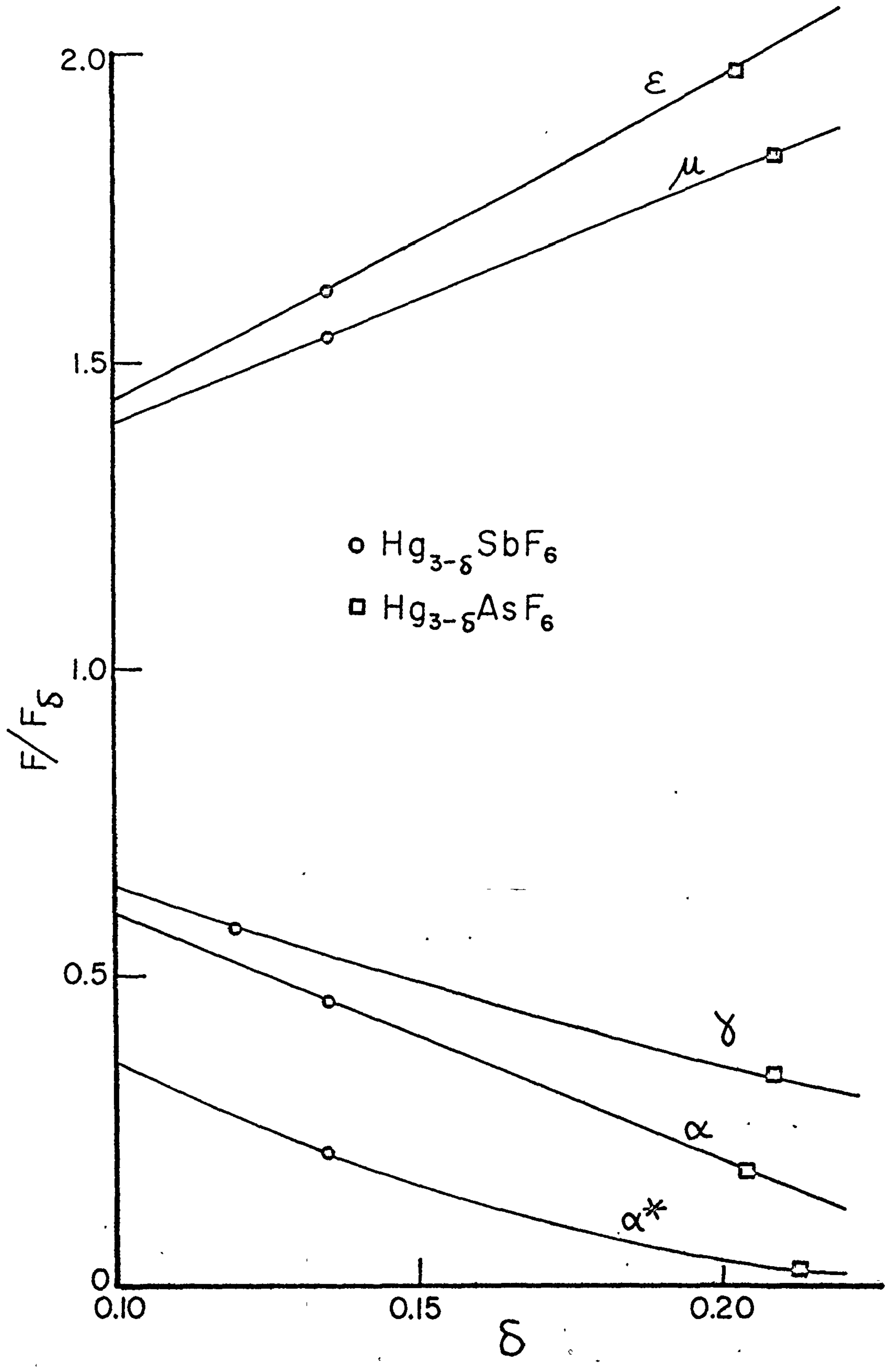

2.0
1.5
1.0
0.5
0
F/Fδ
ε
μ
γ
α
α*
o Hg3-δSbF6
□ Hg3-δAsF6
0.10
0.15
0.20
δ

Since all the orbits obtained above are cylindrical, their cross-sectional areas measured in the dHvA experiments vary as $\sec\theta$ where θ is the angle between the c axis and the magnetic field. The ratio of the cross-sectional areas should be independent of θ and provide a very accurate value of δ at low temperatures.

The cyclotron mass for an orbit of area A is given by

$$m^* = \frac{\hbar^2}{2\pi}\frac{\partial A}{\partial E} . \tag{III.8}$$

In our model, the energy, E, is only a function of the component of the wavevector along the chain, $k_{||}$, and the area of the most probable orbits is given by

$$A_\gamma = [2k_{||} - \frac{4\pi}{a}]^2 \tag{III.9a}$$

$$A_\varepsilon = [\frac{6\pi}{a} - 2k_{||}]^2 \tag{III.9b}$$

$$A_\delta = [\frac{6\pi}{a} - 2k_{||} - \frac{2\pi}{a}\delta]^2 \tag{III.9c}$$

$$A_\alpha = A_\gamma - \frac{4\pi^2}{a^2}\delta^2 \tag{III.9d}$$

$$A_\mu = A_\varepsilon - \frac{4\pi^2}{a^2}\delta^2 . \tag{III.9e}$$

so that, for orbits γ, ε and δ, we have

$$m_\gamma^* > 0 \quad , \quad m_\delta^*, m_\varepsilon^* < 0 \tag{III.10}$$

and

$$|m^*| = \frac{2\hbar^2}{\pi}\sqrt{A}\, k'_{||}$$

where

$$k'_{||} = \frac{dk_{||}}{dE} .$$

Assuming a strictly free electron dispersion relation along the chain

$$|m^*| = \frac{2m}{\pi} \sqrt{\frac{A}{k^2_{||}}}$$

where m is the free-electron mass.

There are two pairs of orbits with the same mass:

$$m^*_\alpha = m^*_\gamma$$

and

$$m^*_\mu = m^*_\varepsilon .$$

c. de Haas van Alphen Effect

The de Haas van Alphen (dHvA) effect is an oscillating behaviour of the magnetic susceptibility which is periodic in the inverse of the magnetic field. The frequencies contained in these oscillations are proportional to extremal cross-sectional areas of the Fermi surface perpendicular to the field.

Analysis of the dHvA effect in $Hg_{3-\delta}AsF_6$ shows that there are five frequency branches which have a minimum when the magnetic field is along the c axis as shown in Fig. III.9 (Razavi et al, 1979). Measurements of the dHvA effect in $Hg_{3-\delta}SbF_6$, the other mercury linear chain compound, will be discussed and the one-dimensional band model with incommensurate translation will be used to fit these results. Accurate measurements of the cyclotron masses in both compounds will also be presented.

1. Apparatus

The samples used in the de Haas van Alphen (dHvA) experiments are approximately 5×2×1 mm^3. They are mounted inside Kel-F cylinders 2.5 cm long having a diameter of 3 mm. These cylinders are bored out for half their length and the sample is placed inside that cavity with the c axis, determined by visual observation of the sample, perpendicular to the cylinder axis. The sample is firmly held in place by filling the rest of the cavity with teflon tape. These Kel-F holders are installed in a hole extending across the Kel-F former of a de-

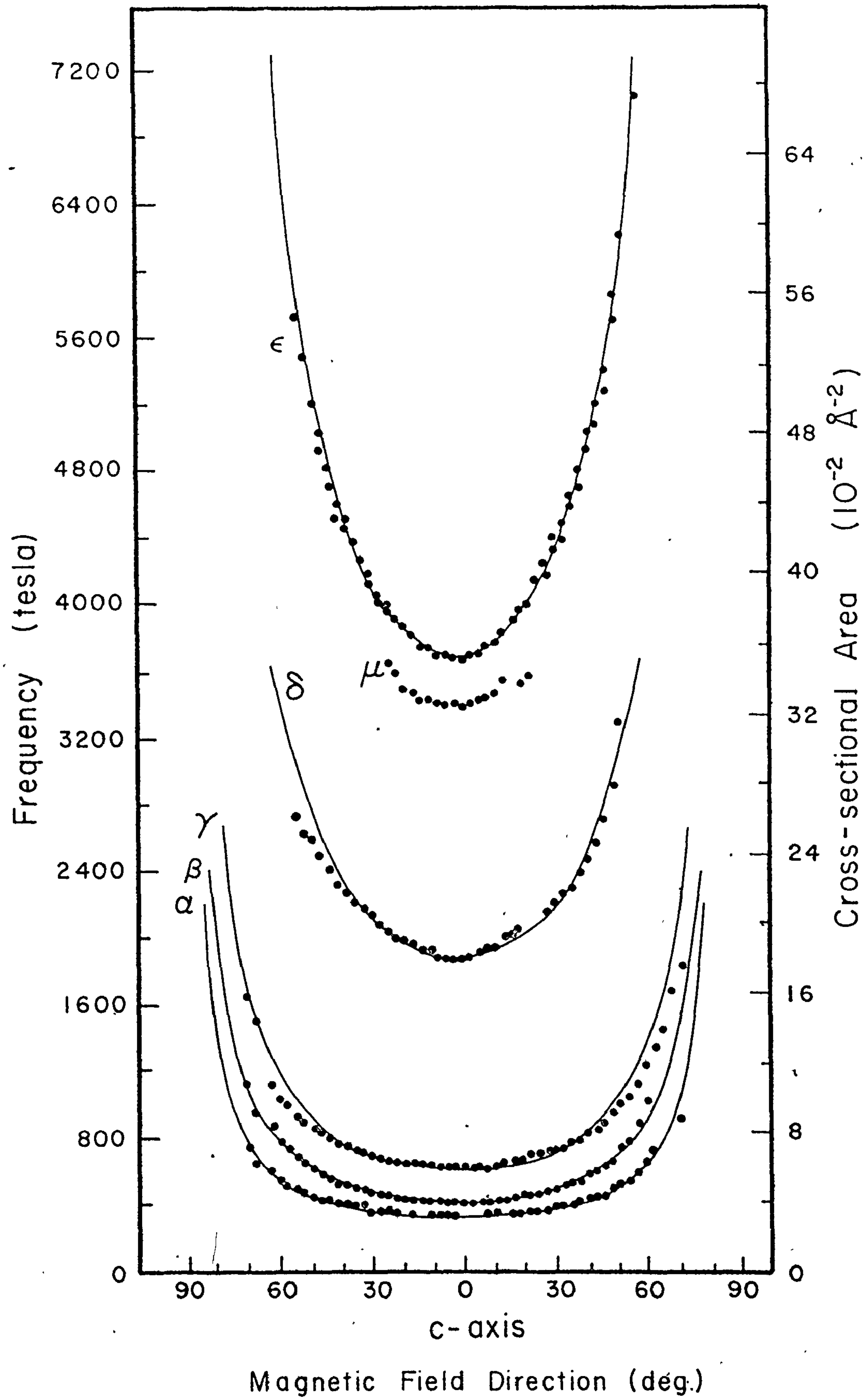
7200
6400
5600
4800
4000
3200
2400
1600
800
0
Frequency (tesla)
64
56
48
40
32
24
16
8
0
Cross-sectional Area (10^{-2} Å^{-2})
ε
μ
δ
γ
β
α
90 60 30 0 30 60 90
c-axis
Magnetic Field Direction (deg.)

Figure III.9

dHvA frequencies and corresponding cross-sectional areas as a function of magnetic field direction away from the c axis in $Hg_{3-\delta}AsF_6$. Solid lines represent cylindrical fits.

tection coil system. A toothed wheel is glued at the end of these cylinders making it possible to rotate the sample using a worm gear at the end of a rod extending to the top of the low temperature dewar in which the whole assembly sits. If the c axis is initially aligned with the axis of the detection coils, it is possible to measure dHvA frequencies for magnetic field directions in a (hk0) crystallographic plane by rotating the sample holder.

The detection coil system, composed of a pick-up coil and a modulation coil, and the electronics have been described previously by Poulsen et al (1971).

The modulation coil is used to add a small oscillating magnetic field of amplitude h and frequency ω to the large dc magnetic field H

$$H' = H + h \cos \omega t \ .$$

The oscillatory part of the magnetization in the sample becomes

$$M = M_0 \sin\left(\frac{2\pi F}{H+h\cos\omega t}\right) \qquad \text{(III.12)}$$

where F is the dHvA frequency. The pick-up coil detects changes in this magnetization which can be expanded into harmonics of ω

$$\frac{dM}{dt} = M_0 \sum_{n=1}^{\infty} 2n\omega J_n(a) \sin\left(n\omega t + \frac{n\pi}{2}\right) \sin\left(\frac{2\pi F}{H} + \frac{n\pi}{2}\right) \qquad \text{(III.13)}$$

where

$$a = \frac{2\pi F h}{H^2}$$

and $J_n(a)$ is the Bessel function of order n. A frequency of modulation of 517 Hz is used and the signal from the pick-up coil at the second harmonic of this frequency (1034 Hz) is detected.

The field from a 5.5 Tesla Westinghouse magnet is changed linearly in 1/H so that the dHvA oscillations are equally spaced in time. The signal amplitude and the magnetic field are alternatively recorded on magnetic tape and the Fourier transform is calculated on a CDC 6400 computer. Peaks in the histogram of this Fourier transform give the values of the dHvA frequencies. Data are collected at various modulation fields, h, that maximize the Bessel function for different ranges of dHvA frequencies.

2. Results

We measured the dHvA effect in four $Hg_{3-\delta}SbF_6$ samples. The graphs of frequency versus rotation angle obtained for all of them show characteristics of polycrystalline samples. Instead of a set of frequency branches with frequencies increasing or decreasing, we observe approximately the same frequencies at all angles as the sample is rotated. One of these, Sb 4, contains only one major crystal and a few separate smaller crystals.

The six fundamental frequency branches for the larger crystal in this sample are shown in Fig. III.10. The solid

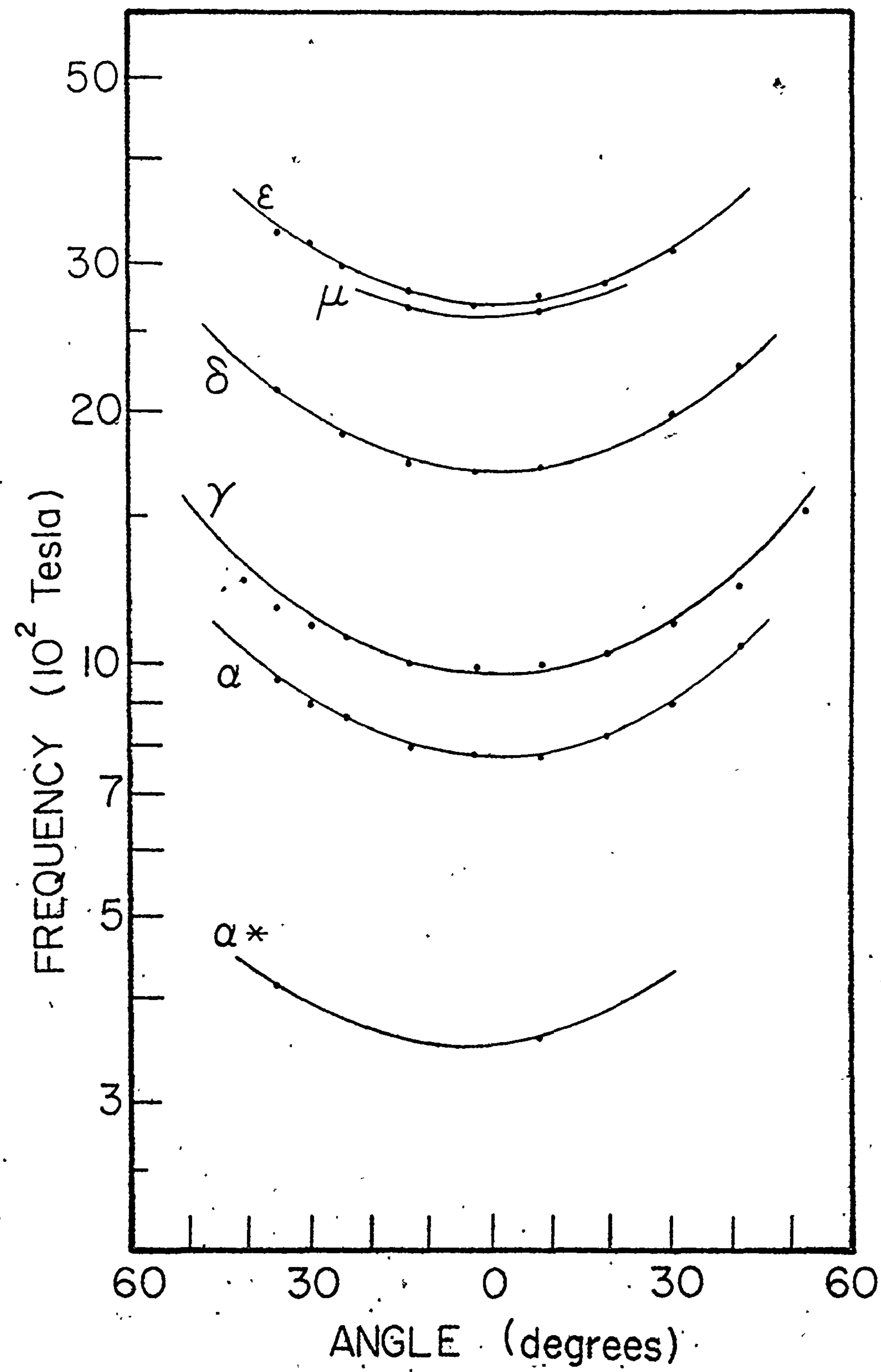

Figure III.10

Semi-log plot of the dHvA frequencies as a function of magnetic field angle from the c axis in $Hg_{3-\delta}SbF_6$. Solid lines represent cylindrical fits.

lines are fits to these frequencies assuming that the Fermi surface is cylindrical so that

$$F = F_o \sec\theta \ .$$

The agreement is very good up to 40° away from the minimum position, the largest angle at which frequencies are still detected. This implies that deviations from an exactly cylindrical Fermi surface are small. The value of the six frequencies at the minimum position, which is taken to be the $\vec{c}$ axis, are listed in Table III.3.

Also, with another polycrystalline sample of $Hg_{3-\delta}SbF_6$, Sb 1, the temperature dependence of the amplitude of the strongest frequencies for one orientation was measured. The cyclotron masses corresponding to these frequencies were calculated from the Lifschitz-Kosevitch formula (Gold, 1968).

The frequencies for which the effective masses were measured could belong to different individual crystals inside the polycrystalline sample. To compare the different effective masses, it is necessary to scale them back to a common crystal orientation. This is done by comparing the frequencies for which the cyclotron masses were measured to the minimum frequencies of the six branches that are fundamental frequencies in sample Sb 4. For a perfectly cylindrical Fermi surface, the frequencies and the effective masses both behave like sec θ as the angle between the cylinder axis and the magnetic field

Table III.3 dHvA frequencies and cyclotron masses at the minimum position and curvature factors of orbits detected in $Hg_{3-\delta}SbF_6$

Orbit	Freq. (Teslas)	m*/m	$\frac{1}{2\pi}\ \frac{\partial^2 A}{\partial k_z^2}$
α^*	345	-	-
α	770	0.15±.02	.03±.03
γ	975	-	-.06±.01
δ	1680	0.18±.03	.06±.02
μ	2580	-	-
ε	2700	0.32±.01	.01±.03

is changed. Therefore, for a given branch,

$$m^*(\theta_{min}) = \frac{F(\theta_{min})}{F(\theta)} m^*(\theta) \quad . \qquad (III.14)$$

The cyclotron masses at the minimum frequency for three fundamental frequency branches of $Hg_{3-\delta}SbF_6$ are shown in Table III.3.

The dHvA frequencies in $Hg_{3-\delta}AsF_6$ samples were also measured. Of the nine samples studied, three showed the pattern of frequencies against rotation angle characteristic of polycrystalline samples while no usable signal was detected in the others. The cyclotron masses associated with seven frequencies for one orientation of a polycrystalline crystal, As 9, were measured. Using the graph of frequencies against rotation angle obtained by Razavi et al (1979), three of these frequencies are assigned to the γ, δ and ε branches. As for $Hg_{3-\delta}SbF_6$ the cyclotron masses for the minimum frequencies of these branches can be calculated assuming a perfectly cylindrical Fermi surface. The results are presented in Table III.4

3. Discussion

The measurements of the dHvA frequencies as a function of magnetic field direction from the c axis in $Hg_{3-\delta}SbF_6$ show that the Fermi surface of this compound consists of cylinders aligned with the c axis. This is what was expected from the Fermi surface model constructed from one-dimensional free electrons. The energy of these electrons only depends on the

Table III.4 dHvA frequencies and cyclotron masses of three orbits in $Hg_{3-\delta}AsF_6$

Orbit	Frequency (T)	m*/m
γ	626	0.23±.02
δ	1860	0.27±.08
ε	3680	0.33±.01

component of the wavevector along the chain associated with these electrons. Since there are no chains along the $\vec{c}$ direction, the Fermi surface has to be independent of k_z (i.e., cylindrical).

From the ratio of the measured frequencies to the frequencies obtained from a cylindrical fit, the curvature factors, $\frac{1}{2\pi}\frac{\partial^2 A}{\partial k_z^2}$, corresponding to frequencies α, γ, δ and ε have been calculated. These dimensionless values, shown in Table III.3, are much smaller than one, the value for a spherical piece of FS, but, within experimental error, the values for the γ and δ frequencies are not equal to zero, the value for a perfectly cylindrical FS. Therefore, there is a possibility of a small undulation of the FS cylinders. This is compatible with our model. When an interaction between perpendicular chains was introduced, creating a gap at the intersection of the two flat Fermi surfaces corresponding to the two sets of mercury linear chains, it was assumed that the gap between the γ orbit and the ε orbit is small. Any variation of this gap along the k_z direction would not change the cross-sectional areas of these two orbits by a significant amount but would lead to some undulation of the two cylinders. Also the small gaps produced by translating the Fermi surface on to itself by a wavevector q, because of the incommensurability of the lattice of the mercury chains and the hexafluoride anions' lattice, could vary along the k_z direction. A calculation of the size of these gaps and how they vary with k_z could be carried out in a more complete band structure calculation (for example, using the pseudo-potential method). At the moment, there is no need to undertake this program because the values of the curvature factors are not very precise and the present model accounts very well for the minimum frequencies of all the branches observed as will be shown below for $Hg_{3-\delta}SbF_6$.

In our model, the δ orbit area depends only on the crystal lattice parameter, a. At room-temperature, Cutforth (1975) obtained a value of 7.699 Å for this parameter in $Hg_{3-\delta}SbF_6$. Assuming a contraction of 1% of the SbF_6 lattice from room-temperature to 1.25 K

$$a(1.25\ K) = 7.62\ \text{Å}\ .$$

Using

$$\text{Area}(\delta\ \text{orbit}) = \left(\frac{\pi}{a}\right)^2$$

the dHvA frequency corresponding to the δ orbit should be 1780 T. This is within 6% of the minimum value of 1680 T observed for one of the frequency branches.

The ratios of the five other major frequencies to the δ frequency are shown in Table III.5. Comparing these ratios to the theoretical ones plotted in Fig. III.8, the observed frequencies are assigned to orbits in our Fermi surface model using a value of δ of 0.135. The theoretical values of the frequency ratios, presented in Table III.5 for that value of δ, are in excellent agreement with the measured values for all

Table III.5 dHvA frequencies and their ratios to the δ frequency for $Hg_{3-\delta}SbF_6$ together with theoretical predictions obtained with a = 7.843 Å and δ = 0.135

Orbit	Experimental		Calculated	
	F (Tesla)	F/F_δ	F (Tesla)	F/F_δ
α^*	345	0.205	345	.205
α	770	0.458	773	.460
γ	975	0.580	986	.593
δ	1680	1	1680	1
μ	2580	1.538	2587	1.540
ε	2700	1.607	2710	1.613

but the γ frequency for which there is a 2% deviation.

This value of δ, 0.135, is in good agreement with the value of 0.12 derived earlier from a 1% contraction of the SbF_6 lattice. Also, it is 35% smaller than the value measured in $Hg_{3-\delta}AsF_6$ at 10 K ($\delta = 0.21$) so that values of the dHvA frequencies associated with the same orbits in both compounds (Table III.6) differ by as much as a factor of seven for the α^* orbit and as little as 10% for the δ orbit. Yet the two sets of frequencies are correctly accounted for by the same model using the two different values of the incommensurability parameter, δ.

The cyclotron masses determined for the minimum frequencies of the α, δ and ε branches for $Hg_{3-\delta}AsF_6$ are shown in Table III.7. The cyclotron masses calculated from equation (III.11) assuming a free electron dispersion relation are also shown in this table.

Although there is not good agreement between the theoretical and experimental values, the theory gives the orders of magnitude and general trends of the cyclotron masses: the cyclotron masses increase with increasing frequencies and the masses for the ε and δ frequencies are larger in the arsenic than in the antimony compound. However, for the low frequencies, α and γ, the experimental cyclotron mass is larger in the arsenic compound contrary to theory.

The differences between the experimental effective masses and the theoretical predictions could be due to deviations

Table III.6 dHvA frequencies in $Hg_{3-\delta}AsF_6$ and $Hg_{3-\delta}SbF_6$ for the same orbits

Orbit	F (Tesla)	
	$Hg_{3-\delta}AsF_6$	$Hg_{3-\delta}SbF_6$
α^*	48	345
α	340	770
γ	626	975
δ	1860	1680
μ	3413	2580
ε	3680	2700

Table III.7 Comparison between experimental and calculated cyclotron masses in $Hg_{3-\delta}AsF_6$ and $Hg_{3-\delta}SbF_6$

Orbit	$Hg_{3-\delta}AsF_6$ m^*/m_o theory	$Hg_{3-\delta}AsF_6$ m^*/m_o exp.	$Hg_{3-\delta}SbF_6$ m^*/m_o theory	$Hg_{3-\delta}SbF_6$ m^*/m_o exp.
α	.161	-	.197	.15±.02
γ	.161	.23±.02	.197	-
δ	.278	.27±.08	.269	.18±.03
μ	.395	-	.342	-
ε	.395	.33±.01	.342	.32±.01

from a free electron dispersion relation or to electron phonon interactions. Because of the large resistivity ratio between room-temperature and liquid helium temperature in these compounds, electron-phonon interaction is believed to be important.

d. de Haas-van Alphen effect under pressure

1. Introduction

The dHvA effect in samples of $Hg_{3-\delta}AsF_6$ was measured as a function of pressure up to 5 kbars. It was expected that hydrostatic pressure of 5 kbar would produce a contraction of the hexafluoride lattice of the same order as the 1% contraction observed upon cooling this compound from room-temperature to 10 K. This is the case for most other metals (Bridgman, 1931). It was also expected that the Hg-Hg distance in the chains would not be changed significantly by pressure since this distance is independent of temperature. At 1.25 K, δ would then change from 0.21 at zero pressure to 0.24 at 5 kbar, causing changes in the dHvA frequencies.

2. Experimental techniques and results

Hydrostatic pressures of up to 5 kbar were generated by a system described by Slavin and Datars (1974). The samples were placed at the bottom of Kel-F cylindrical sample holders, such that the c axis was aligned with the magnetic field and were held in place by teflon tape.

A pressure of 5 kbar was applied to the sample at room-temperature. Then, the pressure bomb was cooled down to the liquid nitrogen boiling point (77 K) and the pressure was increased back to 5 kbar. Then, liquid helium was transferred into the sample dewar so that the pressure transmitting helium would freeze from the bottom of the pressure bomb upwards. All lower pressures were obtained by heating the pressure bomb beyond the melting point of the solid helium (39 K at 5 kbar), relieving some of the pressure and cooling the pressure bomb as described above. Usually, the dHvA frequencies were measured at two or three different pressures during a day. Between experiments, the pressure bomb was sealed and maintained at 77 K.

When all the measured frequencies were plotted against pressure all the changes in frequencies took place from one day to the next while the frequencies were practically constant for all pressures applied during one day as shown in Fig. III.11 for one sample over five days. Since the same effect could be observed if the helium transmitting the pressure had remained frozen when the pressure was released, the same procedure was used in measuring the pressure dependence of the superconducting temperature of tin. The results of this experiment showed that the pressure changed as expected when more than one pressure was studied during one day. This also provided a check of the calibration of the pressure gauge. The

Figure III.11

dHvA frequencies for $Hg_{3-\delta}AsF_6$ as a function of pressure when it is lowered from 4 to 1 kbar over five days. Horizontal segments of the solid line for the δ frequency represent the average of the δ frequency for each day. Solid lines for the other frequencies are theoretical predictions from eq. (III.16a) and (III.16b).

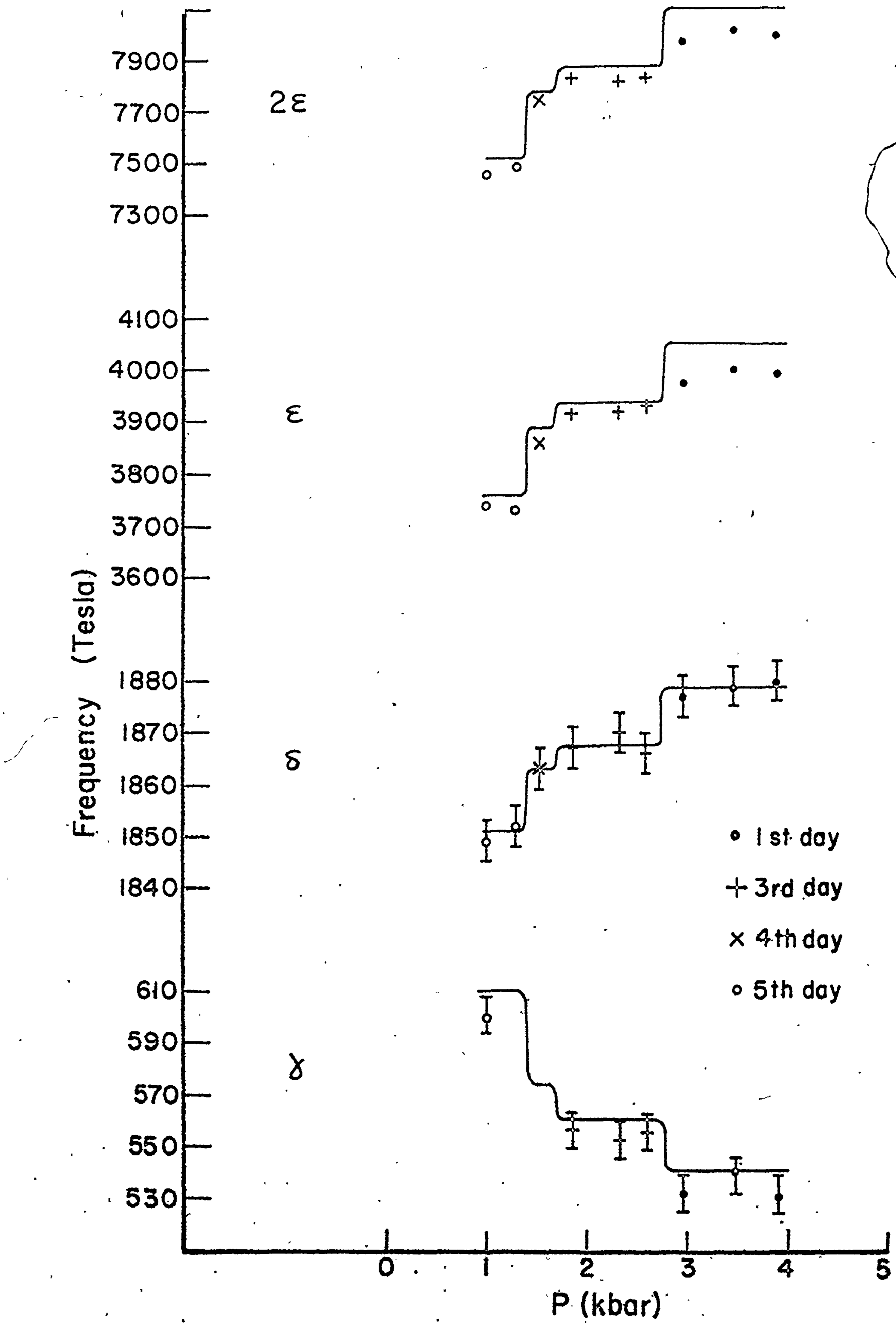

7900
7700
7500
7300
2ε
4100
4000
3900
3800
3700
3600
ε
Frequency (Tesla)
1880
1870
1860
1850
1840
δ
1st day
3rd day
4th day
5th day
610
590
570
550
530
γ
0
1
2
3
4
5
P (kbar)

lack of change in the frequencies over a period of twelve hours that was observed in $Hg_{3-\delta}AsF_6$ is an intrinsic property of this compound. Therefore, the frequency dependence is obtained by keeping the data from the first pressure of each day.

Using this criteria, the frequencies δ, γ, ε and the second harmonic of the ε frequency are plotted in Fig. III.12 for two sets of pressures on the first sample of $Hg_{3-\delta}AsF_6$. One set of data was taken going from high pressures to low pressures and then, the second set was obtained in a similar manner. Frequencies δ and ε increase and the γ frequency decreases with increasing pressure. The scatter between the two sets of experiments is much larger than the error on the individual frequencies. The solid lines in Fig. III.12 are least square fits to the data and the slopes, a, and the intercepts, b, are shown in Table III.8.

The δ frequency is only a function of the lattice parameter, a, in our model of the Fermi surface of the mercury chain compounds. Assuming that the mercury-mercury distance, d, is independent of pressure, the pressure dependence of all other frequencies can be derived from the pressure dependence of the δ frequency. Assuming that the δ frequency varies at a rate α with pressure, such that,

$$F_{\delta} = F_{\delta_o} + \alpha P \qquad \text{(III.15)}$$

where F_{δ_o} is the value of the frequency at zero pressure and

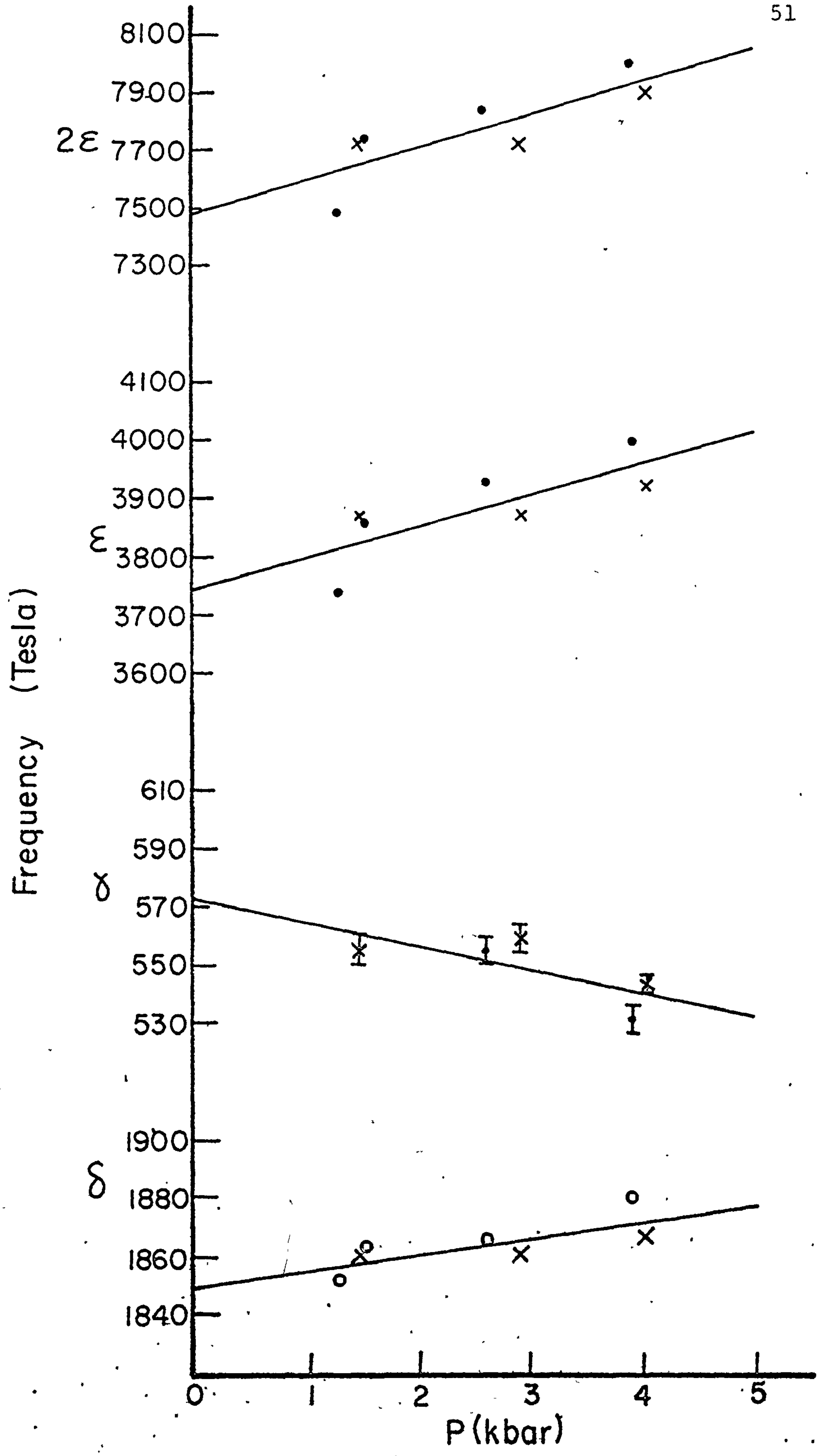

8100
7900
2ε 7700
7500
7300
4100
4000
3900
ε 3800
3700
3600
Frequency (Tesla)
610
590
γ 570
550
530
1900
δ 1880
1860
1840
0
1
2
3
4
5
P (kbar)

Figure III.12

dHvA frequencies for $Hg_{3-\delta}AsF_6$ as a function of pressure. Both the first set (points) and the second set (crosses) of data are obtained as the pressure is lowered. Solid lines are least square fits to the data.

Table III.8 Comparison of experimental and theoretical slopes and intercepts of frequencies versus pressure in $Hg_{3-\delta}AsF_6$

Orbits	Experiment			Theory	
	Slope a (Tesla/kbar)	Intercept b (Tesla)	a/a_δ	a/a_δ	Intercept b (Tesla)
γ	-8 ± 4	$(5.7\ \pm.1)\times10^2$	-2 ± 1	$-2.78\pm.03$	$(5.9\pm\ .2)\times10^2$
δ	6 ± 2	$(1.850\pm.006)\times10^3$	1	1	-
ε	$(5\pm2)\times10^1$	$(3.75\ \pm.09)\times10^3$	8 ± 6	$9.97\pm.08$	$(3.81\pm.06)\times10^3$
2ε	$(1.2\pm.4)\times10^2$	$(7.48\ \pm.09)\times10^3$	20 ± 9	$19.9\ \pm.2$	$(7.6\pm.1)\times10^3$

αP is much smaller than F_{δ_o} in the range of pressures that are applied, then

$$F_\gamma = F_{\gamma_o} - 5\alpha\sqrt{\frac{F_{\gamma_o}}{F_{\delta_o}}}\,P \qquad \text{(III.16a)}$$

$$F_{\gamma_o} = (K - 5\sqrt{F_{\delta_o}})^2$$

and

$$F_\varepsilon = F_{\varepsilon_o} + 7\alpha\sqrt{\frac{F_{\varepsilon_o}}{F_{\delta_o}}}\,P \qquad \text{(III.16b)}$$

$$F_{\varepsilon_o} = (7\sqrt{F_{\delta_o}} - K)^2$$

where

$$K^2 = \frac{2\pi\hbar}{ed^2} \; .$$

These equations state that if the δ frequency increases with pressure then the γ frequency will decrease and the ε frequency will increase. This is what is observed experimentally. Also, the rates of change with pressure of the γ and ε frequencies are related to the rate of change of the δ frequency so that the ratios of these rates only depend on the values of the corresponding frequencies at zero pressure. In Table III.8, these theoretical predictions are compared with the ratios of the slopes of the least-square fits to the experimental frequencies. Also, the frequencies at zero pressure calculated with

$$a = 7.47\ \text{Å}$$

$$d = 2.686\ \text{Å}$$

using eq. (III.16a) and (III.16b) are listed in Table III.8.

In Fig. III.11, we have taken the average value of the δ frequency over each day as a fit to that frequency and calculated the corresponding γ and ε frequencies from eq. (III.16a) and (III.16b) using the same value of d as in the above. These are the solid lines in Fig. III.11.

The theoretical predictions and experimental values in Table III.8 agree within experimental error. Also, in Fig. III.11, the theoretical values for the frequencies δ, ε and 2ε are within 1% of the experimental values and reproduce the jumps in frequency from day to day.

3. Discussion

When hydrostatic pressure is applied to $Hg_{3-\delta}AsF_6$, we expect the tetragonal lattice of negative ions to contract while the mercury-mercury distance remains the same. This implies that some mercury atoms will be leaving the chains. These mercury atoms could diffuse to special locations in the sample, i.e. grain boundaries, dislocation planes, vacancies, etc.... . This is similar to the mercury extrusion observed when the temperature is lowered through the temperature range 195-210 K at zero pressure (Datars et al, 1979). When the pressure is released, the arsenic hexafluoride lattice would remain locked to the chains as long as the extruded mercury atoms do not return to the chains. This is what we believe is happening when the measured dHvA frequencies remain the same as the pressure is released during one day of experiments. If the diffusion of the extruded mercury atoms back to the chains only becomes significant at a temperature between 40 and 70 K or if this diffusion is simply slow at all temperatures, it would explain why changes are only observed from day to day. Also, not all the atoms may return to the chains and this may account for the differences observed in the two sets of pressure measurement on the same sample.

Over the pressure range we have investigated, the δ frequency increases by 1.4% according to the fit in Fig. III.12. This implies that the lattice parameter, a, decreases by 0.7% over the same range. The theoretical predictions of the changes in all other frequencies are based on the change in the incommensurability parameter, 0.21 at 0 kbar to 0.23 at 5 kbar, caused by this change in lattice parameter if the mercury-mercury distance remains constant. The agreement between theory and experiment allows us to conclude that all changes in the dHvA frequencies are a result of a contraction of the arsenic hexafluoride lattice when pressure is applied to the sample. Also, it demonstrates that our Fermi surface model works for discrete values of δ in $Hg_{3-\delta}AsF_6$ and $Hg_{3-\delta}SbF_6$ at room-pressure as well as for a range of values of δ in $Hg_{3-\delta}AsF_6$ under pressure.

CHAPTER IV

RESISTIVITY

a) Introduction

Electrical resistivity measurements by Cutforth et al (1977) on unoriented samples of $Hg_{3-\delta}SbF_6$ and $Hg_{3-\delta}AsF_6$ showed that the resistivity of these compounds is approximately 125 $\mu\Omega$-cm at room-temperature and that it decreases by a factor of 150 for $Hg_{3-\delta}SbF_6$ and 10^3 for $Hg_{3-\delta}AsF_6$ between room temperature and 4.2 K. In further measurements with oriented crystals, they found that the ratio of the resistivity along the c axis to that along the a or b axis at room temperature is 40 for $Hg_{3-\delta}SbF_6$ and 100 for $Hg_{3-\delta}AsF_6$ and that the resistivity is isotropic in the ab plane. They noted that the resistivity does not exhibit any sign of residual resistivity down to liquid helium temperature in all the samples they investigated. Finally, they observed significant variations in the resistivity between 200 and 235 K which they interpreted as evidence for a phase transition in that region.

Resistivity measurements on $Hg_{3-\delta}AsF_6$ by Chiang et al (1977) confirmed the previous results and indicated that the resistivity for directions in the ab plane follows a $T^{1.5}$ law down to 1.4 K. Chiang et al also reported that the resistivity along the c axis decreases by three orders of magnitude within 0.2 K of 4 K making $Hg_{3-\delta}AsF_6$ an anisotropic superconductor. This will be further discussed in Chapter V.

Chakraborty _et al_ (1978), using a contactless ac mutual inductance technique, concluded that below 30 K the temperature dependence of the resistivity in the ab plane is more accurately described by a T^2 law but in a later paper (Chakraborty _et al_, 1979), stated that in the same temperature range, a four-probe dc measurement gave a T^3 law.

Therefore, there is experimental uncertainty about the temperature dependence of the resistivity in the ab plane at low temperatures. Using a model in which resistivity is caused by a diffusion of the electrons along flat planes of a square Fermi surface, Kaveh and Ehrenfreund (1979) predicted that the resistivity at low temperature should vary as T^3. However, the Fermi surface dimensions used in the calculation were about three times larger than the ones obtained from dHvA experiments by Razavi _et al_ (1979) and their argument that large angle scattering freezes out exponentially below 30 K is not justified.

We will present a model for the resistivity of the linear chain compounds that utilizes the measured phonon dispersion and Fermi surface parameters. Our measurements of the resistivity by the Montgomery method will be compared to this theory.

b) Theory

1. Resistivity in the ab plane

By equating the entropy production associated with the Joule heating caused by the macroscopic currents to the entropy production due to scattering of the electrons, the following formula for the lattice resistivity is obtained (Ziman, 1960)

$$\rho_L = \frac{1}{k_B T} \frac{\iiint \{\phi_{\vec{k}} - \phi_{\vec{k}'}\}^2 P_{\vec{k},\vec{q}}^{\vec{k}'} d\vec{k}\, d\vec{k}'\, d\vec{q}}{\left| \iint e\vec{v}_{\vec{k}}\, \phi_{\vec{k}} \frac{\partial f_{\vec{k}}^0}{\partial \varepsilon_{\vec{k}}} d\vec{k} \right|^2} \tag{IV-1}$$

where $f_{\vec{k}}(\vec{r})$ is a distribution function which measures the number of carriers in the $\vec{k}$th state in the neighbourhood of $\vec{r}$. $f_{\vec{k}}^0$ is that distribution without any field applied. $\phi_{\vec{k}}$ is defined by

$$f_{\vec{k}} \equiv f_{\vec{k}}^0 - \phi_{\vec{k}} \frac{\partial f_{\vec{k}}^0}{\partial \varepsilon_{\vec{k}}} \tag{IV-2}$$

and is a measure of the deviation from equilibrium in the electron distribution, weighted with a factor which depends on the form of that distribution.

$v_{\vec{k}}$ is the velocity of the electron in the $\vec{k}$th state given by

$$\vec{v}_{\vec{k}} = \frac{1}{\hbar} \vec{\nabla}_{\vec{k}} \varepsilon_{\vec{k}} \tag{IV-3}$$

where $\varepsilon_{\vec{k}}$ is the energy of an electron in the $\vec{k}$th state.

$P_{\vec{k},\vec{q}}^{\vec{k}'}$ is the equilibrium transition rate between state $\vec{k}$

and state $\vec{k}'$ when the scattering between these two states is caused by a phonon of wavevector $\vec{q}$. Perturbation theory for the electron-phonon interaction tells us that the transition probability is given by

$$P^{\vec{k}'}_{\vec{k},\vec{q}} = \left(\frac{\pi}{mN\omega}\right) \delta_{\vec{g},\vec{k}'-\vec{k}-\vec{q}} \left| J_{\vec{q},p}(\vec{k},\vec{k}') \right|^2$$

$$\mathcal{O}(\varepsilon_{\vec{k}}+\hbar\omega-\varepsilon_{\vec{k}'})\, n^0_{\vec{q}} f^0_{\vec{k}} (1-f^0_{\vec{k}'}) \qquad \text{(IV-4)}$$

where m, N and ω are respectively the mass of the ions, the number of unit cells per unit volume and the frequency of the phonon. The δ and $\mathcal{O}$ functions insure the conservation of crystal momentum ($\vec{g}$ is a reciprocal lattice vector) and energy respectively. $n^0_{\vec{q}}$ is the Bose-Einstein distribution of phonon given by

$$n^0_{\vec{q}} = \frac{1}{(e^{\hbar\omega/kT}-1)} \qquad \text{(IV-5)}$$

$J_{\vec{q},p}(\vec{k},\vec{k}')$ is the matrix element between state $\vec{k}$ and $\vec{k}'$ of the change in crystal potential caused by the displacement of the ions from their equilibrium positions. For longitudinal phonons, it can be written in the form

$$J_{\vec{q},p}(\vec{k}',\vec{k}) = C(K)\vec{K}\cdot\vec{e}_{\vec{q},p} \qquad \text{(IV-6)}$$

where $\vec{e}_{\vec{q},p}$ is the polarization vector of the phonon and $\vec{K}$, the scattering vector, is given by

$$\vec{K} = \vec{k}-\vec{k}' \; . \qquad \text{(IV-7)}$$

Substituting eqs. (IV-5) and (IV-6) in the expression for the transition probability (eq. (IV-4)) and using the Fermi-Dirac distribution for the electrons, the expression for the lattice resistivity (eq. (IV-1)) becomes, after some integration,

$$\rho_L = \frac{1}{32\pi^5 \hbar m N k_B T |\vec{J}|^2} \iint \frac{(\phi_{\vec{k}} - \phi_{\vec{k}'})^2 (\vec{K}\cdot\vec{e})^2 C^2(K)}{(1-e^{-\hbar\omega/kT})(e^{\hbar\omega/kT}-1)} \frac{d\sigma}{v} \frac{d\sigma'}{v'} \qquad \text{(IV-8)}$$

and the current is given by

$$\vec{J} = \frac{1}{4\pi^3\hbar} \int e\vec{v}_{\vec{k}} \phi_{\vec{k}} \frac{d\sigma}{v_{\vec{k}}} \qquad \text{(IV-9)}$$

where $d\sigma$, $d\sigma'$ are elements of the Fermi surfaces on which $\vec{k}$ and $\vec{k}'$ are located, respectively. To calculate the resistivity, we then look for a trial function, $\phi_{\vec{k}}$, for the Fermi surface (FS) of the mercury linear chain compounds shown in Fig. IV.1. When an electric field is applied in the x direction, the whole FS is displaced by a small amount in the k_x directio n. This displacement does not alter the current associated with the FS planes perpendicular to k_y since the velocity on these planes is perpendicular to the direction of the field. $\phi_{\vec{k}}$ can then be of the form

$$\phi_{\vec{k}} = \alpha\ \vec{v}_{\vec{k}}\cdot\vec{\mu} \qquad \text{(IV-10)}$$

where $\vec{\mu}$ is a unit vector in the direction of the field. In this trial function, the scattering time has been assumed to be a constant over the whole FS and any explicit energy dependence has been neglected (Jumper and Lawrence, 1977). The constant α can be ignored since $\phi_{\vec{k}}$ appears in both the numerator and the denominator of (IV-8). Thus for flat Fermi surface sheets

Figure IV.1

Electron-phonon scattering processes on the one-dimensional Fermi surface of the mercury chain compounds. An electron in the kth state is scattered to $\vec{k}'_{I}$, $\vec{k}'_{II}$ and $\vec{k}'_{III}$ by the phonons $\vec{q}_{I}$, $\vec{q}_{II}$ and $\vec{q}_{III}$ respectively. The electron velocity $\vec{v}_F$ is indicated by an arrow on each Fermi surface plane.

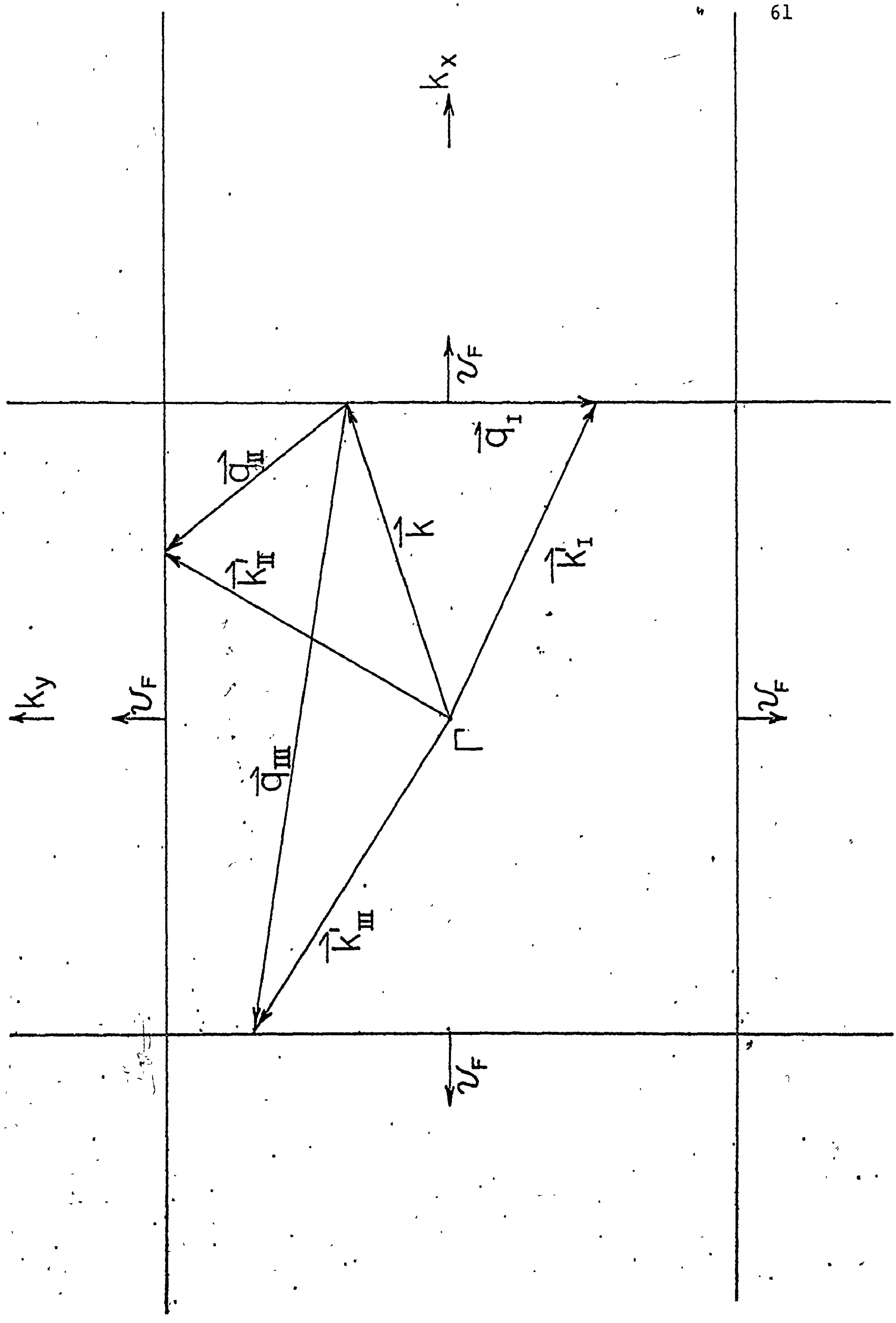

k_x
k_y
v_F
$\vec{q}_I$
$\vec{q}_{II}$
$\vec{q}_{III}$
$\vec{k}$
$\vec{k}'_I$
$\vec{k}'_{II}$
$\vec{k}'_{III}$
Γ

$$\phi_{\vec{k}} = \begin{cases} \pm v_F & \text{FS planes at } \pm k_F\hat{x} \\ 0 & \text{FS planes at } \pm k_F\hat{y} \end{cases}$$

We choose to do our calculation using the simple tetragonal Brillouin zone rather than the body-centred tetragonal because of the extra symmetry of the one-dimensional bands. Then, the total current is given by

$$\vec{J} = \frac{ev_F S}{2\pi^3\hbar}\hat{x} \qquad \text{(IV-11)}$$

where S is the area of the plane of the FS perpendicular to k_x within the Brillouin zone.

To calculate the double integral in (IV-8) we have to examine effective scattering processes. Scattering from k to k' on the same plane surface (process I in Fig. IV.1) will not change ϕ_k so that

$$(\phi_k-\phi_{k'})^2 = 0 \ .$$

Scattering from one plane surface to a surface perpendicular to it (process II in Fig. IV.1) will give rise to a resistivity labeled $\rho_{\perp}$ and has

$$(\phi_k-\phi_{k'})^2 = v_F^{\,2} \ .$$

Finally, scattering between plane surfaces at $+k_F$ and $-k_F$ along the x direction (process III in Fig. IV.1) will give rise to $\rho_{||}$ with

$$(\phi_k-\phi_{k'})^2 = 4v_F^{\,2} \ .$$

In the extended zone scheme, these scattering processes would be Umklapp processes but in the reduced zone scheme that we are using, they become normal scattering processes in the third Brillouin zone.

In the linear mercury chain compounds, phonons from the three-dimensional host lattice of octahedral anions and the one-dimensional mercury chains take part in this scattering of the electrons. The longitudinal accoustic dispersion relation of the former is given by

$$\omega = S_{3D}q \tag{IV-12a}$$

for small values of q, where S_{3D}, the speed of sound, is approximately isotropic in these compounds. The dispersion relation of the latter is

$$\omega = S_{1D}q_i \tag{IV-12b}$$

where q_i is the phonon wavevector along the ith chain. From eq. (IV-8), it follows that $\rho_\perp$ and $\rho_{||}$ caused by one-dimensional or three-dimensional phonons are given by

$$\rho_\perp^{1D} = 8\pi^2\rho_{\theta_\perp}^{1D}\,\frac{q_{\mathcal{D}}^{1D}}{Sc}\,\left(\frac{T}{\theta^{1D}}\right)^2 J_2\left(\frac{\theta^{1D}}{T}\right) \tag{IV-13a}$$

$$\rho_\perp^{3D} = 16\pi^3\rho_{\theta_\perp}^{3D}\,\frac{(q_{\mathcal{D}}^{3D})^3}{S^2c}\,\left(\frac{T}{\theta^{3D}}\right)^3 \left[J_3\left(\frac{\theta^{3D}}{T}\right) - \int_0^1 J_3\left(\frac{y\theta^{3D}}{T}\right)dy\right] \tag{IV-13b}$$

$$\rho_{||}^{1D} = 4\pi\rho_{\theta_{||}}^{1D}\,\left(\frac{k_F}{q_{\mathcal{D}}^{1D}}\right)^2 \left(\frac{\theta^{1D}}{T}\right)\,\frac{e^{2k_F\theta^{1D}/q_{\mathcal{D}}^{1D}T}}{\left[e^{2k_F\theta^{1D}/q_{\mathcal{D}}^{1D}T}-1\right]^2} \tag{IV-13c}$$

$$\rho_{||}^{3D} = 2\pi^2 \rho_{\theta_{||}}^{3D} \frac{(q_D^{3D})^2}{S} \left(\frac{T}{\theta^{3D}}\right)^3 \left[J_3\left(\frac{\theta^{3D}}{T}\right) - J_3\left(\frac{2k_F\theta^{3D}}{q_D^{3D}T}\right)\right] \qquad \text{(IV-13d)}$$

where q_D^{1D}, θ^{1D}, q_D^{3D}, θ^{3D} are the Debye wavevectors and temperatures for the one-dimensional and three-dimensional phonons respectively. ρ_θ is a constant given by

$$\rho_\theta = \frac{\hbar C^2(0) q_D^2}{mNe^2 v_F^2 k_B \theta} \quad . \qquad \text{(IV-14)}$$

where $C^2(k)$ was approximated as $C^2(0)$ following the deformation potential approximation which is a long wavelength approximation that neglects Umklapp processes (Ziman, 1960).

$J_n(x)$ are Debye integrals defined by

$$J_n(x) \equiv \int_0^x \frac{z^n e^z}{(e^z-1)^2}\, dz.$$

From the measurement of the phonon dispersion for 1D and 3D phonons in $Hg_{3-\delta}AsF_6$ by Heilman et al (1979), we calculate that

$$q_D^{1D} = \frac{\pi}{d} = 1.19 \text{ Å}^{-1}$$

$$\theta^{1D} = 400 \text{ K}$$

$$q_D^{3D} = 0.55 \text{ Å}^{-1}$$

$$\theta^{3D} = 80 \text{ K} .$$

If we assume that $C^2(0)$ is the same for 1D and 3D phonons as well as for perpendicular scattering and back-scattering, ρ_θ^{1D} is approximately equal to ρ_θ^{3D} and they can be replaced by a single quantity, ρ_θ. The temperature dependence of the four resistivities normalized by ρ_θ are shown between 0 and 300 K on Fig. IV.2. The four resistivities are of the same order of magnitude above 15 K and are linear between 50 and 300 K with extrapolated intercepts on the temperature axis at 30 K for $\rho_\perp^{1D}$ and between 10 and 15 K for the other three. Below 10 K, $\rho_\perp^{1D}$ follows a T^2 temperature dependence while the other resistivities are decreasing more rapidly. Therefore, the total resistivity becomes proportional to T^2 below 2 K as shown in Fig. IV.3.

In general, $C^2(0)$ will be different for different types of scattering and of phonons. The resistivity can then be written

$$\frac{\rho(T)}{\rho(T_0)} = \frac{\rho_0}{\rho(T_0)} + \alpha\left[\frac{\rho_\perp^{1D}(T)}{\rho_\perp^{1D}(T_0)}\right] + \beta\left[\frac{\rho_\perp^{3D}(T)}{\rho_\perp^{3D}(T_0)}\right] + \gamma\left[\frac{\rho_{||}^{1D}(T)}{\rho_{||}^{1D}(T_0)}\right] + \varepsilon\left[\frac{\rho_{||}^{3D}(T)}{\rho_{||}^{3D}(T_0)}\right] \quad \text{(IV-15)}$$

where ρ_0, the residual resistivity, α, β, γ and ε are temperature independent parameters. Since the four resistivities are linear above 50 K, the total resistivity will be linear in that range for all values of these parameters. Also, at very low temperatures, the rapidly decreasing factors in all lattice resistivities, except $\rho_\perp^{1D}$, will nullify their contributions and the total resistivity will be proportional to T^2 if the lattice resistivity does not become smaller than the residual resistivity.

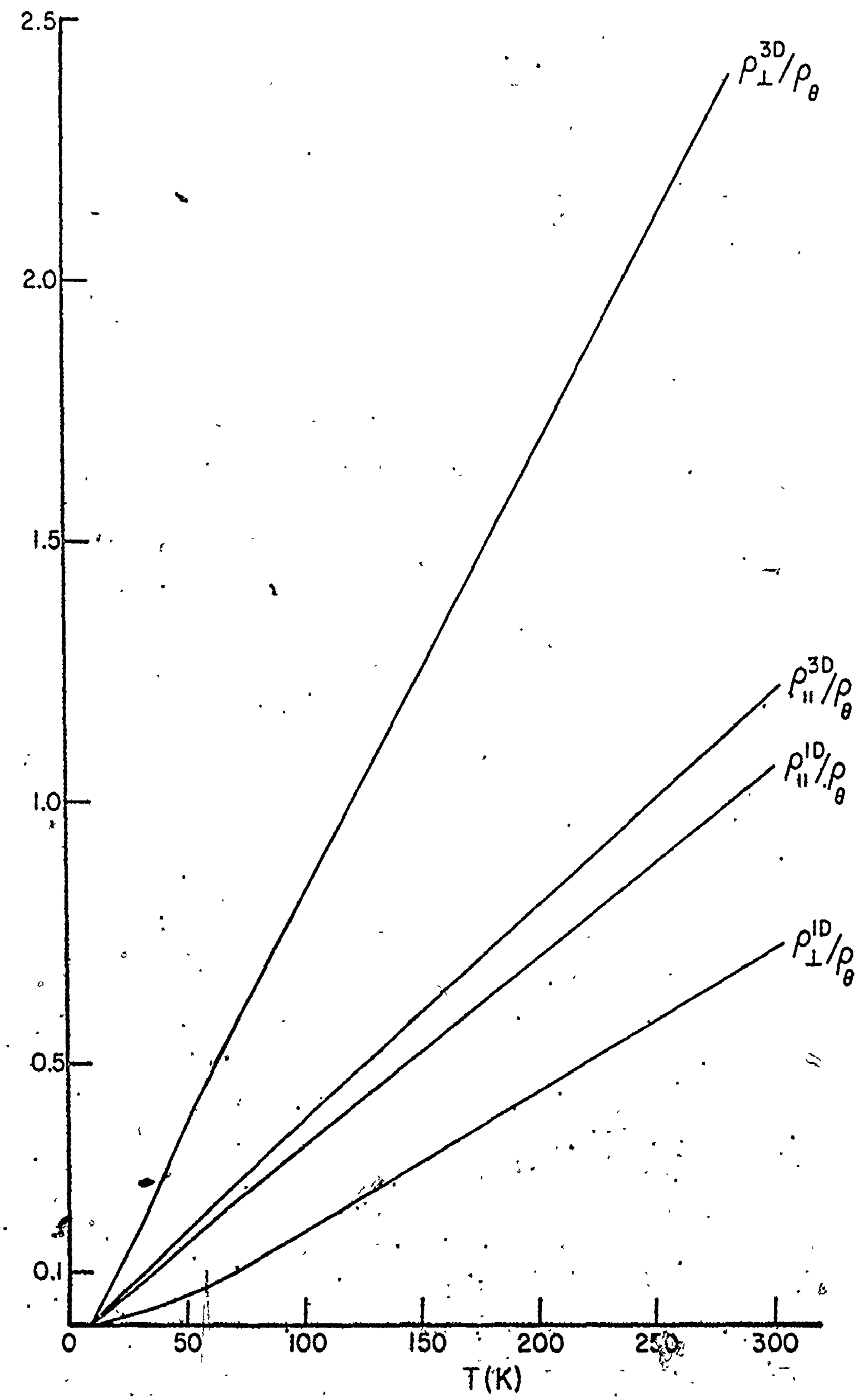

Figure IV.2

No.

$\rho_\perp^{3D}/\rho$

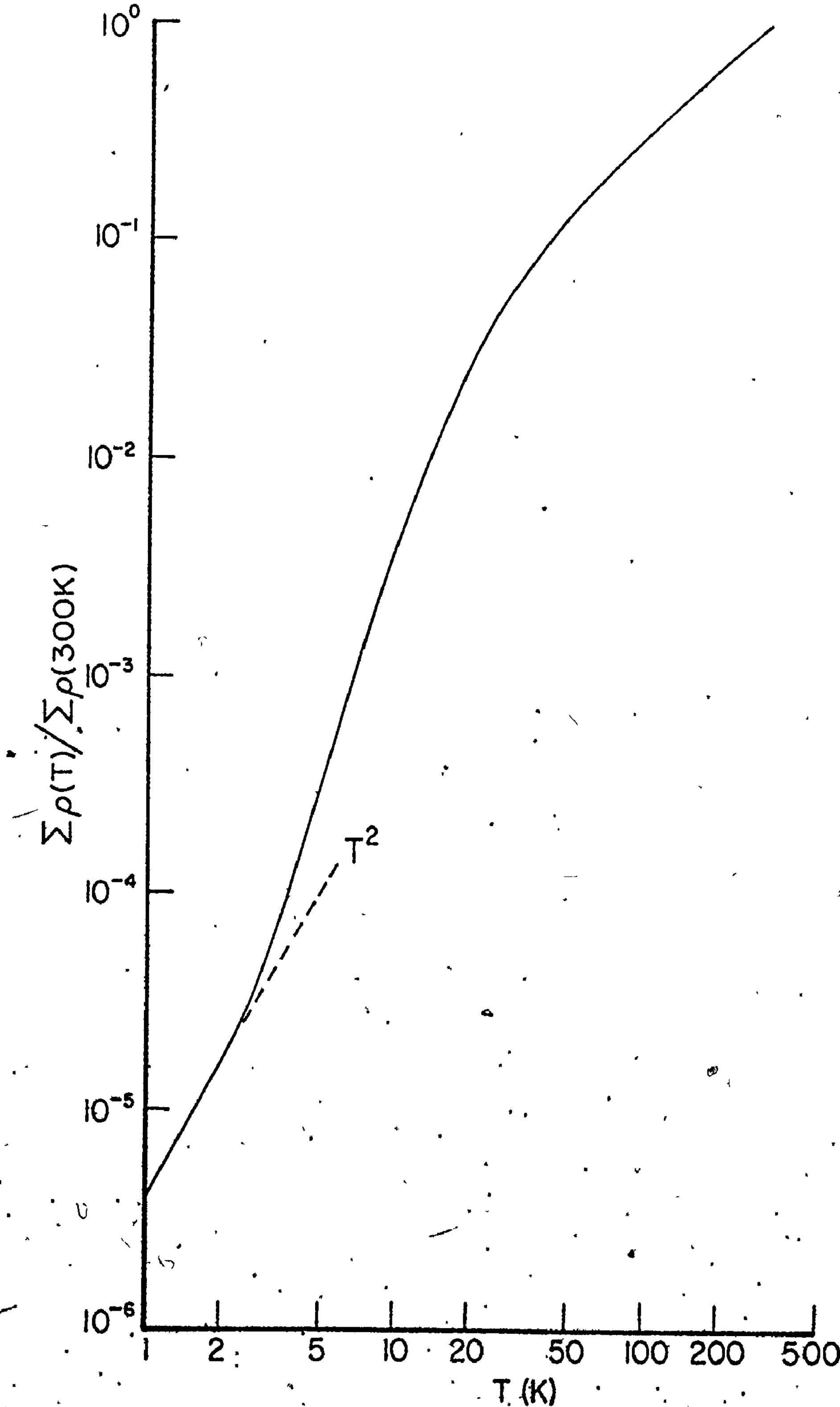

Figure IV.3

L[illegible] plot of [illegible] la[illegible]

2. Resistivity along the $\vec{c}$ axis

The electron velocity along the c direction is zero for plane Fermi surfaces at $\pm k_F$ along k_x and k_y. The resistivity along the c axis is undefined because both the numerator and the denominator of equation (IV-8) are zero. However, there can be some small undulation of the FS along k_z caused by interaction of the mercury chains separated by $\frac{c}{4}$. The first term in the energy producing such an undulation is of the form

$$\varepsilon(\vec{k}) = \varepsilon(k_x, k_y) + \delta\varepsilon \cos\left(\frac{k_z c}{4}\right) . \qquad \text{(IV-16)}$$

The component of the electron velocity along the k_z axis is then given by (Fig. IV.4)

$$\vec{v}_{\vec{k}} \cdot \hat{z} = -\frac{\delta\varepsilon}{\hbar} \cdot \frac{c}{4} \cdot \sin\left(\frac{k_z c}{4}\right) .$$

So, the trial function $\phi_{\vec{k}}$ is chosen to be

$$\phi_{\vec{k}} = \sin\left(\frac{k_z c}{4}\right) . \qquad \text{(IV-17)}$$

Scattering which will change the value of the z-component of the wavevector will produce a non-zero change in $\phi_{\vec{k}}$. The scattering from $\vec{k}$ to $\vec{k}'$ on the same plane surface by 1D phonons is the most important process. The undulation of the FS has been assigned an upper limit of 0.5 percent of k_F from measurement of the dHvA effect. This corresponds to a one-dimensional phonon of energy 0.014 meV or a temperature of 0.2 K, so the exponential factors containing the phonon frequency in eq. (IV-8) can be

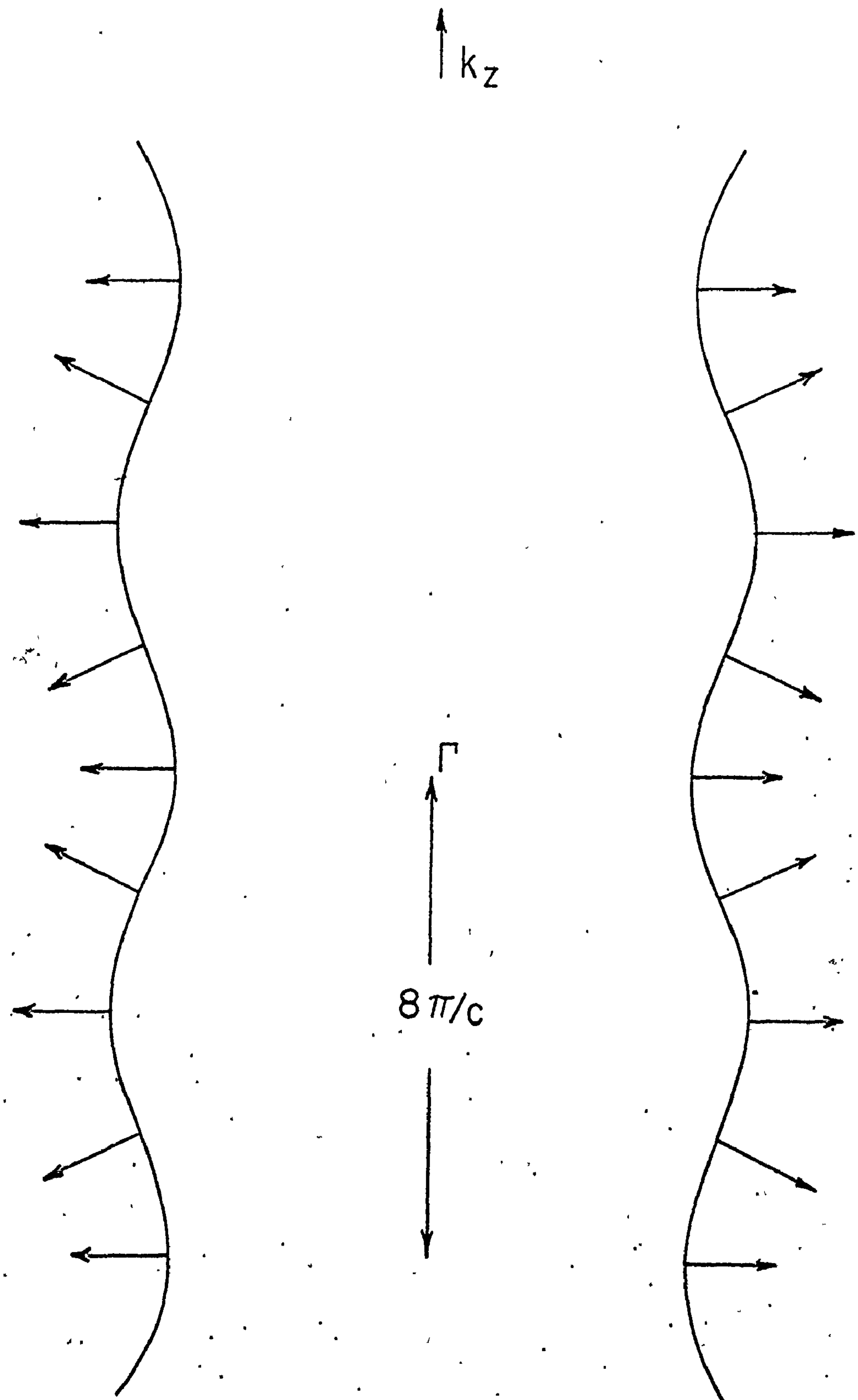

Figure IV.4

Fermi surface undulating along the k_z direction. Arrows represent the velocity of the electrons at various points expanded for all temperatures greater than 1 K. This gives

$$\rho_{c_L} = 128\pi\ \rho_\theta^{1D} \left(\frac{1}{k_F c}\right)^2 \left(\frac{\varepsilon_F}{\delta\varepsilon}\right)^2 \left(\frac{T}{\theta}\right) . \qquad \text{(IV-18)}$$

Then using the numerical values of $k_F, q_{\mathcal{D}}$ and c, the ratio of ρ_{c_L} to $\rho_\perp^{1D}$, one of the four resistivities for current along the a direction, is

$$\frac{\rho_{c_L}}{\rho_\perp^{1D}} = 0.16\left(\frac{\varepsilon_F}{\delta\varepsilon}\right)^2 \left(\frac{\theta}{T}\right) [J_2(\frac{\theta}{T})]^{-1} . \qquad \text{(IV-19)}$$

This ratio is a monotonically increasing function of decreasing temperature with the following limiting behaviours,

$$\frac{\rho_c}{\rho_\perp^{1D}} = \begin{cases} 4.9\times10^{-2}\left(\frac{\varepsilon_F}{\delta\varepsilon}\right)^2 \frac{\theta}{T} & \text{for } T \ll \theta \\ 8.0\times10^{-2}\left(\frac{\varepsilon_F}{\delta\varepsilon}\right)^2 & \text{for } T \gg \theta . \end{cases}$$

At low temperatures, the resistivity in the a (or b) direction will be dominated by a residual resistivity

$$\rho_a = \rho_0$$

while ρ_c, being much larger than ρ_a will not yet be comparable to ρ_0, giving

$$\frac{\rho_c}{\rho_a} = \frac{128\pi\ \rho_\theta^{1D}}{\rho_0} \left(\frac{1}{k_F c}\right)^2 \left(\frac{\varepsilon_F}{\delta\varepsilon}\right)^2 \left(\frac{T}{\theta}\right) .$$

The anisotropy will then be linearly decreasing with decreasing temperature. Fig. IV.5 shows a plot of the temperature dependence of the ratio of the resistivity along the c axis to the sum of the residual resistivity and the total lattice resistivity in the ab plane, shown in Fig. IV.3, using

$$\left(\frac{\varepsilon_F}{\delta\varepsilon}\right)^2 = 5000$$

and assuming that the residual resistivity equals the lattice resistivity at 20 K.

With these parameters, the theoretical anisotropy is constant and equal to 105 between 300 K and 60 K, rises below 60 K reaching a maximum of 125 at 15 K after which it decreases linearly and should become unity when both ρ_c and ρ_a are dominated by the residual resistivity.

c. Montgomery Method

Montgomery (1971) proposed a method of measuring the resistivity of anisotropic conductors based on the theoretical calculation of Logan *et al* (1971).

Samples are cut in the shape of parallelepiped of sides ℓ_1', ℓ_2', ℓ_3' with edges along the principal directions of the crystal. On one of the sample's face, the voltage, V_1, is measured across two adjacent corners while current, I_1, is passed between the two remaining corners. Then, the voltage and current probe are rotated by 90° as shown in Fig. IV.6 and the measurement described above is repeated. From these two measure-

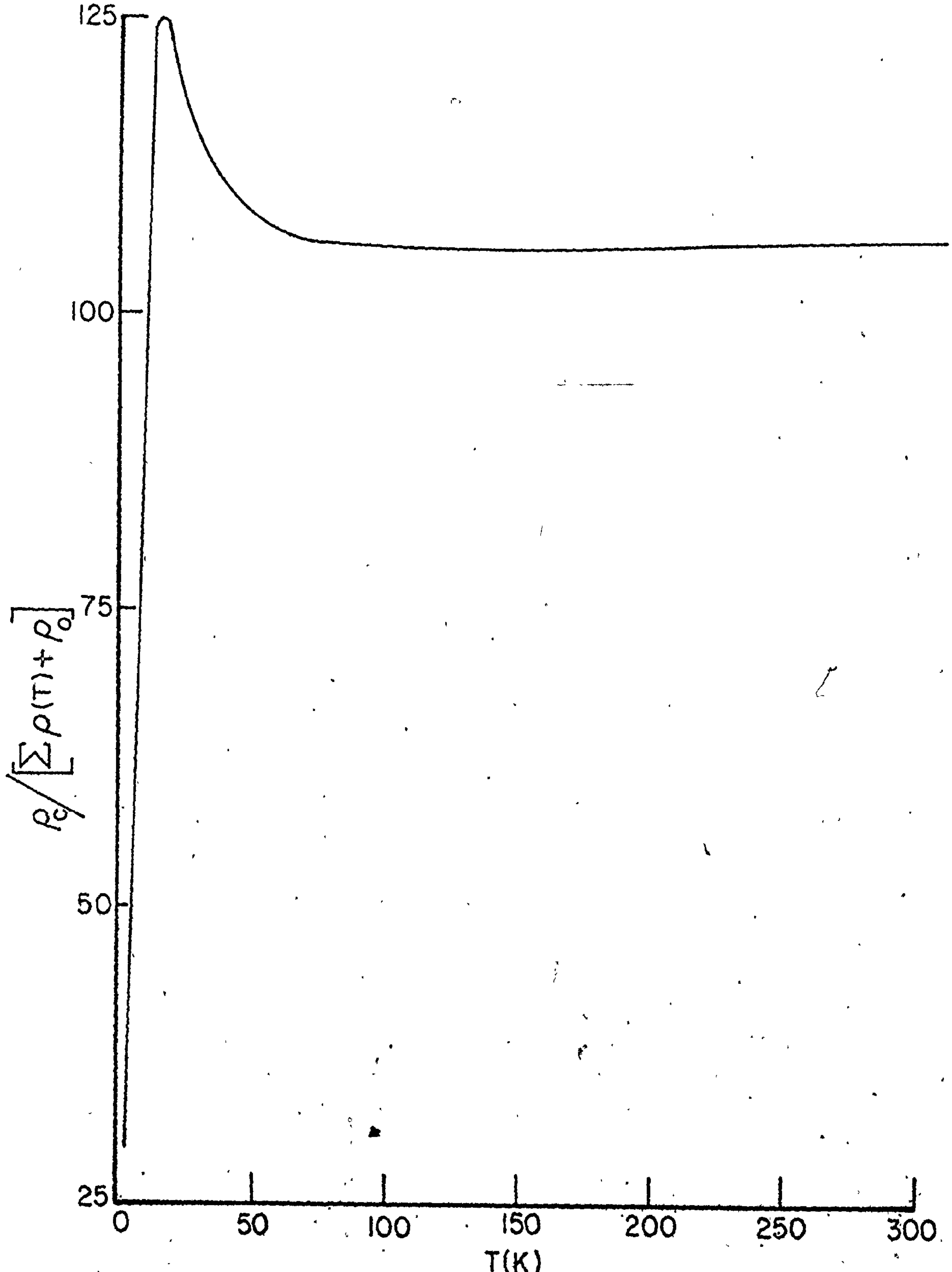

Figure IV.5

Theoretical resistivity anisotropy as a function of temperature.

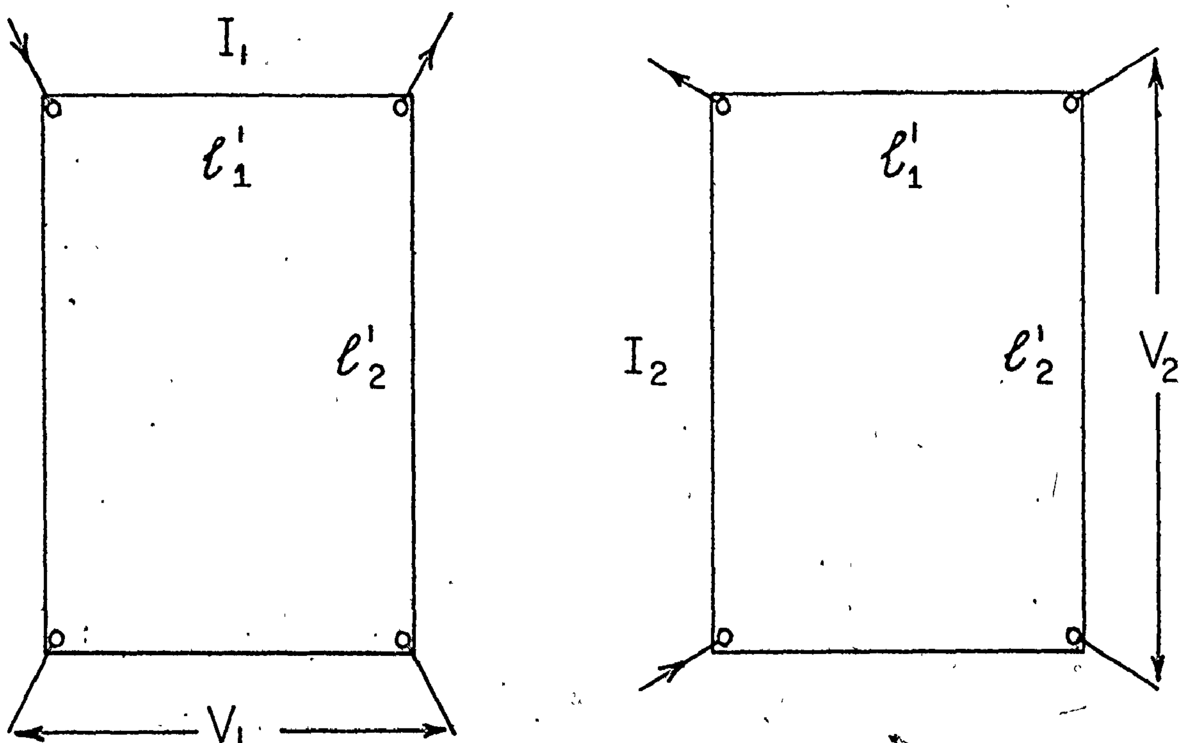

Figure IV.6

Schematic view of measurements of R_1 and R_2 on a parallelepiped sample in the Montgomery configuration.

ments, we define

$$R_1 = V_1/I_1$$
$$R_2 = V_2/I_2 \ . \qquad \text{(IV-20)}$$

For an isotropic sample Logan et al transformed the problem of one current source and one current sink in the arrangement above to an infinite array of sources and sinks in an infinite medium using the method of images. They replaced these sources and sinks by positive and negative charges because of the analogy between current flow lines and electric force lines, and they calculated the potential difference created by this infinite array at the opposite corners of the parallelepiped's face.

They obtained the following relation for the resistivity, ρ, of the isotropic sample

$$\rho = HER_1 \qquad \text{(IV-21)}$$

where E is an effective sample thickness which is equal to the sample thickness ℓ_3 when it is much smaller than the geometrical average of the two other dimensions of the sample, $(\ell_1\ell_2)^{1/2}$. H is a function of the ratio ℓ_2/ℓ_1 shown in Fig. IV.7.

Montgomery started with the results of Logan et al and used a transformation of coordinates given by Wasscher (1961) that connects an anisotropic sample with dimension ℓ_1', ℓ_2', ℓ_3' in the direction corresponding to ρ_1, ρ_2, ρ_3, the diagonal

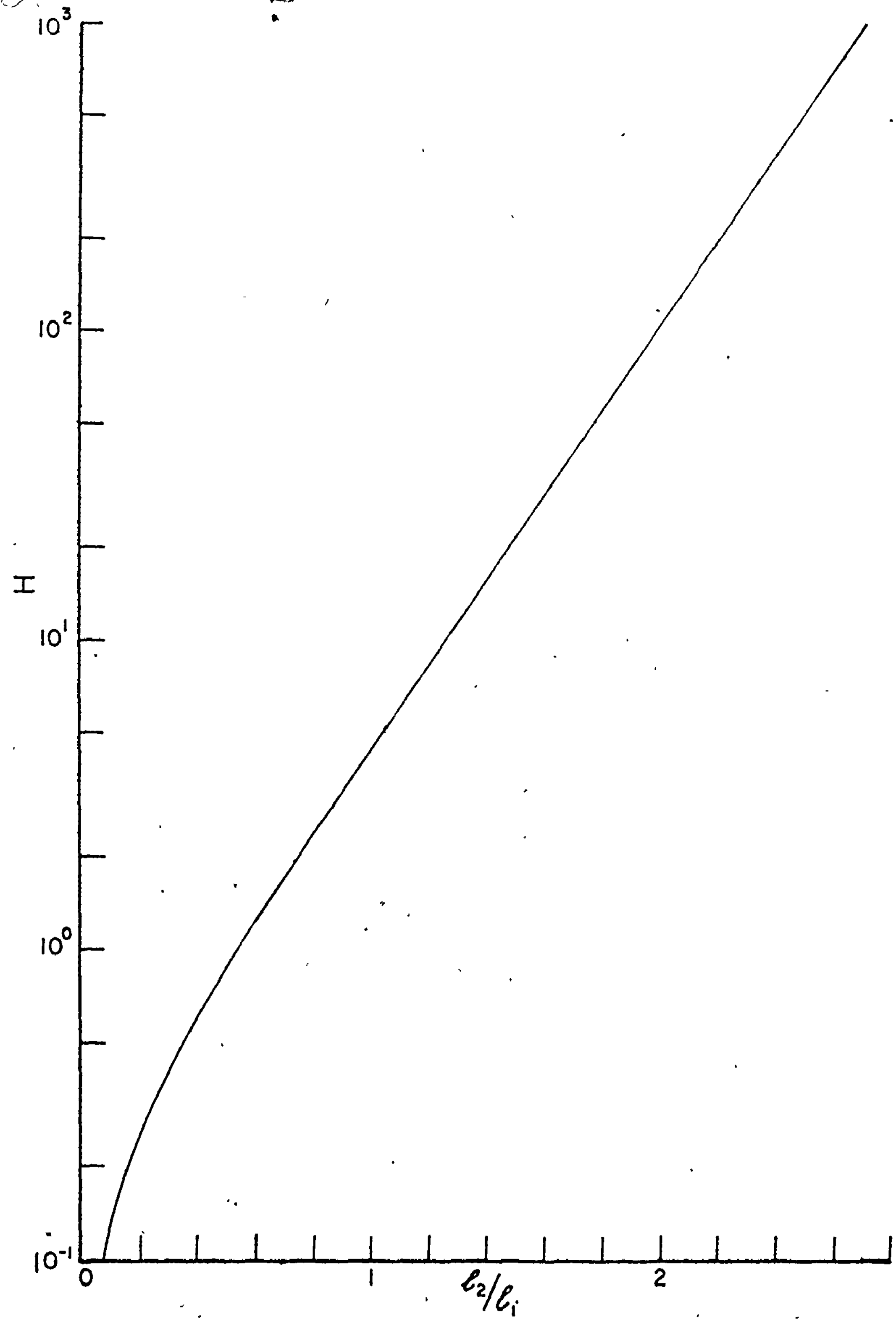

Figure IV.7

Semi-log plot of H versus the ratio of sample dimensions, ℓ_2/ℓ_1.

elements of the resistivity tensor, to an isotropic sample of dimensions ℓ_1, ℓ_2, ℓ_3 and resistivity ρ, where

$$\ell_i = \ell_i' \, (\rho_i/\rho)^{1/2} \tag{IV-22}$$

$$\rho = (\rho_1\rho_2\rho_3)^{1/3} \, . \tag{IV-23}$$

This transformation is such that if a given current is put through two points on the anisotropic sample and the corresponding points on the isotropic sample, then the same potential difference exists across pairs of points connected by the transformation. Therefore, the ratio R_2/R_1 is the same for the anisotropic sample and its isotropic equivalent. It is a very sensitive function of ℓ_2/ℓ_1 (Fig. IV.8) so that measuring this ratio allows us to calculate

$$(\rho_2/\rho_1)^{1/2} = \frac{\ell_2}{\ell_1} \times \frac{\ell_1'}{\ell_2'} \, . \tag{IV-24}$$

For the isotropic equivalent

$$\rho = H(\ell_2/\ell_1)\,\ell_3 V_1/I_1 \tag{IV-25}$$

if the isotropic sample is sufficiently thin. Using equations (IV-22) and (IV-23), this becomes

$$(\rho_1\rho_2)^{1/2} = H(\frac{\ell_2}{\ell_1})\,\ell_3' \,\frac{V_1}{I_1} \tag{IV-26}$$

the value of H is taken from Fig. IV.3 and ℓ_3' is the thickness of the anisotropic sample. We calculate ρ_1 and ρ_2 from eqs.

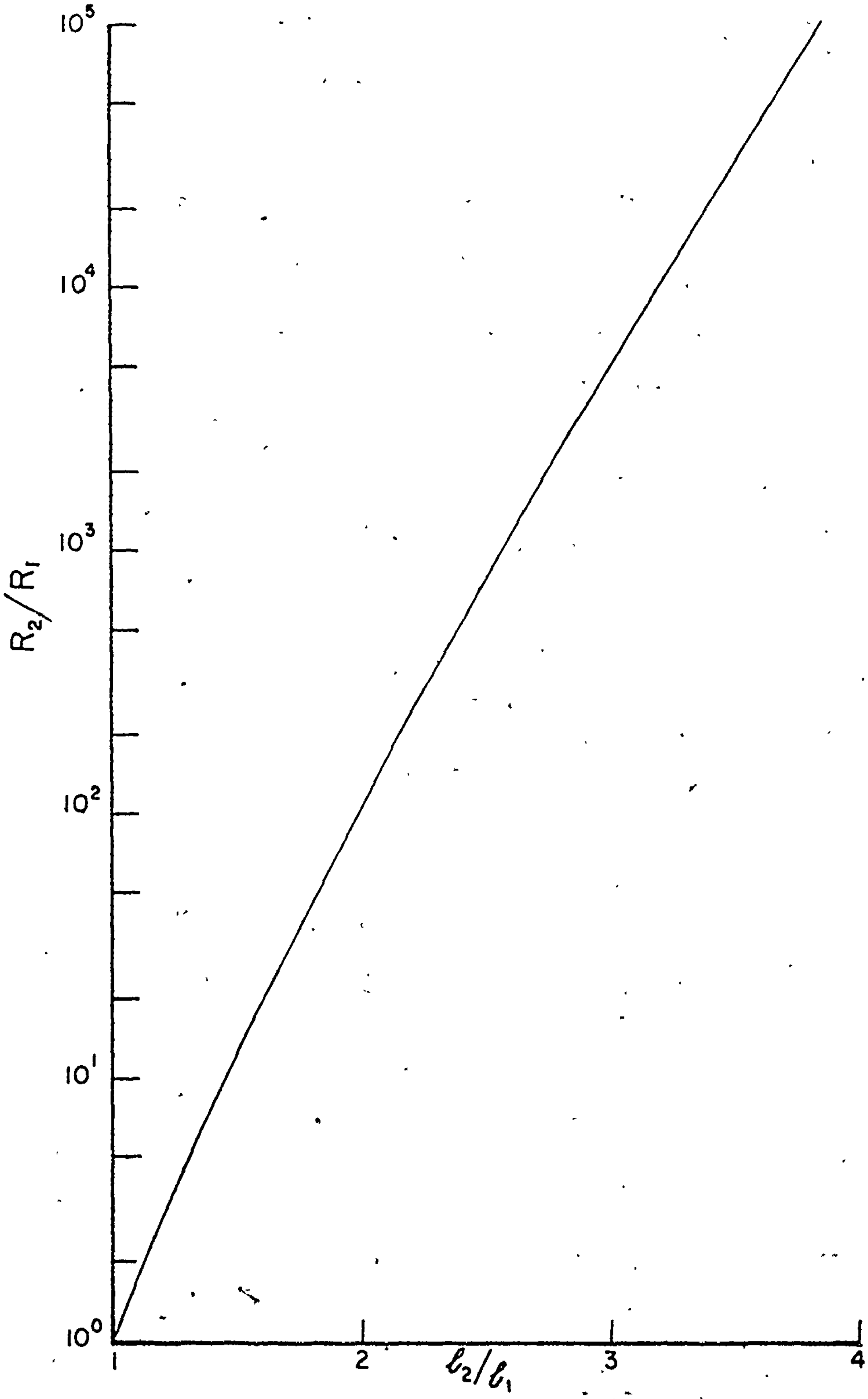

Figure IV.8

Semi-log plot of the resistance ratio, R_2/R_1, against the ratio of sample dimensions, ℓ_2/ℓ_1.

(IV-24) and (IV-26).

The Montgomery method is best suited to measuring the resistivity of anisotropic compounds because the ratio of the measured resistances, R_2/R_1, increases very rapidly with increasing values of ℓ_2/ℓ_1. This makes it possible to get a very accurate value for that ratio of lengths of the isotropic equivalent and in turn, to obtain an accurate value of the anisotropy, ρ_2/ρ_1, if the dimensions of the sample are known precisely. Also, this method reduces the problem of the exact position of the contacts on the sample because deviations from an exact rectangular arrangement are less critical than deviations from linearity when the contacts are in line (Schafer et al, 1974).

It is difficult to prepare a parallelepiped with the voltage and current probes exactly on the corners. If they are not on the corners, it is possible to solve the problem for a specific sample geometry and position of the probes. Let us look at a simple variation from the Montgomery geometry obtained by moving the probes away from the corners of the parallelepiped. Then, the infinite array of charges has four charges centered at the positions where only one charge was present previously and each of the four charges is one quarter of the charge used in the ideal case. The equations presented above are still valid if the distance of the probe from the corner is much smaller than the probe separation. For larger probe's distance from the corners, one would have to solve the problem of the isotropic sample with current probes at equivalent positions to those on the anisotropic sample. New graphs of H and R_2/R_1 against ℓ_2/ℓ_1 would have to be constructed and used as in the ideal case.

We have calculated the variation in potential across the two voltage probes for small displacements of the four contacts from the corners to determine the significance of probe displacement. This was done by calculating the second and fourth order derivative of the potential of Logan et al with respect to displacement along x and y on the parellelepiped's face.

For the case a = b = c, we have determined contours of constant percentage deviation from the value of voltage with the probes on the corners. The 1, 10 and 40 percent contours are shown in Fig. IV.9. In our experiments, the point contacts were within the region for which the deviation is smaller than 40%.

It is worthwhile to consider what happens if, at a given temperature, T_c, ρ_2 is reduced by a factor of a thousand while ρ_1 and ρ_3 stay constant. The isotropic equivalent resistivity and dimensions become

$$\rho(T_c^-) = \rho(T_c^+)/10 \tag{IV-27a}$$

$$\ell_1(T_c^-)/\ell_1(T_c^+) = \ell_3(T_c^-)/\ell_3(T_c^+) = \sqrt{10} \tag{IV-27b}$$

$$\ell_2'(T_c^-) = \ell_2(T_c^+)/10 \tag{IV-27c}$$

Defining

$$\alpha = \ell_2/\ell_1\Big|_{T_c^+}$$

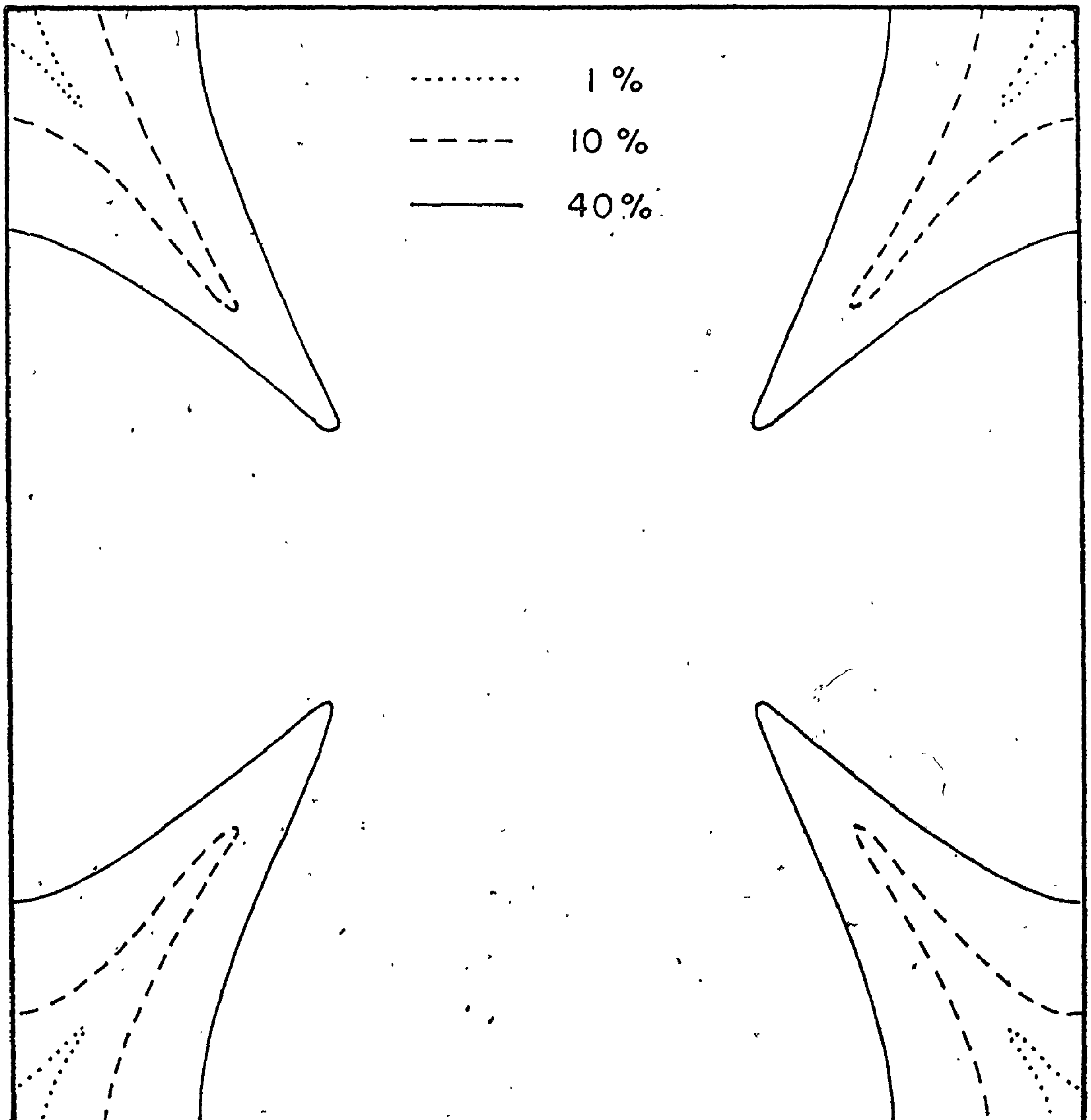

Figure IV:9

Contours of constant deviation from the value of the resistance measured when the current and voltage probes are exactly on the corner of an isotropic cube.

we get

$$\frac{R_1(T_c^-)}{R_1(T_c^+)} = (3.45\times10^{-3})\exp(\frac{13.6}{\alpha} + 3.14\alpha) \qquad \text{(IV-28)}$$

and

$$\frac{R_2(T_c^-)}{R_2(T_c^+)} = (2.90\times10^{-1})\exp[-(\frac{99.4}{\alpha} + 0.43\alpha)] \qquad \text{(IV-29)}$$

for

$$1.4 < \alpha < 20 .$$

We conclude that if there is a transition causing ρ_2 to decrease by a factor of one thousand while ρ_1 and ρ_3 remain constant, then R_1 increases by a factor greater than 1600 and R_2 decreases by a factor greater than one million in the range of ratio of sample dimensions presented above.

d. Apparatus

Resistance was measured by the Montgomery method in two ways. In one way, four platinum wire spring contacts were on the surface of a sample which rested on a moving platform which was displaced toward the contacts so as to increase the pressure exerted by the platinum wires on the surface of the sample. Alternating current at 9.8 Hz was passed through two probes and the voltage at the same frequency ~~detected at the~~ other two probes was amplified and recorded.

In the second experimental arrangement, the sample was held between two sets of four spring loaded pins (Fig. IV.10),

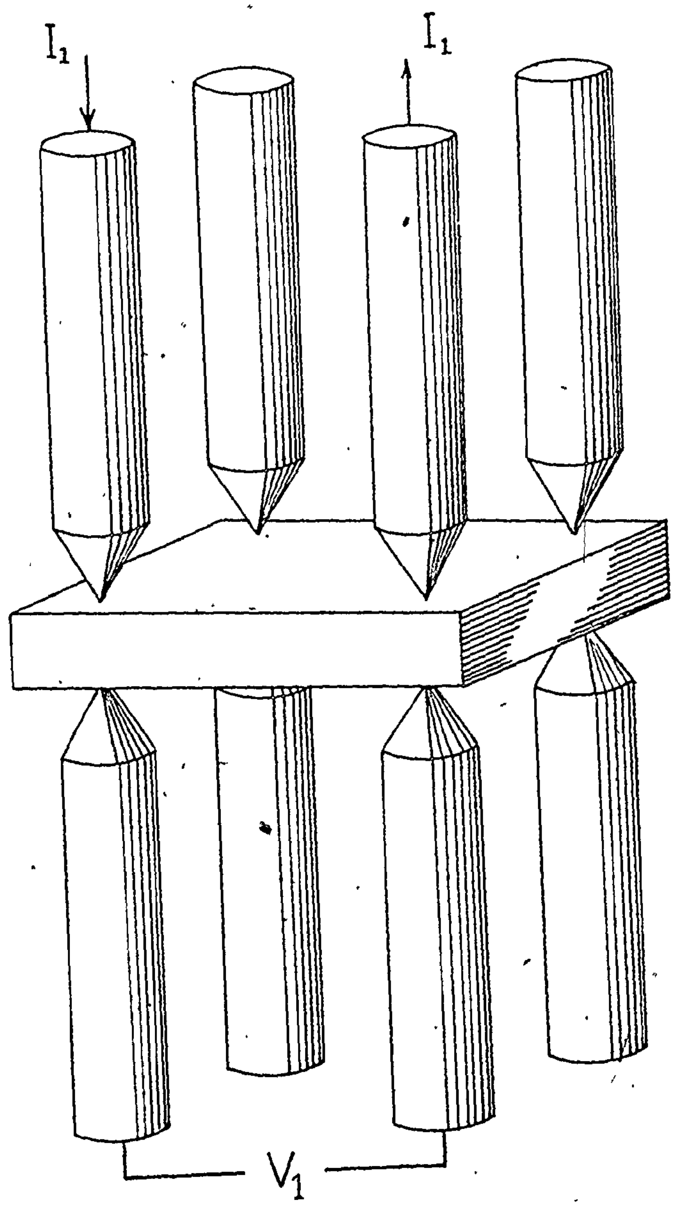

Figure IV.10

Experimental arrangement to measure the resistivity. The flat rectangular sample is held in place by eight pins. Two pins carry the applied current, I_1, and two others probe the voltage, V_1.

The contact pins ran through holes that were 2 or 4 mm apart in teflon discs above and below the sample. The direction of the current between two pins was reversed every five second and the voltage detected between any two of the six remaining contacts was rectified and averaged with a time constant of 20 sec. The current was usually 30 mA but could be increased to 100 mA for the measurement of small resistances.

In the first experimental arrangement, measurements of the anisotropy were obtained with the platinum wire contacts on one face which was approximately 30° away from a (100) face. The resistivity along a direction making an angle α with the c axis is

$$\rho(\alpha) = \rho_c \cos^2\alpha + \rho_a \sin^2\alpha \ . \qquad \text{(IV-30)}$$

If the anisotropy is larger than 50 and the angle α is smaller than 30°, the resistivity along the c axis is simply

$$\rho_c = \rho(\alpha)/\cos^2\alpha \ . \qquad \text{(IV-31)}$$

With the second arrangement, combinations of contacts directly opposite on the top and bottom faces were used to measure ρ_c and ρ_a as shown in Fig. IV.10.

For both arrangements, R_2 and R_1 were measured at different times. The analysis of Montgomery was then used assuming the ideal case of contacts on the corners.

e. Results and Discussion

1. Anisotropy

The resistivity anisotropy is obtained from the product of the ratio of dimensions of the isotropic equivalent with the corresponding ratio in our sample as shown in eq. (IV-24). The sample dimensions are not measured accurately because all the sample handling is done inside a dry box. However, these dimensions are fixed for a given crystal and we can write

$$\frac{\rho_c}{\rho_a} = \left(K \frac{\ell_2}{\ell_1}\right)^2 . \qquad \text{(IV-32)}$$

Calculations of the uncertainty in the anisotropy do not take account of the error in K since it is a systematic error. The anisotropy obtained by Van Schyndel (1976) using the first experimental arrangement is shown in Fig. IV.11 between 4.2 and 250 K. The error bars on this plot reflect the variation in R_1 and R_2 in different experiments on different days. Within one experiment, the error in R_1 or R_2 is small as shown by the continuity of the line joining the points on this graph.

From the graph, we can see that the anisotropy is in the range 95±10 between 40 and 180 K, increases by 10% between 180 and 240 K and increases by 15% between 40 and 15 K.

Measurements of the anisotropy with the second arrangement confirmed this anisotropy and showed that in some cases

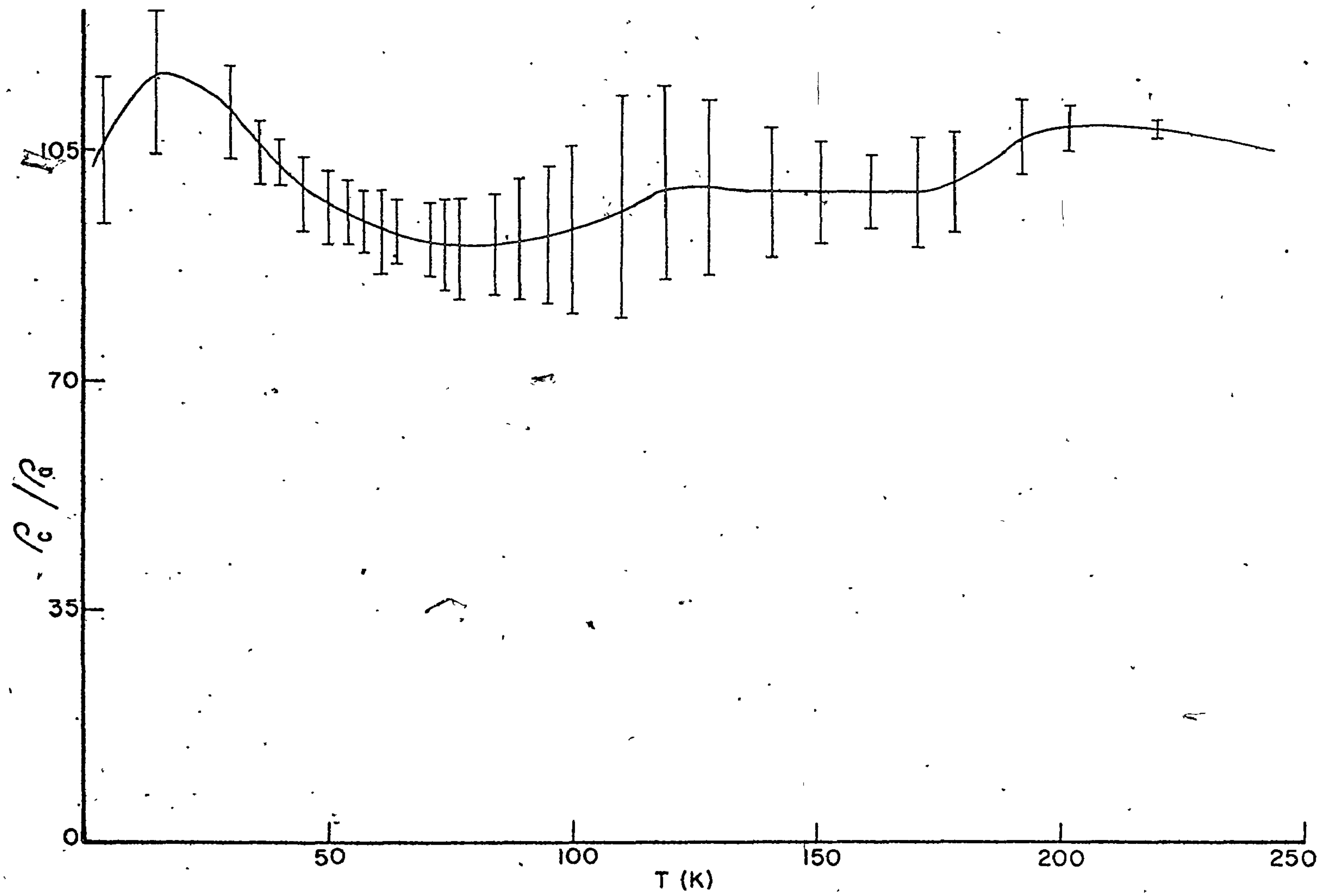

Figure IV.11

Experimental resistivity anisotropy as a function of temperature for $Hg_{3-\delta}AsF_6$. Error bars represent the variation in anisotropy from day to day while the continuous line follows the anisotropy over one day.

the increase in anisotropy below 40 K could be as much as 80%.

The temperature dependence of the anisotropy can be compared with our theoretical calculation of ρ_c/ρ_a in section IV.b (Fig. IV.5). The theoretical anisotropy remains within 2% of its average value between 50 K and 300 K while the variation in the experimental anisotropy is only 10% over the same range with the largest increases occuring at 110 K and 185 K. These increases could be due to short-range and long-range ordering of the chains occuring at 180 K and 120 K respectively which are not considered in the theory. Below 50 K, the theoretical and experimental anisotropies increase by the same percentage when the temperature is lowered to 15 K. This increase is due to the exponential decrease with temperature of three of the four resistivities contributing to the resistivity in the ab plane, $\rho_{||}^{3D}$, $\rho_{||}^{1D}$, $\rho_{\perp}^{3D}$ while the fourth resistivity, $\rho_{\perp}^{1D}$, becomes proportional to T^2. Below 15 K, the theoretical anisotropy decreases linearly because the resistivity in the ab plane is dominated by the residual resistivity. Experimentally, we observed that the anisotropy does start to decrease at these low temperatures but the exact temperature dependence in that region could not be asserted because of the lack of experimental data in that region.

The position and height of the peak in anisotropy between 0 and 50 K depends on the value of the residual resistivity and to a lesser extent, on the value of the Debye temperatures involved in the resistivity in the ab plane. In some samples, we did observe a larger increase in anisotropy extending to lower temperatures which suggests that the residual resistivities were lower for these samples than for the sample whose anisotropy is shown in Fig. IV.11.

2. Temperature dependence of the resistivity

From eqs.(IV-24) and (IV-26), the resistivities ρ_2 and ρ_1 are given by

$$\rho_2 = \sqrt{\frac{\rho_2}{\rho_1}}\, H\left(\frac{\ell_2}{\ell_1}\right) \ell_3' R_1 \qquad \text{(IV-33a)}$$

$$\rho_1 = \sqrt{\frac{\rho_1}{\rho_2}}\, H\left(\frac{\ell_2}{\ell_1}\right) \ell_3' R_1 \ . \qquad \text{(IV-33b)}$$

If the anisotropy is independent of temperature, then R_1 is the only temperature dependent term in these equations and we have

$$\rho_i(T)/\rho_i(T_0) = R_1(T)/R_1(T_0) \ . \qquad \text{(IV-34)}$$

In this case, the temperature dependence of the resistivity is independent of the sample dimensions.

By symmetry, the ab face of the mercury chain compound has to be isotropic and we have shown above that the ratio of the resistivity along the c and a axes is constant between 40 and 150 K. However, between 90 and 250 K, we will show that the resistance presents large anomalies. Therefore, we limit our analysis of the temperature dependence of the resistivity to the region below 90 K.

The average of the resistance R_1 normalized to its value at 90 K measured on the isotropic faces of three samples is plotted between 4.2 and 90 K in Fig. IV.12. The average deviation between the three samples is about 15%. The resistivity is linear between 90 K and 40 K with a slope of 16×10^{-3} K^{-1} and an extrapolated intercept on the temperature axis at 20 K. The resistance measured between 40 K and 90 K on anisotropic faces for another set of three samples shows the same temperature dependence.

Also, the same quantity, $R_1/R_1(90\ K)$, averaged for the isotropic faces of two samples is plotted on a log-log graph (Fig.IV.13) from 90 K to 4.2 K. From 90 K down to 40 K the log-log graph is linear with a slope of 1.34 and between 10 and 25 K, it is linear with a slope of 2.58. Below 10 K, the resistivity changes more slowly and becomes constant below 6 K.

The linear temperature dependence of the resistivity for the isotropic faces between 20 and 90 K (Fig. IV.12) is similar to the one obtained theoretically for the four types of scattering acting on our cylindrical FS (Fig. IV.2). The extrapolation of the linear section of the graph crosses the temperature axis at 20 K. This is in good agreement with an intercept at 30 K for the theoretical resistivity, $\rho_{\perp}^{1D}$ and between 10 and 15 K for the other three types of scattering.

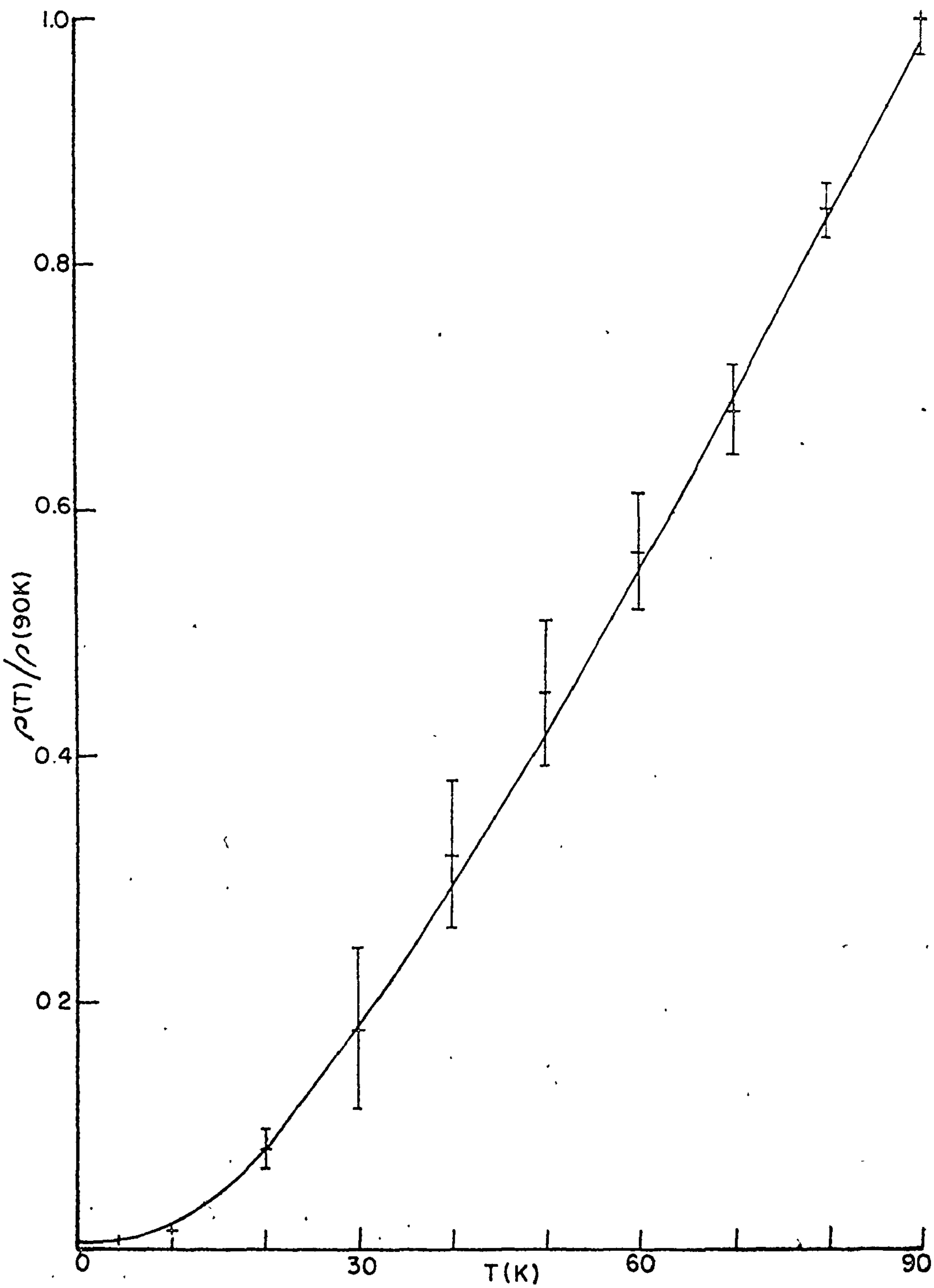

Figure IV.12

Average resistivity on the isotropic faces of three samples of $Hg_{3-\delta}AsF_6$ normalized to the resistivity at 90 K. The solid line represents a fit of this average with the resistivity model.

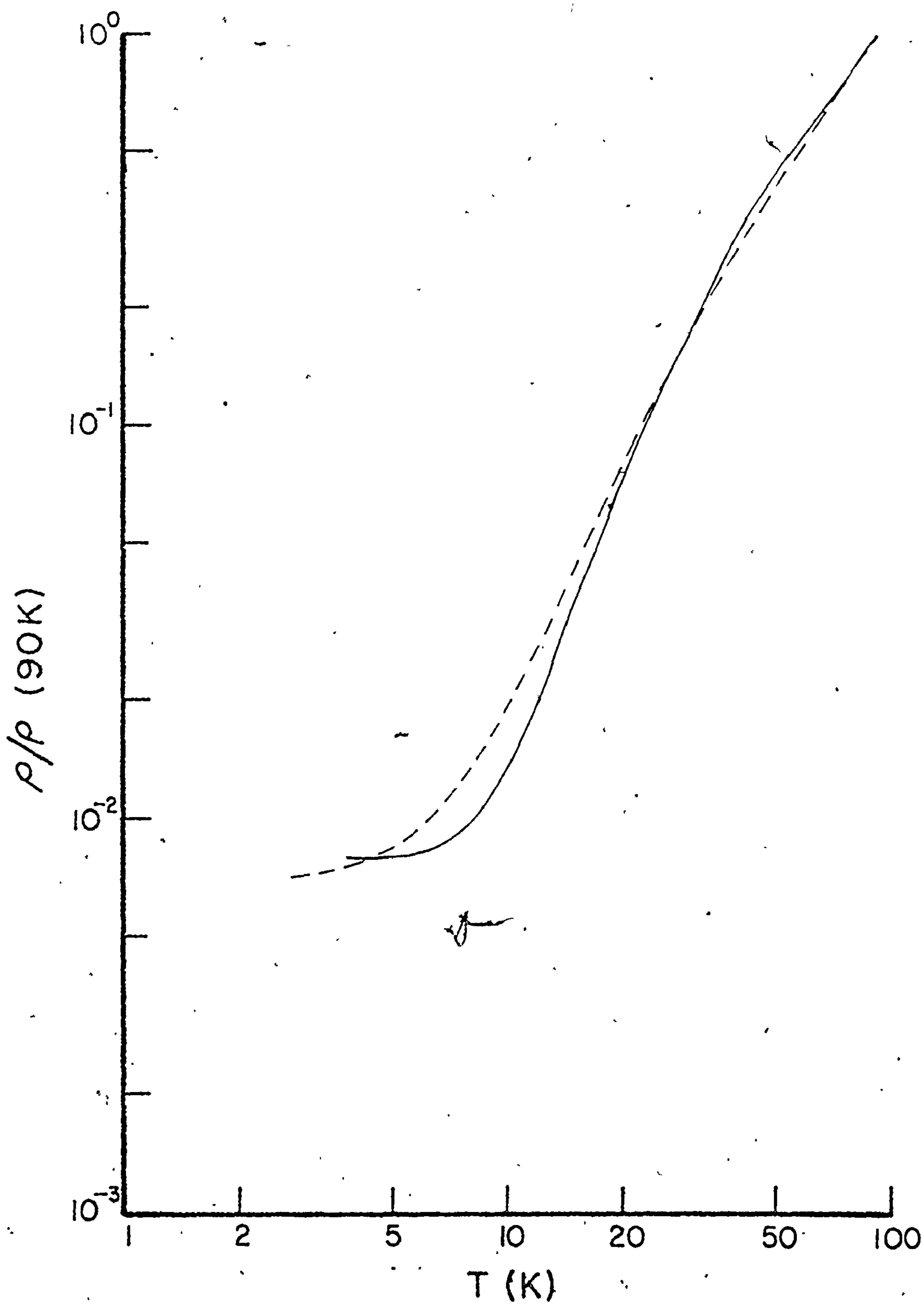

10^0
10^{-1}
10^{-2}
10^{-3}
ρ/ρ (90K)
1
2
5
10
20
50
100
T (K)

Figure IV.13

Log-log plot of the average of the resistivity on the isotropic faces of two samples against temperature for $Hg_{3-\delta}AsF_6$. The solid line is the experimental curve and the dashed line is a fit of the data with the resistivity model.

Also, the temperature dependence of the resistivity obtained from anisotropic faces beteen 40 and 90 K is in very good agreement with the one discussed above. This confirms our previous finding that the anisotropy is constant in that temperature range.

The solid line in Fig. IV.12 and the dashed line in Fig. IV.13 are fits of the resistivity to eq. (IV-15) with the coefficients for $\rho_{\perp}^{3D}$, $\rho_{||}^{1D}$, $\rho_{||}^{3D}$ being equal. We impose this constraint because the temperature dependence of these three resistivities is very similar over the temperature range in which we are trying to obtain a fit. The fit obtained with the parameters $\alpha = .55, \beta = \gamma = \varepsilon = 0.14, \rho_0/\rho(T_0) = .0065, T_0 = 90$ K is very good between 20 and 90 K but shows some significant deviation below 20 K. This could be due to the values of the one-dimensional and three-dimensional phonon Debye temperatures used in calculating the four types of resistivities. These values were estimated from the slope of the phonon dispersion curves measured by Heilmann et al (1979).

At temperatures below 10 K, our theoretical resistivity becomes proportional to T^2. However, it is not possible to verify this because, at these temperatures, the experimental resistivity is dominated by a residual resistivity for all the samples we studied. This is unusual because previous workers have reported no evidence of residual resistivity down to liquid helium temperatures and it suggests that our samples contain more crystalimperfections than the samples used previously but it also demonstrates that there is no mechanism to short out the residual resistivity in these compounds as had been suggested earlier (Chakraborty et al, 1978).

In analyzing our graphs of resistivity against temperature, we stated that the resistivity was linear between 40 and 90 K when it was plotted on a linear scale but we also stated that it has a slope of 1.34 when plotted on a log-log scale over the same temperature range. The apparent contradiction stems from the fact that the linear section of the resistivity on the linear scale does not extrapolate to the origin so that, over that range, the resistivity cannot be expressed by $\rho = aT$, which would result in a slope of unity on a log-log graph, but by $\rho = a(T-T_0)$. This emphasizes the danger in attributing a special significance to the slope of the resistivity over a certain temperature range on any scale without a model that accounts for the temperature dependence of the resistivity over as wide a temperature range as possible. This is particularly true of the resistivity which shows a variety of temperature behaviours depending on the many possible conduction and scattering mechanisms.

In that respect, our model of the resistivity constructed from the measured Fermi surface and phonon dispersion curves is the first attempt at ~~fitting~~ the resistivity over a large temperature range (4 - 90 K). It remains to be shown that in a sample with lower residual resistivity, the lattice resistivity would follow a T^2 dependence at temperatures below 4 K as predicted by this model.

3. Hysteresis in the resistivity

In their resistivity measurements, Cutforth et al (1977) noted evidence for a phase transition at 220 K in $Hg_{3-\delta}SbF_6$ and $Hg_{3-\delta}AsF_6$. Chang et al (1977) observed similar anomalies in $Hg_{3-\delta}AsF_6$ at 220 K.

After investigating the low temperature resistivity of each sample, the resistance on isotropic and anisotropic faces was measured while alternatively raising and lowering the temperature in the range 150 to 250 K.

Fig. IV.14 shows the resistance measured on an isotropic face as it is cooled from 290 to 170 K and then warmed from 150 to 260 K. Fig. IV.15 shows the resistance measured on an anisotropic face of a different sample as it is warmed from 100 to 240 K and then cooled down to 120 K.

When the two samples are cooled, the resistances, which are practically constant between 250 and 220 K, increase suddenly at 217±3 K. The resistances do not retrace this resistance step when the samples are warmed up but increase with increasing temperature and level off above 235 K. The resistances at the end of the temperature cycles, at 250 K on the isotropic face and at 120 K on the anisotropic face, are then larger than at the beginning of the cycles. Variation in the differences between the resistances measured during warming and cooling could not be observed on subsequent cycles because more than one cycling resulted in large discontinuities in the

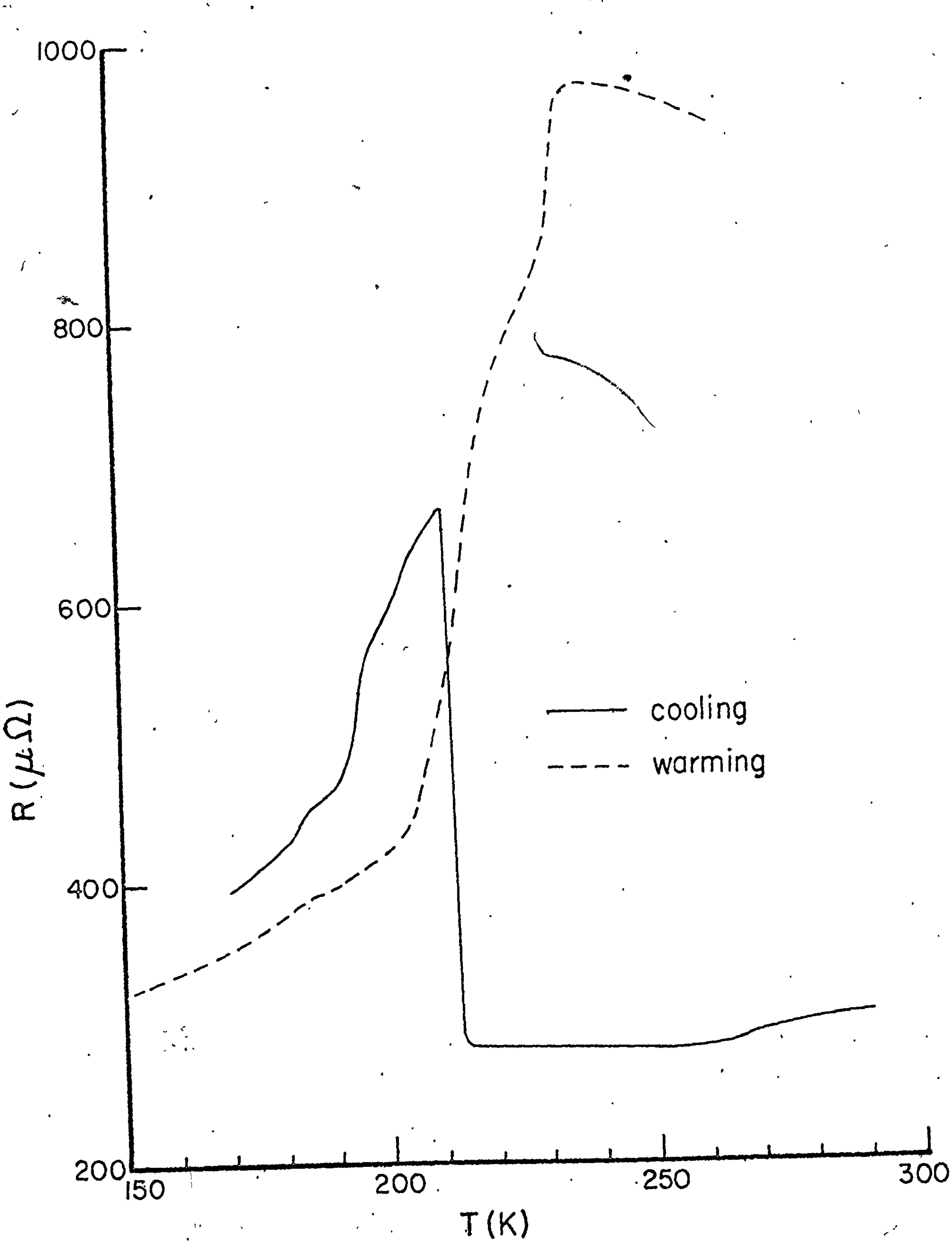

Figure IV.14

Resistance on an isotropic face of a sample of $Hg_{3-\delta}AsF_6$ as the sample is cooled 290 to 170 K and to 260 K.

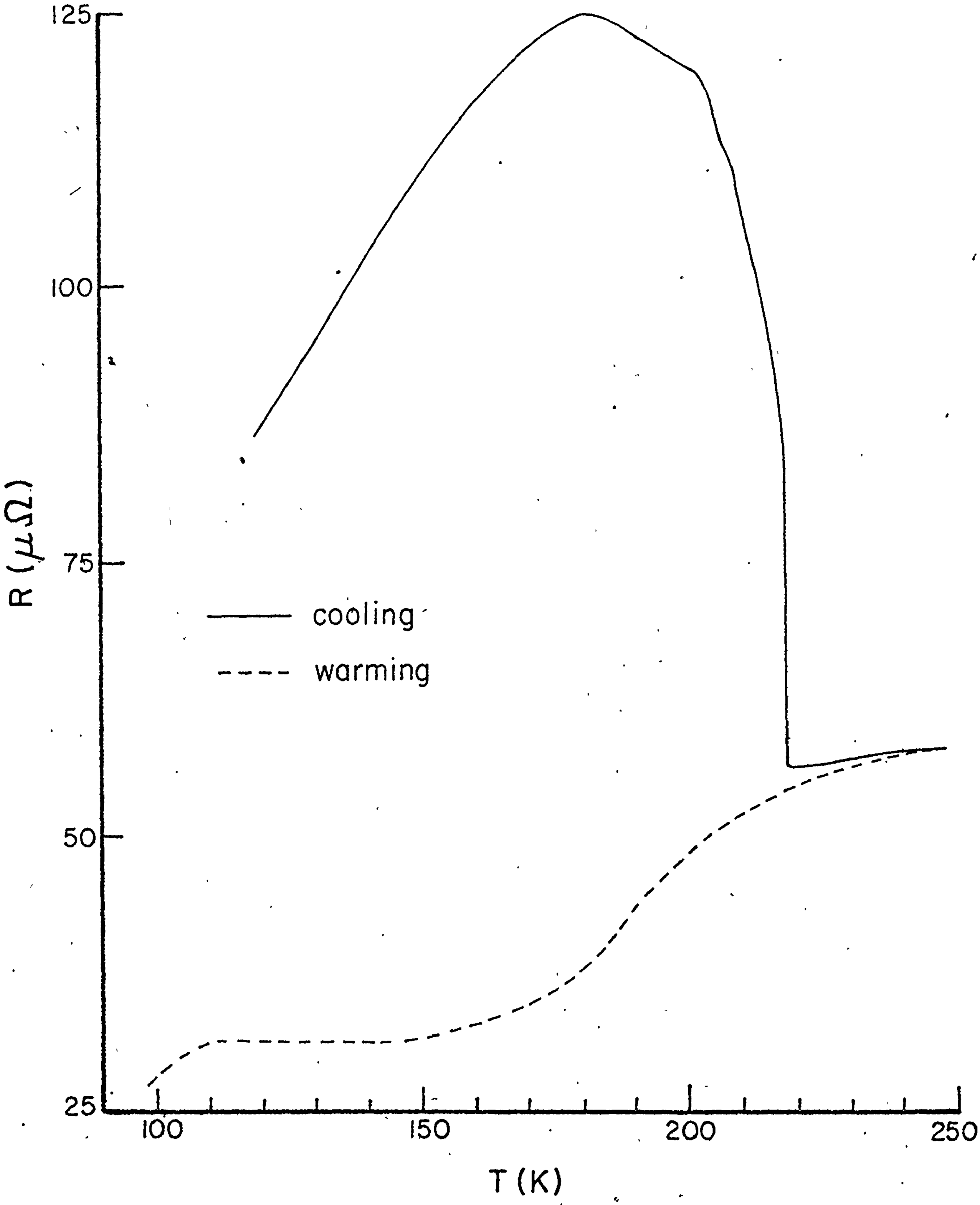

Figure IV.15

Resistance on an anisotropic face of a sample of $Hg_{3-\delta}AsF_6$ as the sample is warmed from 100 to 240 K and then cooled to 120 K.

current through the sample.

The step in resistance at 217 K in the cooling curves for both the isotropic and anisotropic faces indicates a transition in the crystal at 217 K as the temperature is lowered. This change is not observed at 217 K during the warming cycle indicating hysteresis, i.e. a difference between warming and cooling. The exact nature of the crystal change is not understood at the present. However, it is related to the extrusion of mercury which is observed during cooling at 210±10 K by differential thermal analysis (Datars _et al_, 1979).

The increase in resistance with increasing temperature levels off at 235 K during warming. This is the temperature at which the melting of the extruded mercury is observed during warming in differential thermal analysis.

However, this does not imply that the resistance increase at 217 K upon cooling is caused by the freezing of elemental mercury trapped in the sample because this would result in a decrease in resistance as the resistivity of mercury decreases by a factor of four when it goes from the liquid to the solid phase.

The resistances at the end of a temperature cycle through 217 K were larger than at the beginning of the cycle indicating that some irreversible changes take place in the samples during the cycling.

Other anomalies in the spin-lattice relaxation time

(Ehrenfreund et al, 1977), the magnetic susceptibility (Wei et al, 1977) and the thermopower (Scholz et al, 1977) have also been observed near 217 K. Neutron scattering measurements by Pouget et al (1978) in that temperature range did not show any evidence of a crystallographic transition but resulted in two of their three samples breaking up after several cycles in temperature.

The resistance data presented in Figs. IV.14 and IV.15 confirm that an unusual transition takes place at 217 K. It is not a simple crystallographic transition because, in that case, it would be observed upon warming and cooling of the sample. Instead, it is proposed that the jump in resistance at 217 K is due to macroscopic defects distributed uniformly through the sample so that the resistivity along all directions increases. These defects are caused by the differential contraction of the hexafluoride anion lattice with respect to the mercury chains. This contraction leads to the extrusion of mercury observed in the DTA experiments of Datars et al. The macroscopic defects are not annealed when the sample is warmed up, explaining the irreversible nature of the transition. More than one cycling will cause large discontinuities in the current through the sample because a large number of defects will eventually destroy the sample's integrity.

CHAPTER V

SUPERCONDUCTIVITY

a. Introduction

$Hg_{3-\delta}AsF_6$ was first reported to be superconducting by Chiang et al (1977). They noted that the resistivity along the c-axis dropped by at least three orders of magnitude in an interval of 0.2 K of 4 K while the resistivity in the ab plane did not show any discontinuity. They measured a critical field of 380 G at 1.4 K for this transition. Magnetization measurements at five fields between 0 and 100 Gauss were presented afterwards by Spal et al (1977), showing an anisotropic Meissner effect in this compound. At fields of 0.015 Gauss, the magnetization appeared at 4.10 K and was larger for $\vec{H}$ parallel to $\vec{a}$ than for $\vec{H}$ parallel to $\vec{c}$. The magnetization increased between 4.1 and 1.9 K but, even when the field was parallel to the a axis, reached only 20% of total flux exclusion. Finally, in an extension of the previous measurements down to 0.3 K, Spal et al (1979) found that the compound shows complete flux exclusion below 0.43 K with a critical field of 20 Gauss. In that state, the compound does not show magnetization anisotropy. They also confirmed that the magnetization is anisotropic above 0.43 K and showed that this anisotropy reaches a maximum of 15 at 3.5 K in a field of 0.015 G. The similarity in the critical field and temperature of metallic mercury and the critical field and temperatures of this compound led Datars et al (1978) to suggest that the observed effects were caused by films of mercury extruded onto the anisotropic surfaces of the compound. Differential thermal analysis showed that this extrusion occured at 195 K. Spal et al (1979) studied an ac face of a crystal of this compound by X-ray fluorescence at six temperatures between 120 and 300 K. They assigned an upper limit of 500 Å to the thickness of any mercury film on it. This corresponds to approximately one hundred layers of mercury atoms and does not preclude the existence of elementary mercury deposited in internal regions of the sample.

In order to establish more precisely the nature of the magnetization transition, we have measured the differential susceptibility of powders and single crystals of $Hg_{3-\delta}AsF_6$ between 4.2 and 1.2 K in fields of 0 to 400 G. Also, results of our measurements of the resistivity of single crystals in the same temperature range will be discussed.

b. Experimental techniques

Powders of $Hg_{3-\delta}AsF_6$ are obtained by crushing polycrystalline samples. The powders are quite coarse and not very uniform because we want to limit the contact between our samples and any water containing surface. The single crystals used in this study are picked up for their well faceted faces and for dimensions that fit the sample holder. Typical crystal sample dimensions are $2\times1\times0.5$ mm^3. The samples are inserted inside Kel-F cylindrical sample holders of 3 mm diameter.

The ac magnetic susceptibility is measured with the coil arrangement used to measure the dHvA effect. The assembly is inserted between the poles of an electromagnet for the powders and inside a superconducting magnet for single crystal samples. The electromagnet provides a field transverse to the axis of the detection coil while the field of the superconducting magnet is parallel to the coils' axis.

The single crystal samples are placed in the sample holder such that the c axis is along the axis of the coils and these sample holders can be rotated with respect to an axis perpendicular to the c axis.

The modulation coil is driven at 517 Hz and the inductive pick-up voltage at the same frequency is recorded as the magnetic field is increased from negative to positive fields at a rate of 1 G/sec. The temperature is maintained constant by regulating the vapor pressure of the helium bath in which the coils are immersed.

c. <u>Results</u>

Three different powder samples were investigated in the course of this study. Fig. V.1 shows curves of pick-up voltage as a function of magnetic field for one of these powders at several temperatures. At 4.2 K, the trace does not show any

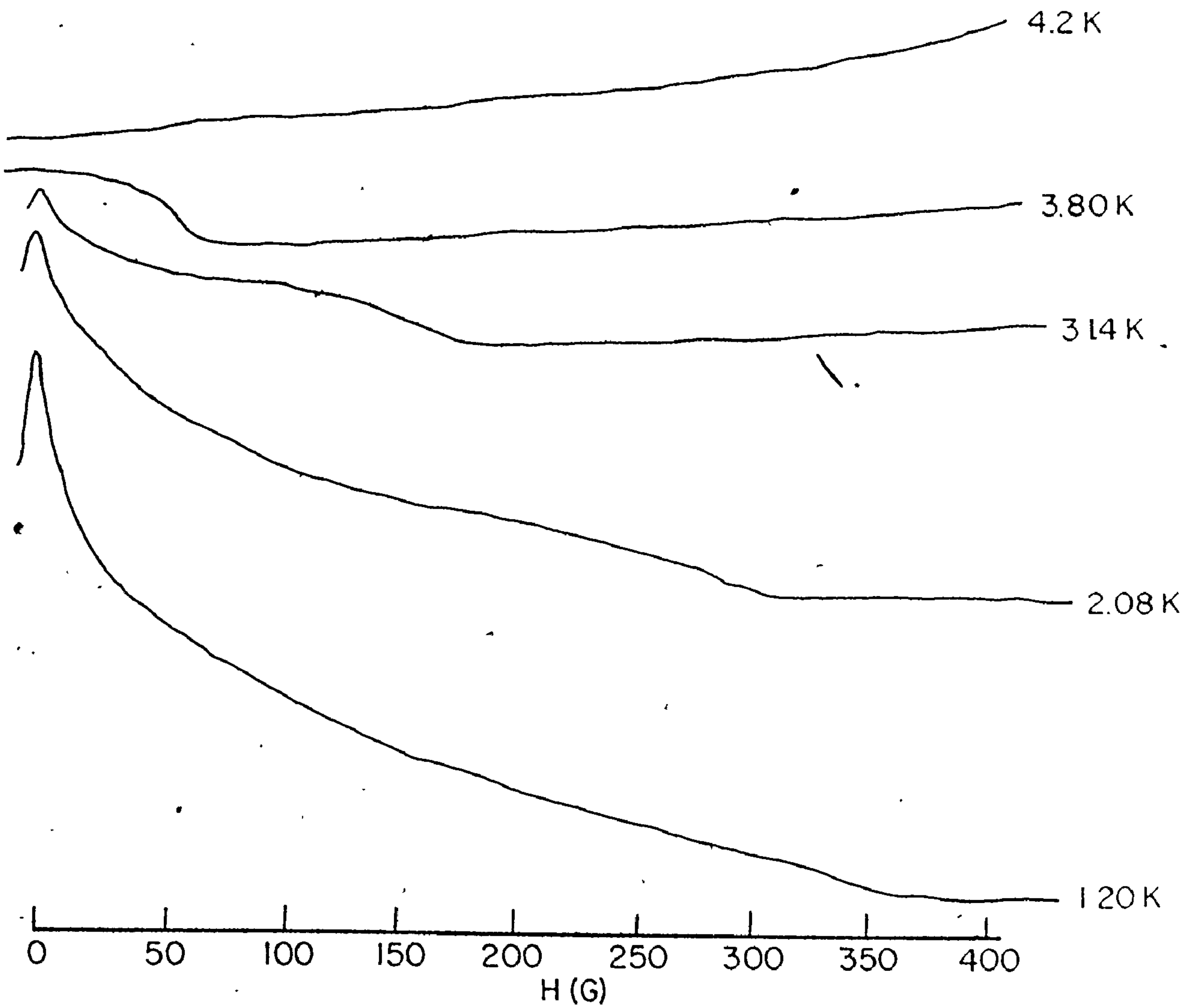

Figure V.1

Chart recorder traces of pick-up voltage as a function of magnetic field at five temperatures for a powder of $Hg_{3-\delta}AsF_6$.

feature apart from a slow variation of the total pick-up. At 3.8 K, there is a transition at 50 Gauss. Below this temperature, this transition moves to higher fields. There also appears at 3.4 K a feature at a lower field. This feature grows rapidly in size with lowering temperature but exists over the same magnetic field range as the temperature is lowered. In contrast, the high field transition does not change size and occurs at higher fields as the temperature is lowered. It appears that there are two independent features in this data since the low field feature is not present at 3.8 K where the high field transition is present.

The difference between the signal at zero field and the signal at the shoulder occurring before the high field transition is a measure of the zero-field susceptibility, $\chi(0)$. When $\chi(0)$ is plotted as a function of temperature (Fig. V-2), a critical temperature of 3.58 K is extrapolated. Similar plots for the other two powders gave critical temperatures of 3.2 and 3.38 K.

If the field corresponding to the completion of the high field transition is plotted as a function of the square of the temperature (Fig. V.3), a straight line is obtained as predicted by the empirical relation

$$H_c/H_c(0) = 1-(T/T_c)^2 \ .$$

The critical magnetic field and temperature extrapolated from this graph are 404 Gauss and 4.123 K. These are very close to

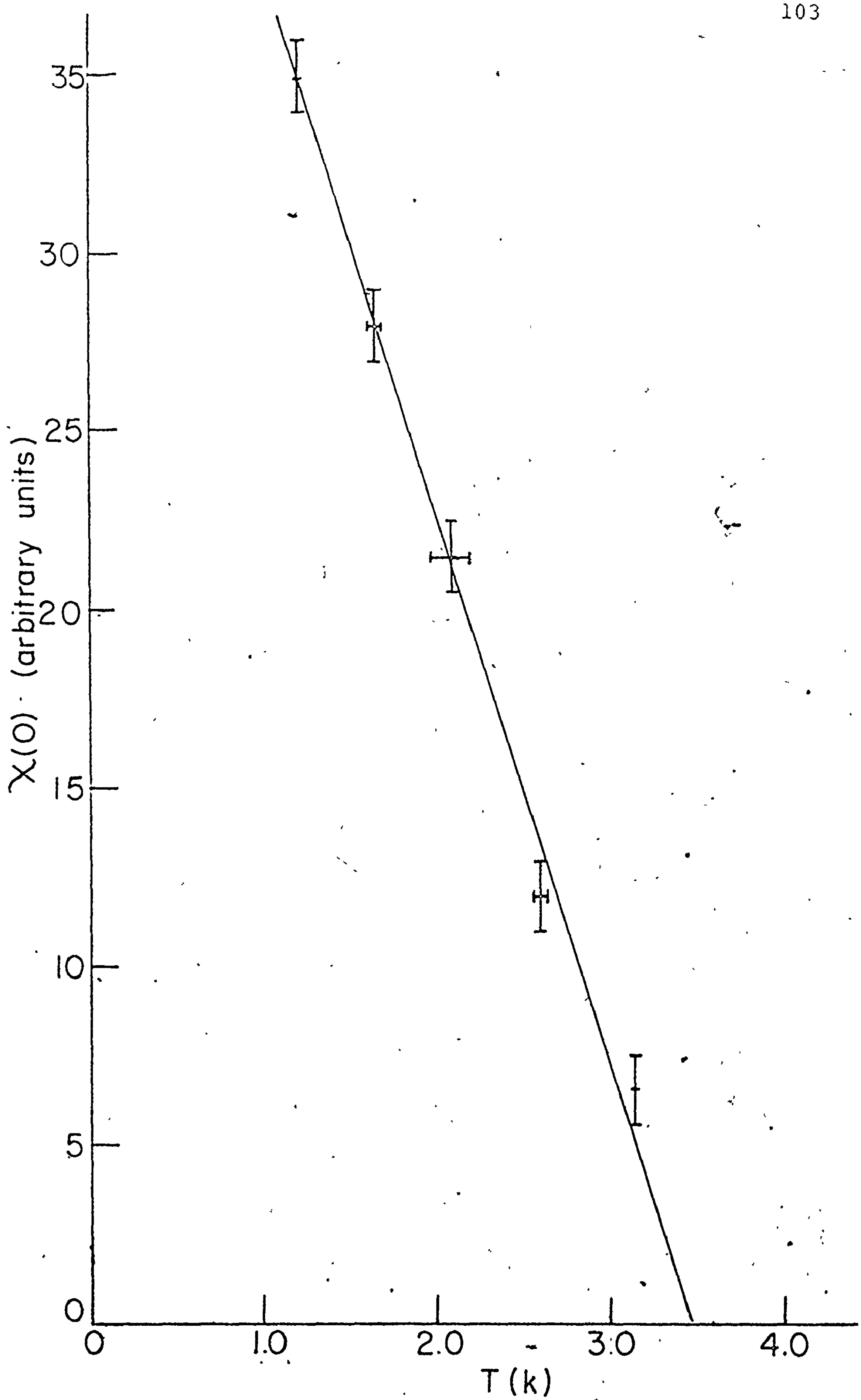

35
30
25
20
15
10
5
0
0
1.0
2.0
3.0
4.0
T (k)
χ(0) · (arbitrary units)

Figure V.2

Zero field susceptibility, $\chi(0)$, as a function of temperature for a powder of $Hg_{3-\delta}AsF_6$. Solid line is a linear fit to the data points. The absolute value of the voltage was recorded so that $\chi(0)$ appears to be positive even though the superconducting state is diamagnetic implying a negative $\chi(0)$.

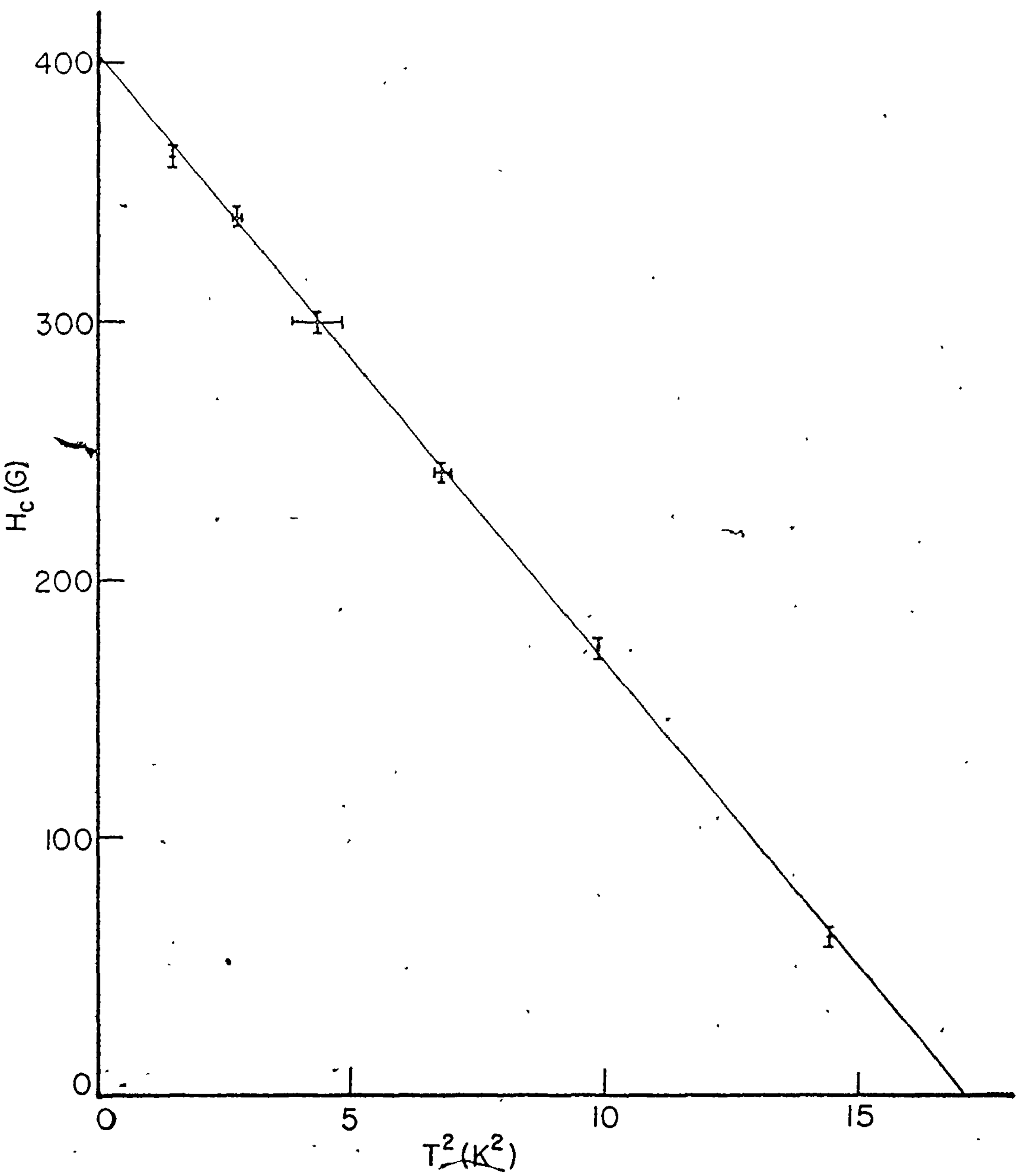

Figure V.3

Critical field for the high field transition in a powder of $Hg_{3-\delta}AsF_6$ as a function of the square of the temperature. Solid line is a linear fit to the data points.

the corresponding quantities for metallic mercury (H_c = 412 Gauss, T_c = 4.153 K).

When the powder sample was warmed to room temperature and cooled down again, the two features of the data were still present but the high-field transition became six times larger while the low-field feature stayed approximately the same. The critical temperature of the low-field effect increased with thermal cycling. For one powder sample, it changed from 3.2 K to 3.4 K to 3.7 K after successive temperature cycles to room temperature.

Seven "single crystals" were investigated in this work. Of these seven crystals, only one showed sufficient anisotropy in its susceptibility to be consistent with the magnetization reported by Spal et al (1977). With the magnetic field parallel to the c axis, a change in the susceptibility at low fields appeared at 4.08 K in this sample. This change extended to higher fields and became larger as the temperature was lowered. Also, there was no evidence of a transition that could be attributed to mercury at higher fields. At 3.5 K, the sample was rotated until the magnetic field was perpendicular to the c axis. In this configuration, the transition occured at a four times lower field (Fig. V.4) and a small dip appeared at the magnetic field where the slope of the voltage was steepest with the field parallel to the c-axis. Further cooling with the field perpendicular to the c-axis showed that the transition

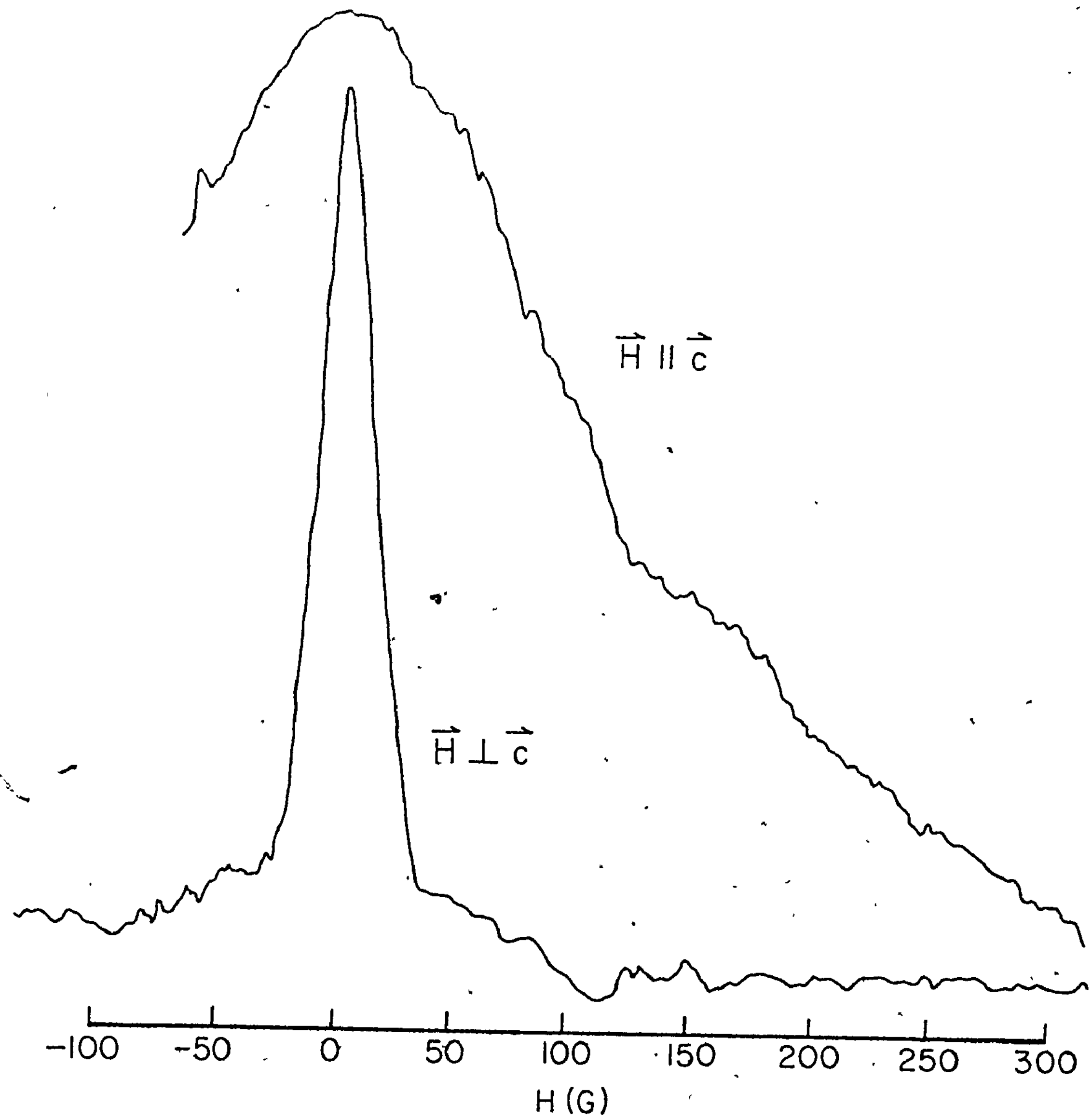

Figure V.4

Chart-recorder traces of pick-up voltage as a function of field at 3.46 K in a single crystal of $Hg_{3-\delta}AsF_6$ when the magnetic field is parallel to the c axis and when it is perpendicular to the c axis.

moved to higher fields. The critical field reached 200 G at 1.25 K. When the sample was rotated at 1.25 K, the transition occured again at a minimum when the field was perpendicular to $\vec{c}$ but the anisotropy in critical field decreased. Fig. V.5 shows a plot of the critical field against the angle away from the c axis at 1.25 K.

Plots of the voltage at zero field and the field at which the transition occured versus temperature with the magnetic field perpendicular to the c axis extrapolated to a critical temperature of 3.75 K (Fig. V.6).

After temperature cycling to liquid nitrogen temperature, this critical temperature increased to 3.97 K and a separate feature, a dip in the signal, appeared between 4.15 K and 4.10 K as shown in Fig. V.7. This feature occurs at higher fields as the temperature is lowered and appears to be due to elemental mercury. A third experiment with the same sample showed an increase of the critical temperature to 3.986 K. The anisotropy of the critical field for the low field transition was found to be 5. at 3.85 K.

For the other six single crystal samples, the transition at low field appeared at lower temperatures or was not detected even at the lowest temperature. When it was present, it did not show significant anisotropy when the sample was rotated.

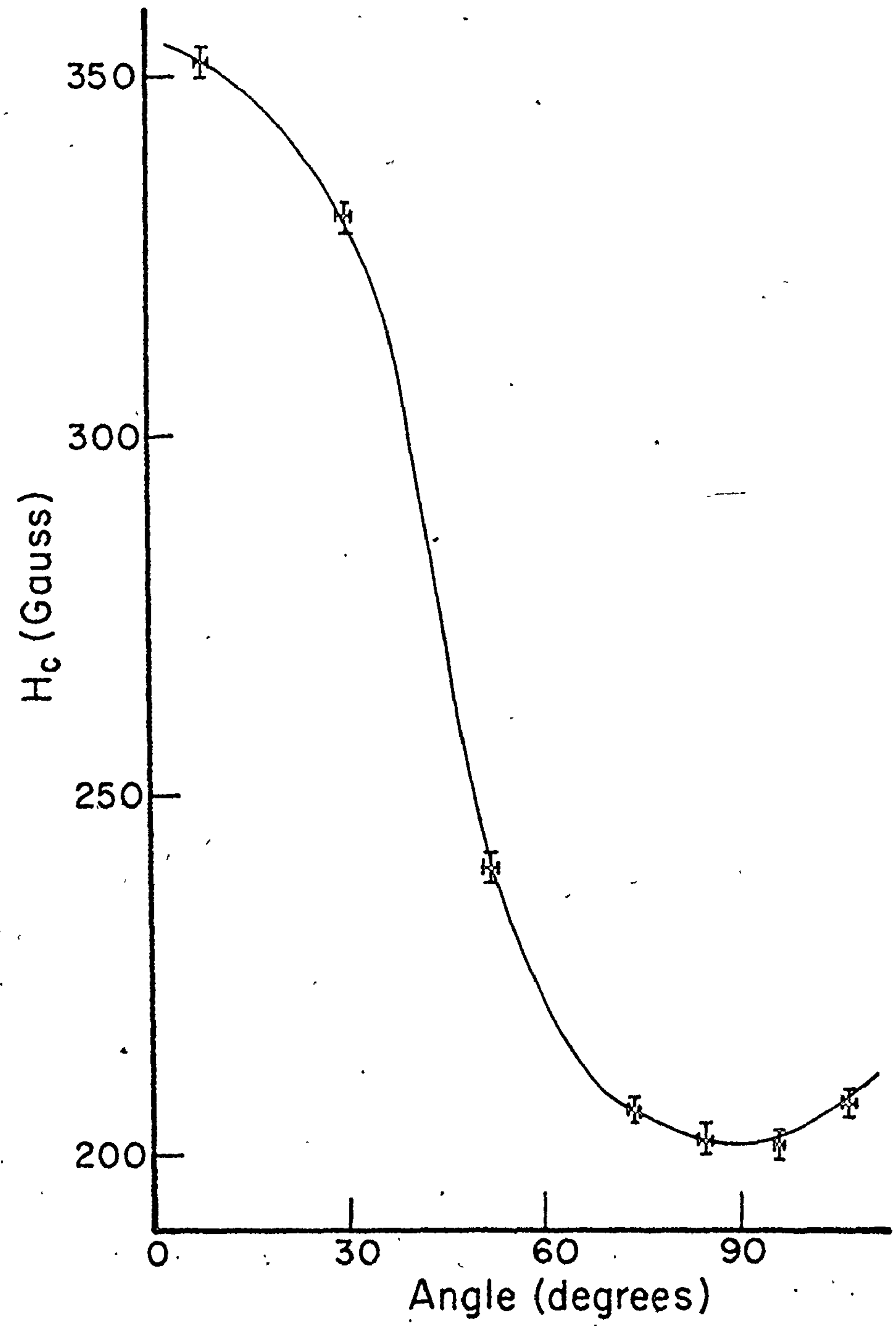

Figure V.5

Critical field as a function of angle away from the c axis at 1.25 K in $Hg_{3-\delta}AsF_6$. Solid line is drawn to guide the eye.

Figure V.6

Zero-field susceptibility and critical field of a single crystal of $Hg_{3-\delta}AsF_6$ as a function of temperature. Hand-fitted solid lines are used to extrapolate the critical temperature.

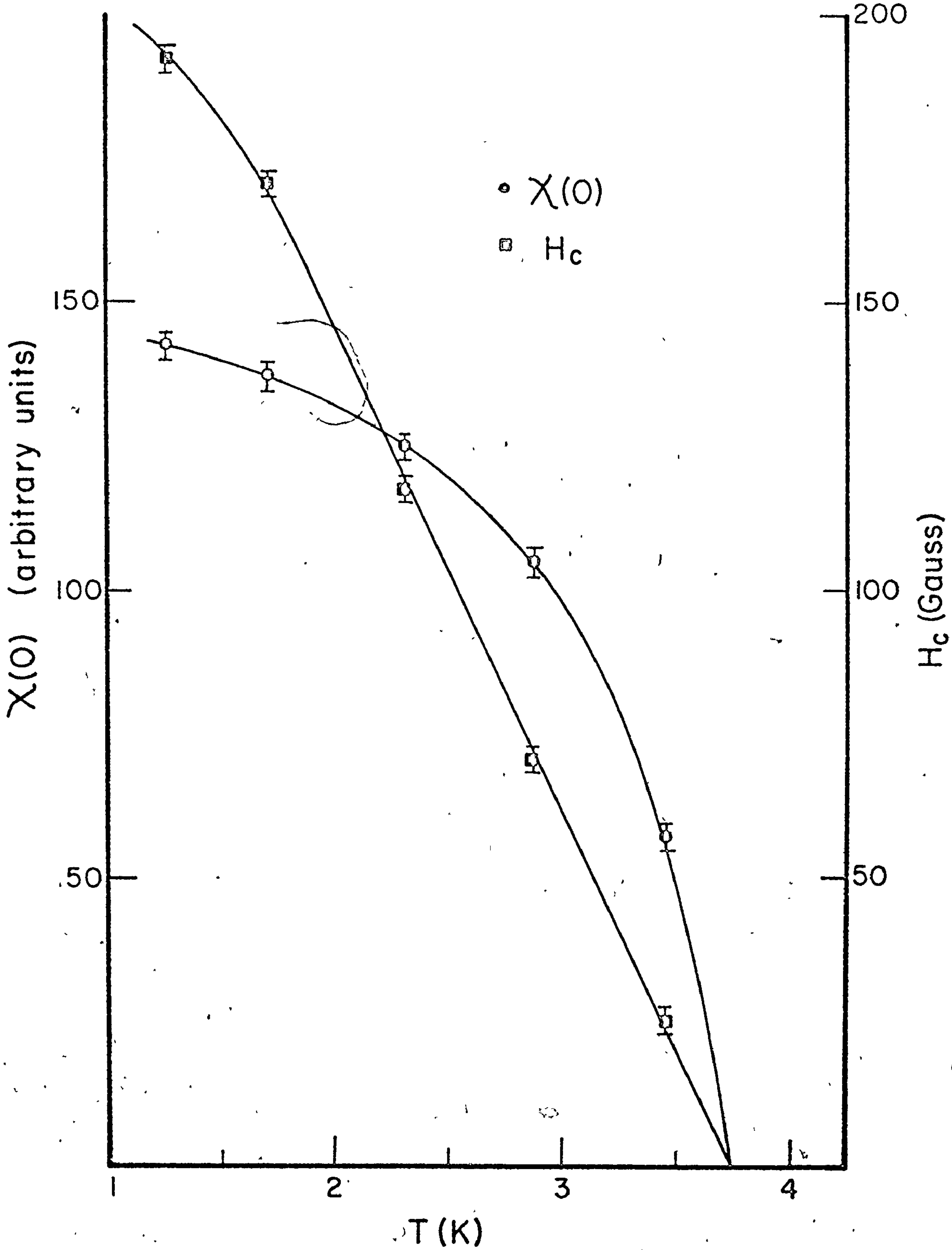

χ(0)
Hc
χ(0) (arbitrary units)
Hc (Gauss)
150
100
.50
200
150
100
50
1
2
3
4
T (K)

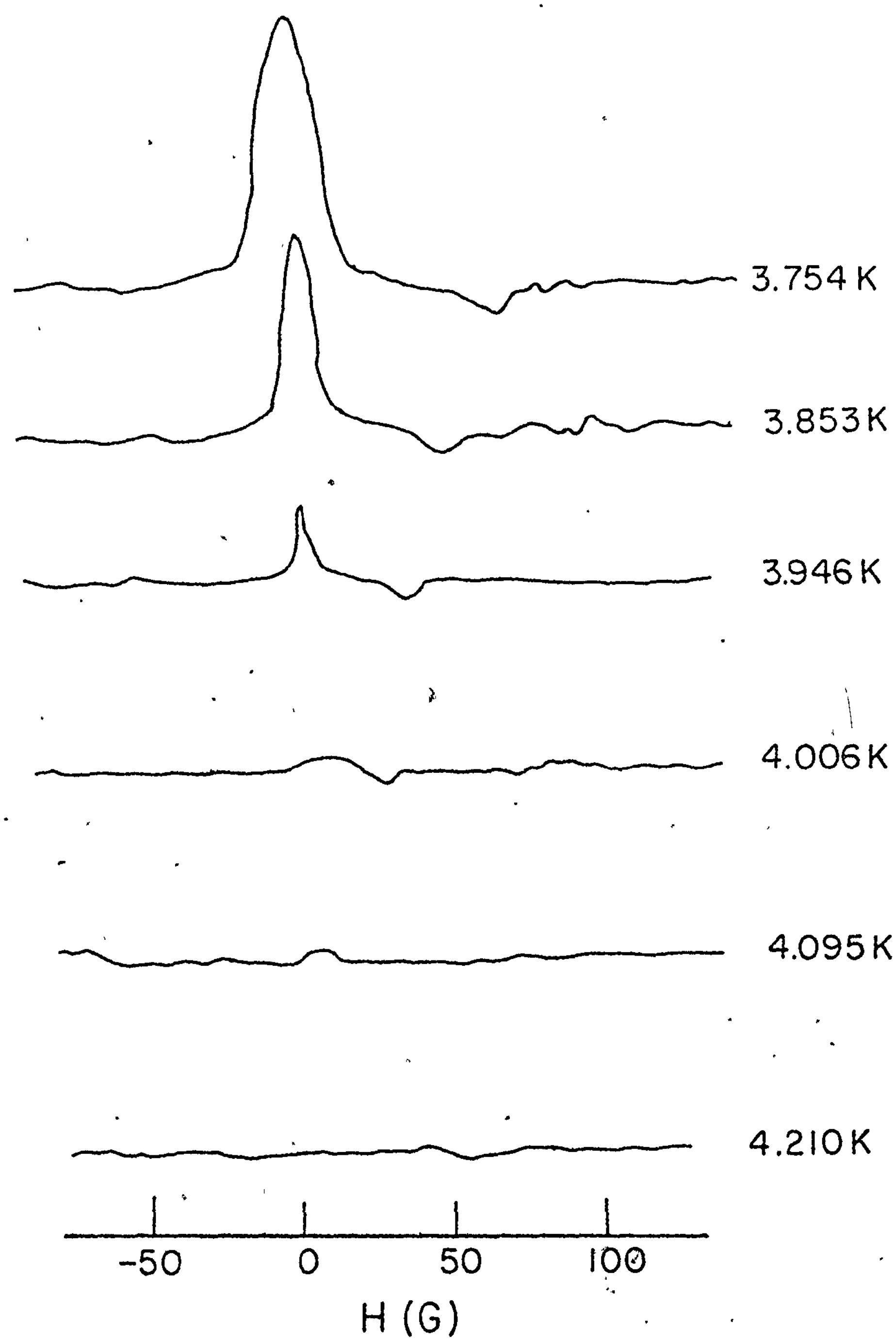

Figure V.7

Chart-recorder traces of pick-up voltage as a function of field at six temperatures for a single crystal of $Hg_{3-\delta}AsF_6$.

Also the resistance of single crystals of $Hg_{3-\delta}AsF_6$ between 1.25 and 4.2 K was measured. It was shown in section IV.c, that the resistance measured by applying a current on an ab face of a sample and measuring the voltage across two point contacts directly opposite on the other ab face of this sample will increase by more than 1600 if the resistivity along the c axis goes down by three orders of magnitude while the resistivity in the ab face remains constant as was reported by Chiang et al (1977). Any such increase in this resistance was not observed for the two samples we investigated down to 1.25 K.

The resistivity of other samples has been measured with other arrangements of the current and voltage probes and a drop in the resistivity at 4.1 K has never been observed.

d) Discussion

The results obtained with the powder samples show that there are two independent processes that will cause the magnetization to change. The high field transition, which was not reported in magnetization experiments by previous workers, is due to elemental mercury being present. This is shown by the value of the critical temperature and the variation of the critical field with temperature for this transition. This mercury is either extruded from the sample during the cool down from room-temperature because of the differential contraction of the mercury chains and the anions or is a result of decomposition by reducing agents in the atmosphere surrounding the sample. Visual observation of the sample after the experiments had been completed confirmed the presence of some mercury on the surface of the sample.

Since the critical temperature and magnetic field observed in the resistivity by Chiang et al (1977) are also close to the corresponding values for mercury, we attribute the transitions that they observed to the superconducting transition of mercury. This transition is different from that observed at lower fields in the magnetization and ac susceptibility. Thus, it is not correct to associate the properties observed in resistivity and magnetization as was done by Spal et al (1979).

The low field transition has been identified previously as the onset of superconductivity in this compound. The plots of the zero field susceptibility against temperature for our samples are in qualitative agreement with the data of Spal et al. $\chi(0)$ increases monotonically with lowering temperature below the critical temperature, T_c. In a bulk superconductor, the zero field susceptibility would be constant and equal to $1/4\pi$ below T_c. The critical temperatures observed range from 3.2 to 3.6 K on the first cool down of the sample while Spal et al reported a T_c of 4.1 K. Also, the critical temperatures increase with each thermal cycling of the powders.

The results of our experiments with a single crystal confirm that the critical temperature of the low field transition increases with thermal cycling. Also, the critical field for this transition is five times smaller for $\vec{H}$ perpendicular to $\vec{c}$ than for $\vec{H}$ parallel to $\vec{c}$ at 3.85 K. Below this temperature, the anisotropy decreases and at the lowest temperature, 1.25 K, the critical field is 350 G when the field is parallel to $\vec{c}$ and 200 G when the field is perpendicular to $\vec{c}$.

Fig. V.8 shows a trace of the ac susceptibility as a function of fields for $Hg_{3-\delta}AsF_6$ at 1.25 K with the field perpendicular to $\vec{c}$ together with similar graphs for spheres of Sn at 3.17 K (type I superconductor) and Ta at 2.93 K (type II) taken from Hein and Falge (1961). Up to half of the critical field the ac susceptibility of the Sn and Ta samples is independent of field while it decreases by 20% for the mercury compound. At 2/3 H_c, the ac susceptibility of the Sn sample decreases rapidly and eventually changes sign while the susceptibility of the Ta sample begins to decrease and that of the mercury compound continues to decrease. A change of sign of the susceptibility at high fields was observed when elemental mercury was present with our compound. These changes occur in the Sn and Ta samples at 2/3 H_c because the demagnetization factor of a sphere is 1/3 and the internal field has exceeded the critical field at certain points on the sphere. When this happens, the total magnetization in both spheres begins to decrease. The ac susceptibility of the Ta sphere does not change sign because

Figure V.8

ac susceptibility as a function of field in single crystals of $Hg_{3-\delta}AsF_6$ at 1.25 K, Sn at 3.17 K and Ta at 2.93 K. Traces obtained when the field is increased and decreased are designated by arrows.

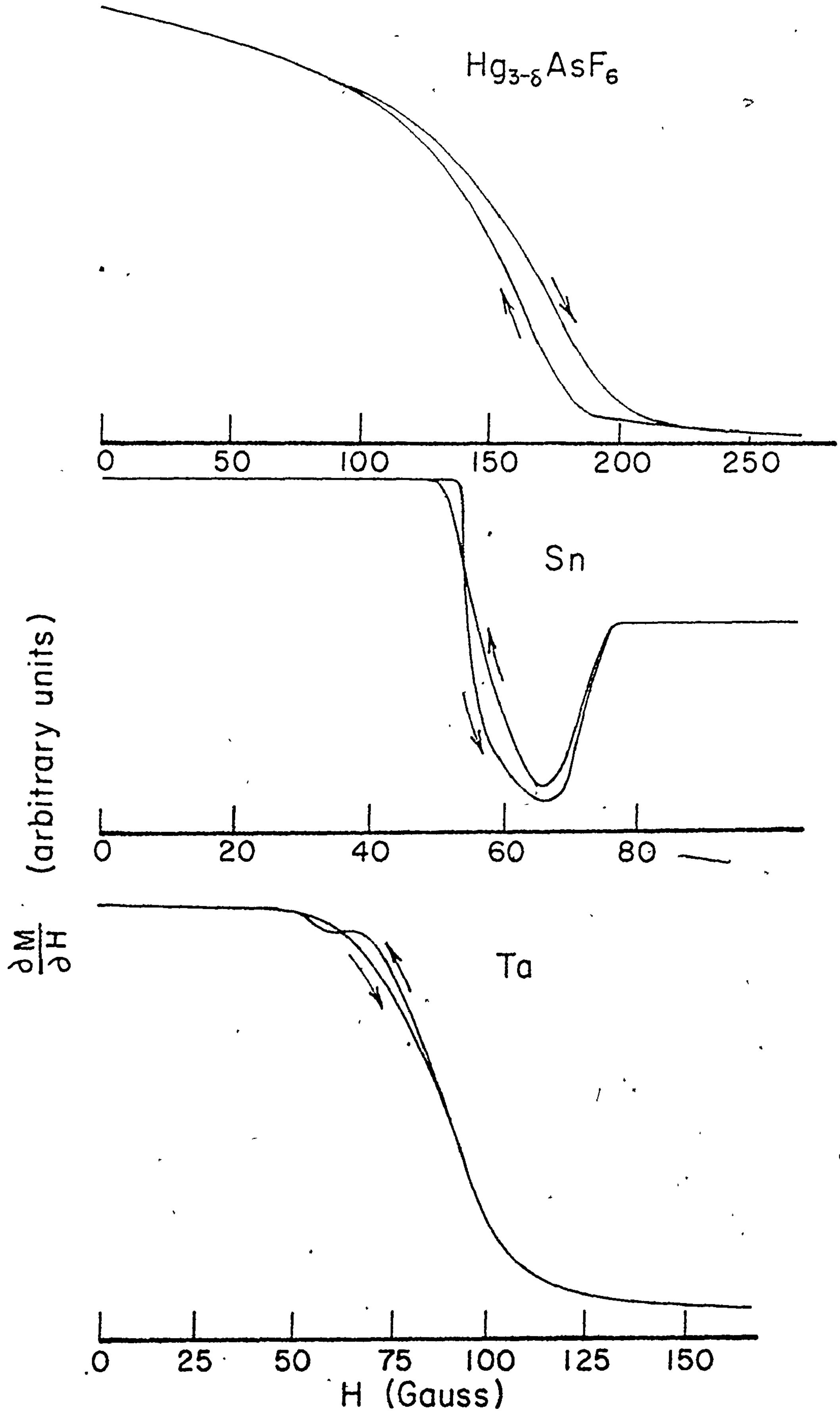

$Hg_{3-\delta}AsF_6$
0
50
100
150
200
250
Sn
0
20
40
60
80
Ta
0
25
50
75
100
125
150
$\frac{\partial M}{\partial H}$ (arbitrary units)
H (Gauss)

at fields exceeding 2/3 H_c, the magnetization does not remain on the magnetization curve. When the field is modulated, the magnetization follows a loop with an average slope that is not very different from the magnetization slope when the whole sample was superconducting. Therefore, the ac susceptibility of the Ta sample does not become negative but decreases steadily, reaching zero at the critical field as a result of this property of the intermediate state in type II superconductors.

Because $Hg_{3-\delta}AsF_6$ starts to show the same type of behaviour at lower fields, it suggests that the mercury compound enters the intermediate state at a very low value of magnetic field .

Two explanations are suggested for the observed anomalies in the superconducting behaviour of the linear mercury chain compound. $Hg_{3-\delta}AsF_6$ could be an anisotropic type II superconductor similar to the transition metal dichalcogenides (Morris et al, 1972) and the graphite intercalates (Hannay et al, 1965). In these two types of compounds having layered structures, the critical field for superconductivity is larger when the field is aligned with the layers than when it is perpendicular to the layers. For $Hg_{3-\delta}AsF_6$, the critical field is larger when the field is perpendicular to the plane of the chains. H_{c_1}, the field at which a type II superconductor enters the intermediate state, would then be smaller than 0.015 G in this compound according to the magnetization measurements of Spal et al. This would explain why our ac susceptibility is not constant for fields smaller than 10 G. The critical field measured in this experiment would be H_{c_2} the field at which no parts of the sample are in the superconducting state.

The other suggestion is that regions of elemental mercury on the surface and in the interior of the sample become superconducting at a temperature close to the transition temperature of mercury. Superconducting pairs in these regions are leaking to the normal metallic regions making a larger volume participate in the Meissner effect. If these regions are thin planes of mercury atoms containing the c-axis, the magnetic field dependence that has been observed can be understood qualitatively because of the much larger demagnetization factor when the field is perpendicular to a plane than when it is parallel. The amount of mercury in these regions would depend on the number and type of defects in our crystals which would explain why we do see this effect in only one of seven samples and why thermal cycling causes T_c to change. However, this hypothesis is not completely satisfactory because it was not possible to force a sample to exhibit a superconducting transition by thermally cycling it if it did not show any transition initially.

A summary of what is known about the superconducting properties of the mercury linear chain compound, $Hg_{3-\delta}$, is presented below.

First, there is a superconducting transition caused by some metallic mercury. This transition is observed in our measurements of the ac susceptibility in all powders studied and in all the crystals after a certain number of temperature cyclings. Also, we believe that Chiang <u>et al</u> recorded this transition in their measurements of resistivity.

Also, there is another transition in the magnetization of these compounds. The critical temperatures for this transition range from 3.2 to 4.1 K and increase with temperature cycling of the samples. Also, the critical field for this transition is larger when the magnetic field is along the c axis than when the field is perpendicular to the c axis. The magnetization in that state is larger when the field is perpendicular to $\vec{c}$ than when the field is parallel to $\vec{c}$. Along both directions, the zero field susceptibility increases when the temperature is lowered below T_c down to the lowest temperature attainable.

By dividing all the observed phenomena in this way, we see that the superconducting behaviour of $Hg_{3-\delta}AsF_6$ is not as anomalous as previous workers had noted and could possibly be explained as being a type II superconductor or a normal conductor with regions of mercury embedded in it.

CHAPTER VI

CONCLUSIONS

A model of the Fermi surface of the mercury chain compounds was constructed using one-dimensional electron dispersion relation for the valence electron remaining on the chains and taking account of the incommensurability of these chains with respect to the anion lattice. This Fermi surface model consists of square based cylinders aligned with the c axis. Formulas for the possible orbits on this Fermi surface in terms of the lattice parameter, a, and the incommensurability parameter, δ, and for the cyclotron masses corresponding to these orbits were obtained.

The fundamental dHvA frequencies in $Hg_{3-\delta}SbF_6$ were measured on a polycrystalline sample. These measurements indicated that the Fermi surface of $Hg_{3-\delta}SbF_6$ consists of cylinders aligned with the c axis. The minimum cross-sections of these cylinders were accurately fitted using the Fermi surface model.

The cyclotron masses corresponding to fundamental frequencies in $Hg_{3-\delta}AsF_6$ and $Hg_{3-\delta}SbF_6$ were also observed from the dHvA effect measurements and were compared to the predictions of the Fermi surface model.

The dHvA frequencies in $Hg_{3-\delta}AsF_6$ were measured under hydrostatic pressures between 0 and 5 kbar. The rates of change of the fundamental frequencies with pressure were explained assuming a contraction of the hexafluoride anion lattice while the mercury-mercury distance remained constant. The lack of change in frequency with pressure during one day was attributed to a slow return to the chains of the mercury atoms that were extruded when pressure was applied.

These Fermi surface measurements show that the Fermi surface model is valid for values of the incommensurability parameter of 0.135 in $Hg_{3-\delta}SbF_6$ and 0.210 in $Hg_{3-\delta}AsF_6$, a difference of 35%. This model also applies to incommensurability parameters ranging from 0.21 to 0.23 in $Hg_{3-\delta}AsF_6$ under pressure.

The cylindrical Fermi surface and scattering of electrons by one-dimensional and three-dimensional phonons were used to construct a model of the temperature dependence of the resistivity. This model agreed with measurements of the resistivity in the ab plane between 4.2 and 90 K, and with measurements of the ratio of the resistivity along the c axis to the resistivity in the ab plane between 4.2 and 250 K in $Hg_{3-\delta}AsF_6$. Therefore, electron-phonon scattering can account for the temperature dependent part of the resistivity in this anisotropic conductor as it does in most isotropic metals.

Between 90 and 300 K, the experimental resistivity was different on warming and cooling curves indicating that an unusual transition occurs at 217 K upon cooling. This transition was related to the differential thermal analysis results of Datars et al (1979) indicating that it is coincident with mercury extrusion from the sample. It is suggested that macroscopic defects in the sample are created when this mercury extrusion takes place causing the changes in resistivity.

The ac susceptibility of powders and crystals of $Hg_{3-\delta}AsF_6$ was measured between 1.2 and 4.2 K in fields ranging from 0 to 400 G. The superconducting transition of metallic mercury was observed indicating that some elemental mercury was present with the sample. The zero-field susceptibility and the critical field associated with a transition in the mercury chain compound were also measured. This distinction between the two sources of magnetization changes suggests that the resistivity drop along the c axis observed by Chiang et al (1977) at 4.1 K is due to elemental mercury. The Meissner effect measurements of Spal et al (1977) and the measurements presented in this work can then be explained if $Hg_{3-\delta}AsF_6$ is a type II superconductor or if it contains regions of elemental mercury trapped in the sample.

In summary, two factors dominate the electronic properties of the mercury linear chain compounds: the localization of the conduction electrons on the mercury chains and the incommensurability of the mercury and anion lattices. It is this unique combination of these factors which leads to the interesting behaviour of the compounds described in this thesis.

BIBLIOGRAPHY

Berlinsky, A.J. 1978. Private communication.

Bridgman, P.W. 1931. The Physics of High Pressure, G. Bell and Sons Ltd., 149-188.

Brown, I.D., Cutforth, B.D., Davies, C.G., Gillespie, R.J., Ireland, P.R. and Vekris, J.E. 1974. Canadian J. Chem. 52, 791.

Chakraborty, D.P., Spal, R., Chiang, C.K., Denenstein, A.M., Heeger, A.J. and MacDiarmid, A.G. 1978. Solid State Commun. 27, 849.

Chakraborty, D.P., Spal, R., Denenstein, A.M., Lee, K.B., Heeger, A.J. and Azbel, M. Ya. 1979. Phys. Rev. Lett. 43, 1832.

Chiang, C.K., Spal, R., Denenstein, A.M., Heeger, A.J., Miro, N.D. and MacDiarmid, A.G. 1977. Solid State Commun. 22, 293.

Cutforth, B.D. 1975. Ph.D. Thesis, McMaster University.

Cutforth, B.D., Datars, W.R., van Schyndel, A. and Gillespie, R.J. 1977. Solid State Commun. 21, 377.

Datars, W.R., van Schyndel, A., Lass, J.S., Chartier, D. and Gillespie, R.J. 1978. Phys. Rev. Lett. 40, 1184.

Dinser, R.J., Datars, W.R., Chartier, D. and Gillespie, R.J. 1979. Solid State Commun. 32, 1041.

Ehrenfreund, E., Newman, P.R., Heeger, A.J., Miro, N.D. and MacDiarmid, A.G. 1977. Phys. Rev. B16, 1791.

Gillespie, R.J. and Ummat, P.K. 1971. J. Chem. Soc. Chem. Commun., 1168.

Gold, A.V., 1968. Solid State Physics, the Simon Fraser Univ. Lectures, Vol. 1, Electrons in Metals, ed.: Cochran, J.F.

and Haering, R.R.: Gordon and Breach, 39-126.

Hein, R.A. and Falge, R.L. 1961. Phys. Rev. 123, 407.

Hannay, N.B., Geballe, T.H., Matthias, B.T., Andres, K., Schmidt, P. and MacNair, D. 1965. Phys. Rev. Lett. 14, 225.

Heilmann, I.U., Axe, J.D., Hastings, J.M., Shirane, G., Heeger, A.J. and MacDiarmid, A.G. 1979. Phys. Rev. B20, 751.

Jumper, W.D. and Lawrence, W.E. 1977, Phys. Rev. B16, 3314.

Kaveh, M. and Ehrenfreund, E. 1979. Solid State Commun. 31, 709.

Koteles, E.S., Datars, W.R., Cutforth, B.D. and Gillespie, R.J. 1976. Solid State Commun. 20, 1129.

Little, W.A. 1964. Phys. Rev. 134, A1416.

Logan, B.F., Rice, S.O. and Wick, R.F. 1971. J. Appl. Phys. 42, 2975.

Lomer, W.M. 1964, in Proc. Int. Conf. Magnetism, Nottingham, The Institute of Physics and the Physical Society, 127.

Montgomery, H.C. 1971. J. Appl. Phys. 42, 2971.

Morris, R.C., Coleman, R.V. and Bhandari, R. 1972. Phys. Rev. B5, 895.

Peebles, D.L., Chiang, C.K., Cohen, M.J., Heeger, A.J., Miro, N.D and MacDiarmid, A.G. 1977. Phys. Rev. B15, 4607.

Pouget, J.P., Shirane, G., Hastings, J.M., Heeger, A.J., Miro, N.D. and MacDiarmid, A.G. 1978. Phys. Rev. B18, 3645.

Poulsen, R.G., Moss, J.S. and Datars, W.R. 1971. Phys. Rev. B3, 3107.

Razavi, F.S., Datars, W.R., Chartier, D. and Gillespie, R.J. 1979. Phys. Rev. Lett. 42, 1182.

Schafer, D.E., Wudl, F., Thomas, G.A., Ferraris, J.P. and Cowan, D.O. 1974. Solid State Commun. 14, 347.

Scholz, G.A., Datars, W.R., Chartier, D. and Gillespie, R.J. 1977. Phys. Rev. B16, 4209.

Slavin, A.J. and Datars, W.R. 1974. Can. J. Phys. 62, 1622.

Spal, R., Chiang, C.K., Denenstein, A., Heeger, A.J., Miro, N.D. and MacDiarmid, A.G. 1977. Phys. Rev. Lett. 39, 650.

Spal, R., Chen, C.-E., Denenstein, A., McGhie, A.R., Heeger, A.J. and MacDiarmid, A.G. 1979. Solid State Commun. 32, 641.

Stark, R.W. and Friedberg, C.B. 1971. Phys. Rev. Lett. 26, 556.

van Schyndel, A. 1976. Private communication.

Wasscher, J.D. 1961. Phillips Res. Repts. 16, 301.

Wei, T., Garito, A.F., Chiang, C.K. and Miro, N.D. 1977. Phys. Rev. B16, 3373.

Ziman, J.M. 1960. Electrons and Phonons, Oxford University Press, 357-367.